ABSTRACT

Title of dissertation: STEPS ON VICINAL SURFACES:
DENSITY-FUNCTIONAL THEORY CALCULATIONS
AND TRANSCENDING MINIMAL
STATISTICAL-MECHANICAL MODELS

Rajesh Sathiyanarayanan
Doctor of Philosophy, 2009

Dissertation directed by: Professor Theodore L. Einstein
Department of Physics

Using both density-functional theory calculations and Monte Carlo simulations, we compute various key parameters that are used to model steps on vicinal surfaces.

In the first part, we discuss the importance of multi-site interactions (trios and quartos) in the lattice-gas characterization of adatom interactions. Using density-functional theory calculations, we show that multi-site interactions with substantial contributions from direct interactions are sensitive to adatom relaxations. Such sensitivity to adatom relaxations complicates the lattice-gas approach to modeling overlayer systems. Our results show that a careful consideration of relaxation effects is required to make connections with experiments.

In the second part, we use both density-functional theory calculations and kinetic Monte Carlo simulations to identify the impurity atom responsible for growth instabilities on Cu vicinals. In addition to that, we also show that a small quantity

of codeposited impurities significantly alters the growth behavior. Our results indicate that growth morphologies could be controlled through the codeposition of an appropriate impurity. Hence, impurities could play a crucial role in nanostructuring of surfaces.

Step configurations have fruitfully been related to the worldlines of spinless fermions in one dimension. However, in addition to the realistic no-crossing condition, the fermion picture imposes a more restrictive non-touching condition. in the third part of this thesis, we use Metropolis Monte Carlo method to study the effects of loosening this non-touching condition on the resulting TWDs. Our results show that allowing step touching leads to an effective attraction in the step-step interaction strength measurements. We show that this effective attraction can be incorporated into the fermion picture as a finite-size effect.

STEPS ON VICINAL SURFACES: DENSITY-FUNCTIONAL THEORY CALCULATIONS AND TRANSCENDING MINIMAL STATISTICAL-MECHANICAL MODELS

by

Rajesh Sathiyanarayanan

Dissertation submitted to the Faculty of the Graduate School of the
University of Maryland, College Park in partial fulfillment
of the requirements for the degree of
Doctor of Philosophy
2009

Advisory Committee:
Professor Theodore L. Einstein, Chair/Advisor
Professor Ellen D. Williams
Professor John D. Weeks
Professor Janice E. Reutt-Robey
Professor Victor M. Yakovenko

This thesis is dedicated to my family.

Acknowledgments

First and foremost, I would like to thank my family and friends for their invaluable help and support during the entire course of this work.

My deepest gratitude to my advisor, Professor Theodore Einstein, for providing valuable guidance and for giving me an opportunity to work on challenging and extremely interesting problems in surface science. I would also like to thank Professor Ellen Williams for her help and support throughout this work.

I would like to thank Dr. Alberto Pimpinelli and Dr. Ajmi Hamouda for their help in the later parts of this thesis. Working with them has been a wonderful educational experience for me. Through several fruitful discussions, they have helped me learn about various surface phenomena and random matrix ideas.

Thanks are due to Professor Ellen Williams, Professor John Weeks, Professor Janice Reutt-Robey and Professor Victor Yakovenko for agreeing to serve on my thesis committee and for sparing their invaluable time reviewing the manuscript.

It was truly a wonderful experience working with all the members of the surface science group. Special thanks to Timothy Stasevich and Hailu Gebremariam for their patience and support during the initial stages of this work.

I would like to thank MRSEC for the financial support and the National Center for Supercomputing Applications, University of Illinois at Urbana-Champaign for providing the required computational resources to carry out my calculations.

Sincere thanks and apologies to people whom I have failed to mention here.

Table of Contents

List of Tables

List of Figures

Chapter 1

Introduction

There has been a continuous and consistent trend in the miniaturization of devices in the recent decades. One of the fields in which this trend is clearly evident is the microelectronics industry, as exemplified by the sustained realization of Moore's law for more than forty years. Keeping pace with this rate of miniaturization depends on the development of technological capability to fabricate devices and components at nanometer length scales (0.1-100 nm) in the near future. This has led to and fueled the enormous interest in the field of nanotechnology research. Broadly, there are two approaches for fabrication of devices in the nanometer length scale - the top-down and the bottom-up approaches [1]. In the top-down approach, desired patterns are created on substrates through micropatterning techniques. Alternately, in the bottom-up approach, devices and components are fabricated through growth and subsequent self-assembly of atoms (or molecules) on substrates with well defined physical characteristics. The choice of a good substrate and thorough knowledge about the atomistic mechanisms related to growth are essential for the realization of the bottom-up approach.

Vicinal surfaces [2, 3] are formed when a solid is cleaved along a direction close to a crystalline high-symmetry orientation (cf. Fig. 1.1). Below the roughening temperature of the high-symmetry orientation ($T < T_R$), a vicinal surface has distinct

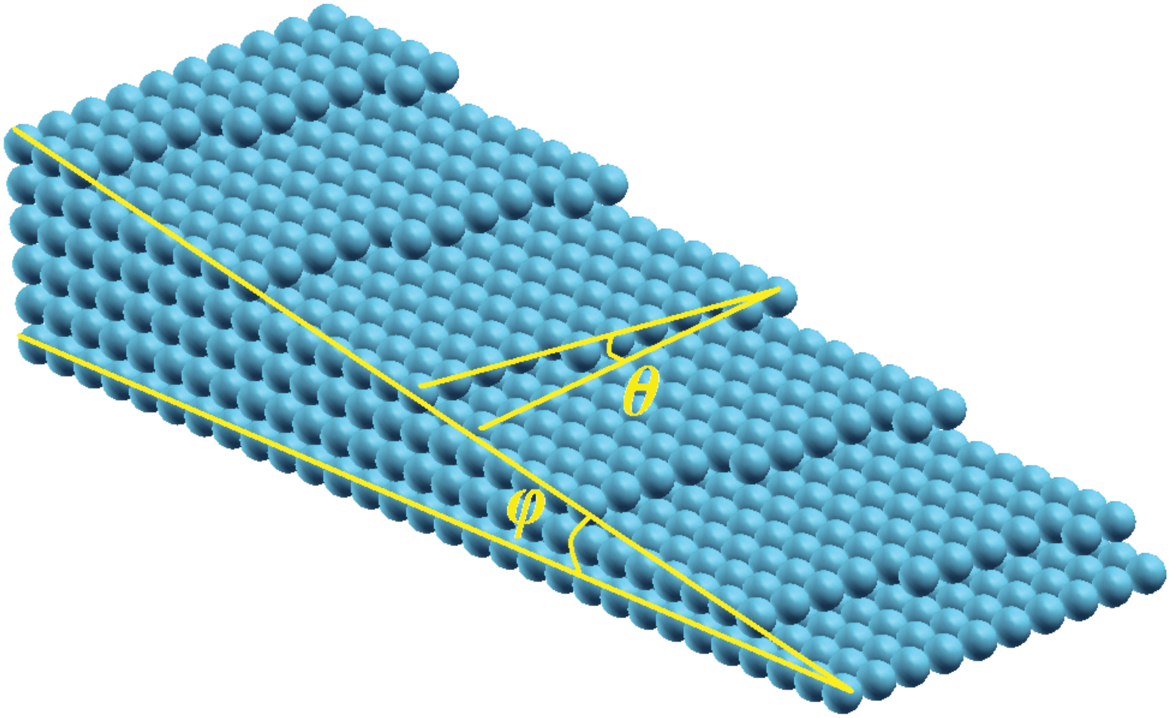

Figure 1.1: A surface vicinal to the high symmetry $\langle 1\ 0\ 0 \rangle$ direction. The surface consists of (1 0 0) terraces separated by close-packed steps that are oriented at an angle $\theta = \tan^{-1}(1/4)$ to the close-packed $\langle 1\ 1\ 0 \rangle$ direction. The polar angle (ϕ) is related to the mean spacing between steps ($\langle \ell \rangle$) through: $\langle \ell \rangle = 1/\tan(\phi)$. The tangent of the azimuthal angle (θ) gives the linear density of kinks (1/4 in this case).

physical features - high-symmetry terraces separated by steps and depending on the miscut direction, these steps could contain kinks (geometric kinks). Due to controlled number of defects, vicinal surfaces serve as ideal substrates for growth and self-assembly processes in the bottom-up approach. In addition to acting as templates for growth of microstructures, such as quantum dots and nanowires, vicinal surfaces are also widely used in the catalysis of chemical and biological reactions. At $T = 0$K, the orientation of the steps and the density of kinks remain fixed. However at the operating temperature of these devices (close to room temperature), thermal

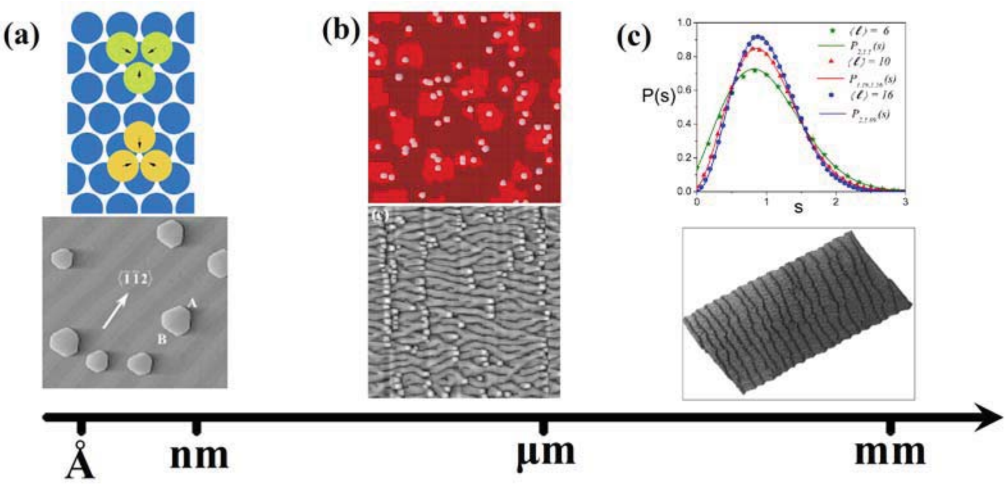

Figure 1.2: Multi-scale modeling of steps: the top panels show the analytic method appropriate at that particular length scale and the bottom panels show the respective experimental observations. (a)top: calculation of *A*- and *B*-step formation energies using orientation-dependent trios on fcc (1 1 1) surfaces [4, 5], bottom: Pt islands with a ratio of 1.16 between *A*- and *B*-step formation energies [6], (b)top: kinetic Monte Carlo simulations of early stages of growth when 2% of W atoms are codeposited with Cu atoms on Cu(1 0 0) (cf. Chapter 3), bottom: formation of tall pyramids at higher coverages for the same system [7], (c)top: generalized Wigner fits [8, 9] to the terrace width distributions of steps, bottom: 2800 × 2800 Å^2 STM image of Al/Si(1 1 1) [10]. The step-step interaction strength for this system was estimated using the generalized Wigner formalism.

motion of atoms causes step fluctuations[1] and the formation of adatom and vacancy islands on terraces. As a result, thermal motion of atoms play a crucial role in altering morphologies of vicinal surfaces. Hence, a thorough understanding of various atomistic processes and step fluctuations is required to fabricate devices that remain stable at room temperatures.

An accurate analytic treatment of morphological evolution of vicinal surfaces should provide a description that is valid at vastly different length scales. It should take into account atomic scale (sub-nanometer) properties while characterizing step

---

[1] The attachment and detachment of atoms at step edges creates additional kinks, known as thermal kinks.

fluctuations and surface morphologies at much larger length scales (few micrometers). Since the analytic description is required to span length scales that are separated by several orders of magnitude, multi-scale models are normally used for characterizing evolution of surface morphologies (cf. Fig. 1.2). A purely continuum approach towards constructing such a multi-scale model, despite being computationally economical, is inadequate to capture the effects of atomistic processes. On the other hand, a more accurate approach that accounts for the behavior of every individual atom in the system is unsuitable for systems with more than a few hundred atoms due to the very high computational cost associated with it. An extremely successful approach that incorporates atomic scale properties with the computational ease of a continuum approach is the continuum step model [2]. In the continuum step model, steps are considered continuous along the step-edge direction and discrete in the direction perpendicular to the step-edge; the evolution of the surface is then described in terms of motion of steps. In general, the mean direction of step edges is labeled $\hat{y}$ and the perpendicular direction is labeled $\hat{x}$; this notation has become known as "Maryland notation". The position of the i-th step edge, $x_i(y)$, varies continuously with y.

In the continuum step model, the length scales are bridged in the following way - the behavior of individual atoms is linked to a few key, experimentally measurable parameters through statistical mechanics and these parameters are then used to predict and understand the evolution of steps and surface morphologies under various conditions. Hence, minimal statistical-mechanical models lie at the core of the continuum step model. At the nanometer length scale, the main energy parameters in this model are adatom interactions and barriers for the diffusion of single (or at most a few) adatoms. Traditionally, many theoretical methods, such as tight-binding [11, 12], embedded atom method [13, 14], etc. have been employed to compute these energy parameters. With recent advances in computational power, these energy parameters can now be computed with reliable accuracy using more sophisticated computational packages based on the density-functional theory (DFT) [15, 16]. The computed energy parameters are then linked to macroscopic parameters like step formation energy, step stiffness ($\tilde{\beta}$), etc., using ideas from statistical mechanics. These macroscopic parameters are then used to simulate fluctuations of steps (up to several thousand atoms) using Monte Carlo methods. The choice of surface representation and the computational method depends on the physical property under study. For instance, kinetic Monte Carlo (KMC) simulations on a solid-on-solid (SOS) lattice are suited for studying growth and other non-equilibrium phenomena and the Metropolis Monte Carlo method with the terrace-step-kink (TSK) model is suited for studying equilibrium properties. Conversely, both microscopic and macroscopic parameters can be measured through experimental or simulation studies of step fluctuations. Hence, the continuum step model plays an important role in studying morphologies of vicinal surfaces.

In short, analytic modeling of steps on vicinal surfaces routinely makes use of minimal statistical-mechanical models to understand and predict morphological evolution of surfaces. The success of this approach relies on the identification and accurate computation of the model parameters. However, minimal statistical-mechanical models fall short of providing a complete description of morphological evolution of vicinal surfaces in certain situations. This thesis discusses a few of these cases and also provides the necessary modifications to the minimal model required to make connection with experimental observations in each of these cases. Chapter 2 emphasizes the importance of non-pairwise multi-site interactions in the lattice-gas picture. Through extensive calculations using DFT-based Vienna Ab initio Simulation Package (VASP) [17, 18, 19, 20] calculations on different high symmetry surfaces, we show that adatom relaxations play a crucial role in the computations of multi-site interaction strengths. In Chapter 3, we investigate the effect of codeposited impurities on the resultant surface morphologies; we focus on Cu vicinals. Experiments performed by Ernst and co-workers showed that Cu vicinals undergo meandering and mounding instabilities during growth. Even though various instability mechanisms have been proposed to account for the observed instabilities, none of them could explain all experimental observations. Recently, it was shown that codeposition of small percentage of impurities with Cu atoms during growth could reproduce the experimental results. To identify the impurity atom responsible for the observed instabilities, we computed the binding energies and diffusion barriers for various candidate impurity atoms. Using the energies for the candidate impurity atoms from DFT calculations in KMC simulations, we then study the effect of impurity codeposition on the resulting surface morphologies. Our results presented in Chapter 3 show that by codepositing a specific impurity atom during growth, we can control the resultant surface morphologies. The terrace-width distribution (TWD) is a useful quantity to parameterize both non-equilibrium and equilibrium step fluctuations on vicinal surfaces. In addition to that, certain important parameters used for modeling steps can be extracted from TWD measurements. The fermion picture, as exploited by Calogero and Sutherland [21], facilitates the theoretical treatment of TWDs and provides a straightforward way to measure the step-step interaction strength parameter ($\tilde{A}$). However, the fermion picture depends on the assumption that step edges do not touch each other during fluctuations. We study the effects of loosening this non-touching condition on the TWDs of vicinal surfaces, and hence $\tilde{A}$ measurements. Our results are presented in Chapter 4. A summary of our results and open questions are presented in Chapter 5.

Chapter 2

Role of multi-site interactions in the lattice-gas modeling of steps: Adatom relaxations[1]

2.1 Lattice-gas model and multi-site interactions

A thorough understanding and characterization of surface energetics is important for fabricating nanostructures with desired morphological features. To this end, lattice-gas models have been very successful in catergorizing structural properties, energetics and evolution of adatoms and steps on surfaces, as discussed in a variety of reviews [24, 25, 26, 27]. The general idea being that a set of interactions is sufficient to understand both equilibrium and dynamic surface processes. The supercell approach [28, 29] implemented in DFT-based [15, 16] computational packages, such as VASP [17, 18, 19, 20], provides a direct way to compute these interactions with reliable accuracy. Ref. [29] serves as an excellent guidebook for using DFT-based software packages, especially VASP, to compute adatom interactions on vicinal surfaces. The lattice-gas interactions are then used in Monte Carlo simulations to test whether they account adequately for experimentally observed properties such as phase diagrams, equilibrium island shapes, or step fluctuations.

The basic assumptions that underlie lattice-gas models are: (i) all atoms sit at high-symmetry positions and local relaxations produce the final structure, (ii) a

---

[1] Adapted from Refs. [22] and [23].

finite set of effective interactions is sufficient to understand all the surface processes and (iii) interactions are not sensitive to local positions of the adatoms. In the simplest scenario, only pair interactions between nearest neighbors are considered. However, in certain cases, like the orientation dependence of step stiffness and the equilibrium shape of islands, long-range pair interactions and multi-site interactions are required for a complete description [5, 22, 23, 30, 31, 32, 33, 34, 35, 36]. The substrates in these studies are typically mid or late transition or noble metals, where the electronic indirect interaction leads to rich behavior [26].

In the lattice-gas model, the Hamiltonian of adatoms on a surface is written as:

$$H = E_1 \sum_{\langle i,j \rangle_1} n_i n_j + E_2 \sum_{\langle i,j \rangle_2} n_i n_j + ... + \sum_T E_T \sum_{\langle i,j,k \rangle_T} n_i n_j n_k + \sum_Q E_Q \sum_{\langle i,j,k,l \rangle_Q} n_i n_j n_k n_l \tag{2.1}$$

where n_i is the occupancy of the high-symmetry lattice site indexed i; $n_i = 1$ denotes an occupied site and $n_i = 0$ denotes an empty site. Interactions between adatom pairs upto the m^{th}-neighboring pair $(E_1, E_2, ..., E_m)$ are included in the model; accordingly, interactions between adatom pairs that are separated by distances greater than the m^{th}-neighbor distance are expected to be insignificant. E_T stands for three-adatom non-pairwise interactions trio interaction, with the index running over all trimer configurations of significant strength. Similarly, E_Q stands for four-adatom non-pairwise quarto interaction. If necessary, pair interactions with a longer range and/or higher-order multi-site interactions (possibly, five-adatom quintos) are included in the model till adequate convergence between theoretical predictions and experimental observations is obtained. However, the inclusion of a large number of interaction parameters makes the lattice-gas model intractable, thereby severely undermining the efficacy of lattice-gas models in modeling overlayer systems.

In this chapter, we focus only on multi-site interactions in which the participating adatoms are close to each other and hence, share short-range lateral bonds. Such multi-site interactions have significant contributions from direct interactions,[2] especially due to covalent bonding. When the adatom-adatom interactions involve such short-range lateral bonds, it is possible (even likely) that the adatoms can shift non-negligibly from their high-symmetry favored positions. The shifting of adatoms from high-symmetry positions can cause subtle relaxation effects that can complicate the straightforward application of the lattice-gas framework. As we will show in this chapter, such relaxation effects are especially significant for multi-site interactions, where the relaxations are not along the bond directions. Also, multi-site interactions, in general, have a large elastic component; hence, a careful consideration of relaxation effects is essential for accurate computations of their strengths.

In the reminder of this chapter we stress the importance of multi-site interactions in the lattice-gas picture and show that adatom relaxations could complicate the computation of their strengths using three relevant examples. In section 2.2 we discuss the computation of difference in formation energies between the two types of close-packed steps (*A*- and *B*-steps) on fcc (1 1 1) surfaces using a pair of orientation-

---

[2] These are interactions between adatoms that would occur even in the absence of a substrate. The substrate provides only a minor perturbation to these interactions.

dependent trios. Here we consider Pt(1 1 1), where this difference in energy between the two orientations is known to be particularly large [6, 37]. Our VASP calculations indicate that the strengths of the two orientation-dependent trios are very sensitive to adatom relaxations on this surface [22]. Section 2.3 deals with bridging the discrepancy between theoretical calculations and experimental observations of step-stiffness anisotropy on Cu(1 0 0) [22]. Theoretical models actually require multi-site interactions to account for the observed anisotropy in step-stiffness but adatom relaxations severely hamper their evaluation, which worsens the discrepancy between theory and experimental observations. We show that a careful consideration of relaxation effects and the inclusion of a four-adatom quarto interaction resolves the discrepancy between theory and experiments. In section 2.4, we present the results of our VASP calculations of adatom interactions and single atom diffusion barriers of Cu adatoms on Cu(1 1 0) [23]. On this surface, we find many strong multi-site interactions that are comparable in strength to the strongest pair interactions. We also show that these multi-site interactions are very sensitive to adatom relaxations. A summary of our results and remarks about the lattice-gas approach to overlayer systems are given in section 2.5.

2.2 Energy differences of close-packed steps on Pt(1 1 1)

2.2.1 Orientation-dependent trio interactions on fcc (111) surfaces

On fcc (1 1 1) surfaces, close-packed steps can be classified as either *A*-steps [(1 0 0) microfacets] or *B*-steps [(1 1 1) microfacets]. The difference between them

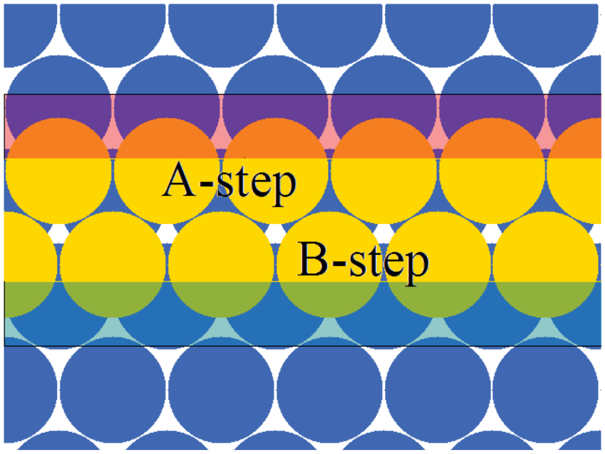

Figure 2.1: Two types of close-packed steps on fcc (1 1 1) surfaces. Throughout this chapter, lighter (yellow/green) circles represent adatoms and darker (blue/orange) circles represent atoms in the substrate layer. The view is from a point directly above ($\hat{z}$) and normal to the surface plane. The translucent strips mark the (1 0 0) microfacets and the (1 1 1) microfacets in the cases of A- and B- steps respectively. For specificity in discussions, the vertical direction in the figure is called $\hat{y}$ and the horizontal direction is $\hat{x}$ throughout this chapter.

lies in their arrangement relative to the substrate atoms. As can be seen in Fig. 2.1, the centers of A-step atoms are aligned with the centers of underlying substrate atoms along the $\hat{x}$ direction forming square (1 0 0) microfacets, whereas centers of B-step atoms are shifted by $a/2\sqrt{2}$ along the $\hat{x}$ direction with respect to the centers of underlying substrate atoms forming triangular (1 1 1) microfacets. Since the difference between A- and B-steps lies in their orientation relative to the substrate atoms, pair interactions, however long-ranged, cannot distinguish between them. To do that, one must introduce other non-pairwise multi-site interactions involving at least three adatoms. Stasevich et al. [4, 5] showed that the minimal multi-site interaction that can distinguish between these two steps is the orientation-dependent trio, an equilateral triangle formed by NN (nearest-neighbor) legs, shown in Fig. 2.2. Atoms on an a-trio share a common substrate atom between them and all of its edges

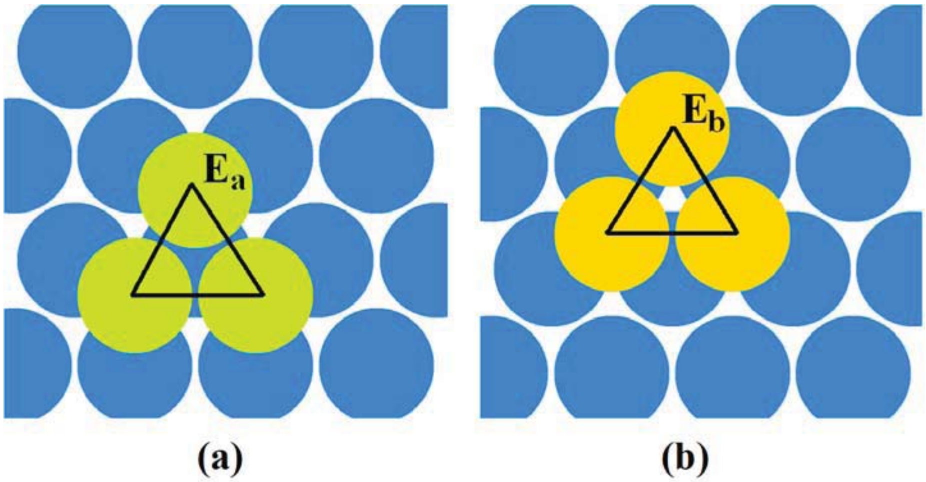

Figure 2.2: Two orientation-dependent trios on a fcc (1 1 1) surface: (a) *a*-trio atoms share a common substrate atom and all edges are *A*-steps, (b) *b*-trio atoms do not share a common substrate atom and all edges are *B*-steps.

are *A*-steps, whereas atoms on a *b*-trio do not share a common substrate atom and all of its edges are *B*-steps. With the inclusion of *a*- and *b*-trios in the lattice-gas pciture, the step formation energies in terms of lattice-gas interactions can be written as [5]

$$E_A = -(E_1 + \frac{1}{3}E_a + \frac{2}{3}E_b + E_c) \tag{2.2a}$$

$$E_B = -(E_1 + \frac{2}{3}E_a + \frac{1}{3}E_b + E_c) \tag{2.2b}$$

where E_1 is the NN interaction[3] and E_c is the three-adatom non-pairwise interaction formed by collinear adatoms along a close-packed direction. Since all other lattice-gas interactions concerning these two steps are the same, the difference in the step formation energies (ΔE_{AB}) are then related to the trios through

---

[3] The nearest-neighbor (NN) and next-nearest-neighbor (NNN) interactions are also denoted by first- and second-neighbor interactions respectively in related literature.

$$\Delta E_{AB} = E_A - E_B = \frac{1}{3}(E_a - E_b). \tag{2.3}$$

Using Eq. (2.3), we can calculate ΔE_{AB} through a straightforward computation of a- and b-trio interaction strengths. Since computing the strength of trios involves the usage of few adatoms (three/six depending on whether adatoms are placed on one/both sides of the slab), it eliminates the need for larger supercells that are typically used in such calculations. This results in a significant reduction in the computational cost normally associated with such step formation energy calculations.[4] In addition to reducing the computational cost, the approach based on orientation-dependent trios also allows us to test one of the fundamental assumptions of the lattice-gas model. The local geometry of atoms, i.e. the number of occupied NN and NNN sites surrounding each adatom, on orientation-dependent trios differ from that of the atoms on long steps. Thus the method of computing ΔE_{AB} directly from the strengths of a- and b-trios is based on the assumption that local geometry of adatoms do not affect lattice-gas interactions. Hence the success of this method is intrinsically tied to the validity of assumption (iii) mentioned in the previous section.

Using VASP, Stasevich et al. [5] computed the lattice-gas interactions for Cu adatoms on Cu(1 1 1). Using Eq. (2.2a) and (2.2b), they found $E_A = 277 \pm 23$ meV/atom and $E_B = 267 \pm 23$ meV/atom, which results in the following ratio: $E_A/E_B = 1.04 \pm 0.12$. This ratio is in very good agreement with previous theoretical

---

[4] On Pt, we find that the computation time scales as a power-law with the number of atoms with an exponent between 2 and 3.

calculations [38, 39] and experimental observations [3]. Since the ratio is close to unity, the case of Cu does not provide a convincing test for the success of the simple trio-based method. To put this method to a sterner test, we studied the case of orientation-dependent trios on Pt(1 1 1). From the ratio of lengths of adjacent close-packed step edges of adatom islands, Michely and Comsa [6] determined the ratio of the step formation energies at 625 K (finite-temperature generalization of E_A/E_B) to be 1.15 ± 0.03, which translates to $\Delta E_{AB} \approx 50$ mev/atom. Due to a large value of ΔE_{AB}, Pt(1 1 1) becomes an apt surface for testing the applicability of our simple trio-based model.

2.2.2 Step formation energies on Pt(1 1 1)

To compute the difference in step formation energies (ΔE_{AB}), we used VASP with its ultrasoft pseudopotentials for Pt and the Ceperley-Alder local density approximation (LDA) [40]. We used LDA because Boisvert et al. [41] showed that LDA produces a better estimate of the Pt surface energies than the generalized gradient approximation (GGA). We used a cut-off of 14.1 Ryd for the plane-wave basis set. We also used a Methfessel-Paxton [42] width of 0.2 eV to speed up the calculations.[5] The lattice parameter for Pt was determined to be 3.91 Å from a bulk LDA calculation using a $(1 \times 1 \times 1)$ supercell sampled by a $(13 \times 13 \times 13)$ $\mathbf{k}$-point grid. Our straightforward calculation of the trio interaction energies from isolated trimer configurations on Pt(1 1 1) (see Fig. 2.3(a)) used a $(4 \times 4 \times 14)$ supercell sampled by a $(3 \times 3 \times 1)$ $\mathbf{k}$-point grid. Our slab was five atomic layers thick and the rest of

---

[5] This is a recommended setting for calculations involving transition metal surfaces [43].

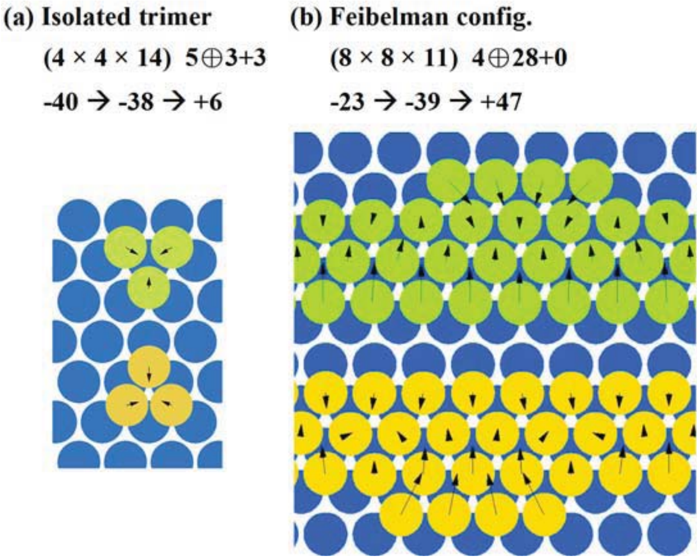

Figure 2.3: Illustration of a basic isolated trimer and the large structure used by Feibelman. Beneath each descriptor is the size of the supercell ($n_x \times n_y \times n_z$) and the layer structure # full atomic layers in the slab ⊕ # adatoms on top of slab + # adatoms on bottom of slab. In the third row are tabulated the ΔE_{AB} values in meV/adatom with no relaxation → the comparable energy when only z-relaxation is allowed → the comparable energy when total relaxation is allowed. In the figure panels the arrows show the magnitude (amplified by a factor of ten for the sake of clarity) and direction of the lateral relaxation. For compactness, each panel combines a pair of configurations onto a single lattice. The upper configuration (green circles) depicts an A-step while the lower configuration (yellow circles) shows a B-step.

the supercell was filled with vacuum. We placed adatoms on both top and bottom of the slab so that any charge-transer effects in computed energies cancel [44]. The adatoms were sited so that they formed either an a-trio (E_a) or a b-trio (E_b). The middle layer was fixed, and atoms in all other layers were allowed to relax in all directions until the net force on the atoms was less than 0.01 eV/Å.

From our calculations, we found $\Delta E_{AB} = +6$ meV/atom consistent with the experimental results of Michely and Comsa [6] that E_B is smaller than E_A. However, the magnitude of ΔE_{AB} is only 1/8 that reported in the DFT calculations of Feibelman [37], who used an $(8 \times 8 \times 4)$ slab with 28 adatoms on one side (cf. Fig. 2.3(b)).

To predict confidently the magnitude of trio interactions, it is important to understand the origin of this large difference between the results of these two calculations. Since the computational parameters used in both calculations are identical, the origin of the difference in ΔE_{AB} values should therefore lie in the relaxation of adatoms. To verify that adatom relaxations are indeed causing the difference, we computed ΔE_{AB} values for both the "isolated trimer" and "Feibelman" configurations in the no-relaxation scheme i.e. atoms are forced into their bulk-continuation positions and relaxations along all directions are suppressed. In the case of no-relaxation, we find, remarkably, that for both the isolated trimer and Feibelman configurations, ΔE_{AB} becomes negative with values -40 and -23 meV/atom respectively (see Fig. 2.3); the B-step formation energy is higher than the A-step formation energy in both configurations, contrary to experimental observations. This shows that adatom relaxations are indeed required to get accurate values of trio interaction strengths. In addition to that, since ΔE_{AB} changes sign between no- and total relaxation, energy lowering due to adatom relaxations is greater at the B-step than at the A-step.

Relaxations of atoms can be purely vertical (normal to the slab, i.e., along $\hat{z}$ direction) or more generally can involve lateral displacements perpendicular to the normal along with vertical relaxations (total relaxation). When atoms are allowed to relax only along the vertical direction (z-relaxation), the obtained ΔE_{AB} values are very close to each other: -38 meV/atom in the isolated trimer configuration and -39 meV/atom in the Feibelman configuration. However, similar to the no-relaxation case, ΔE_{AB} values are negative for both configurations, in contradiction with experimental observations. The ratio of relaxations of A- and B-steps along the $\hat{z}$

direction (i.e. the ratio of change in interlayer separation between adatom and substrate layers) is $\Delta z_B/\Delta z_A = 0.70$ in our isolated trimer configuration and $\Delta z_B/\Delta z_A = 0.68$ in the Feibelman configuration. It should be noted that the ratio of relaxation is less than unity in both cases, i.e., A-step atoms relaxed inward more than B-step atoms. The negative ΔE_{AB} values obtained from both configurations show that vertical relaxations alone cannot guarantee accurate trio interaction strengths. In fact, in the case of the Feibelman configuration, z-relaxation worsened the ΔE_{AB} value by about 50%. As we will show later in this chapter, allowing relaxation only in the vertical direction (z-relaxation) actually exacerbates the problem for most of the adatom configurations.

A crucial difference between our calculations and Feibelman's calculations is the relative amount of lateral relaxations (in-plane displacements from high-symmetry lattice sites) of A- and B-step atoms. In Fig. 2.3, the arrows show the lateral displacements of adatoms (magnified by a factor of 10 for clarity) in both cases. It is evident from the figure that B-step atoms relax by a greater amount compared to A-step atoms in the Feibelman configuration but the relaxations are about the same in magnitude in our isolated trimer configuration. The ratio of lateral relaxation of a B-step atom (averaged over all atoms in the step) to that of an A-step atom is 1.65 in Feibelman's calculations, whereas it is only 1.03 in our isolated trimer calculations. In spite of the considerable difference in values, the ratios indicate that the lateral relaxation of B-step atoms is greater than that of A-step atoms. Since ΔE_{AB} is positive only for total relaxation, this shows that lateral relaxations alone are responsible for greater energy lowering at the B-step than at the A-step.

For the Feibelman configuration, the following physical picture emerges from our ΔE_{AB} calculations using different relaxation schemes: ΔE_{AB} is unphysically negative when atoms are forced onto their bulk positions; this does not change when relaxations are allowed only along the vertical direction (z-relaxation). However, when atoms are further allowed to relax laterally (total relaxation), the B-step atoms relax by a greater amount and hence undergo a greater reduction in energy compared to A-step atoms, resulting in positive ΔE_{AB} values very close to the experimental observations. This picture also holds true for our isolated trimer configuration except that in the case of total relaxation, the relative amounts of lateral relaxations of a- and b-trios are not enough to guarantee accurate values of ΔE_{AB}. By computing ΔE_{AB} values for these two configurations for all three (no-, z- and total) relaxation schemes, we have clearly shown that lateral relaxations of adatoms play a crucial role in obtaining accurate values of step formation energies on Pt(1 1 1). Lateral relaxations of adatoms are determined to a great extent by the local geometry of adatoms. As a result, we can say that ΔE_{AB} values depend on the local geometry of a- and b-trios. Hence, we predicted that calculations employing intermediate configurations between the isolated trimer and the Feibelman configuration should result in a range of ΔE_{AB} values. To verify this prediction, we computed ΔE_{AB} for three intermediate adatom configurations. The following section talks about the results of those calculations.

2.2.3 Effect of local geometry on trio interactions

The intermediate configurations (cf. Fig. 2.4) were chosen in such a way as to examine the dependence of lateral relaxations and hence of ΔE_{AB} values, on the following factors: (i) lateral width of the overlayer (the number of horizontal adatom stripes used to represent the adatom island or upper terrace) and (ii) the interaction between adjacent edge-atoms. From another perspective, the latter can be viewed as interactions between the kink and anti-kink pairs that define the beginning and end of the edge-atom chain along an edge. Similar to the isolated trimer configuration, all intermediate configurations were studied with a $(4 \times 4 \times 14)$ supercell and a five atomic layer thick slab with adatoms on both sides of the slab. Edge-atoms were placed on step edges to create A-kink-anti-kink pairs and B-kink-anti-kink pairs on A- and B-step edges respectively.

In decomposing the energies for all six upper configurations, we note that the additional edge-atoms increase the total energy (per repeat length along the $\hat{x}$ direction) by E_A (the kink and the anti-kink each add E_A but the overall length of the A-step is decreased by one link, subtracting E_A; hence, a net increase by E_A.) plus the number of edge-atoms times the energy of an atom in the close-packed interior of the overlayer [45]. The straight and edge-atom decorated configurations are viewed as having the same edge energies. Similarly, for the lower configurations the difference per repeat length is raised by E_B plus the number of edge-atoms times the same 2D-bulk contribution. Thus, ΔE_{AB} is just the difference in energy per repeat length of the total energy of the upper configuration and the lower one

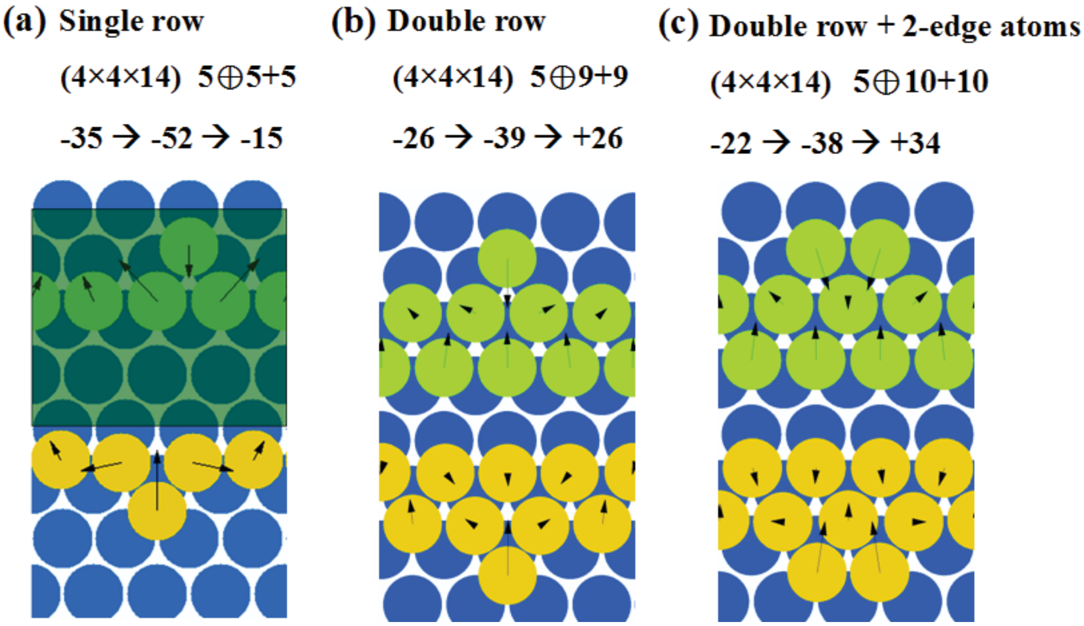

Figure 2.4: Illustration of intermediate configurations considered in our study, progressing from an atom on a chain to larger structures leading towards Feibelman configuration. The slab and adatom configurations are written using the notation introduced in Fig. 2.3. The shaded rectangle in the upper part of panel (a) illustrates the (4×4) 2D unit cell for this case.

for each pair. The results are listed in the bottom row of the tabulation in Fig. 2.4.

For kinks on two adatom-wide stripes (see Figs. 2.4(b) and 2.4(c)), the step formation energy of A-steps is greater than that of B-steps, in agreement with previous theory and experiment and similar to results using the $(8\times8\times11)$ supercell. Evidently, this is due to the lateral relaxations since this inequality does not hold for the cases of no- or z-relaxation. Comparing the intermediate configurations in Figs. 2.4(a) and 2.4(b), we can say that the addition of a row of adatoms changed ΔE_{AB} by 40 meV/atom. When there are two edge-atoms per cell (cf. Fig. 2.4(c)), symmetry no longer constrains the lateral relaxation of the edge-atoms to lie along $\hat{y}$ direction. Indeed, we see that the edge-atoms evidently attract each other modestly. This behavior can be understood from bond-energy-bond-order (BEBO) [46] arguments, since the edge-atoms have the fewest lateral neighbors. As we move across the series, the relaxations are stabilized as the overlayer structure becomes larger, and we see more clearly the asymmetry in the relaxations around edge-atoms on the two types of close-packed steps.

Comparing Figs. 2.4(c) and 2.3(b), we can see that this horizontal relaxation of end of edge-atoms becomes greater for longer chains. This attraction between edge-atoms, which favors the formation of a nascent chain along the step edge, can be recast as a repulsion between the kink and the anti-kink bounding the minichain.[6] Inspection of the upper and lower parts of Fig. 2.4(c) shows that the $\hat{x}$ component of relaxation is rather similar; correspondingly, the change in ΔE_{AB} from Fig. 2.4(b) is relatively modest. The major source of the change in ΔE_{AB} comes from the greater inward (along the $\hat{y}$ direction) relaxation at the B- vs. the A-step, as seen most clearly in Figs. 2.4(b) and 2.4(c). Compared to the double row configurations, the magnitude of relaxation along $\hat{y}$ direction is higher for the case of Feibelman configuration (cf. Fig. 2.3(b)), leading to an even larger value of ΔE_{AB}.

For the no-relaxation scheme, we get the leftmost energies in the third row of tabulated information in the figures. In all the intermediate configurations, ΔE_{AB} remains - unphysically - negative. The negativity of ΔE_{AB} does not change when only vertical relaxation is allowed. In fact, except for the isolated trimer config-

---

[6] For large edge-atom chains, we expect that the $\hat{x}$ relaxation is significant only for edge-atoms near either end of the chain. Though this would seem at first glance to then amount to a negligible finite-size correction, the prescription, described above, for computing the step energies subtracts the energies of the edge-atoms nearer the middle of the chains from those of an edge without edge-atoms, so that the values at the ends continue to be emphasized. While this feature turns out not to be crucial in the present problem, it could in principle confound straightforward assessment of step energies.

uration, the magnitude actually increases, typically by at least 50%, making the discrepancy from experiment worse. For both no- and z-relaxations schemes, the ΔE_{AB} values obtained for the two double row configurations, Figs. 2.4(b) and 2.4(c), are very close to the corresponding values for the Feibelman configuration.

2.2.4 Comparison of lateral relaxations on Cu(1 1 1) and Pt(1 1 1) surfaces

The minimal trio-based approach gives good results on Cu(1 1 1) but lateral relaxations of adatoms render the approach ineffective on Pt(1 1 1). To check whether adatom relaxations are more significant on Pt compared to Cu, we computed the inward relaxation of both A- and B-step edges using an infinitely long strip (4 atomic rows wide) of adatoms on a $(1 \times 8 \times 14)$ supercell (see Fig. 2.5(a)). For Cu, the lateral relaxations were 0.051 and 0.070 Å (ratio = 1.37) for A- and B-step edges respectively; for Pt they were about three times as large, 0.124 and 0.204 Å respectively (ratio = 1.65, same as the corresponding ratio of the Feibelman configuration). Even after accounting for the slightly larger lattice constant of Pt (3.91 Å) compared to Cu (3.64 Å), the magnitude of lateral relaxations are much higher on Pt compared to Cu .

Further, we computed ΔE_{AB} on Pt using a simple triad configuration in a minimum-size $(2 \times 3 \times 14)$ supercell shown in Fig. 2.5(b). Computations employing such minimum-size supercells normally involve suppression of adatom relaxations, resulting in distortions in the computed energy values due to frustrated relaxations.

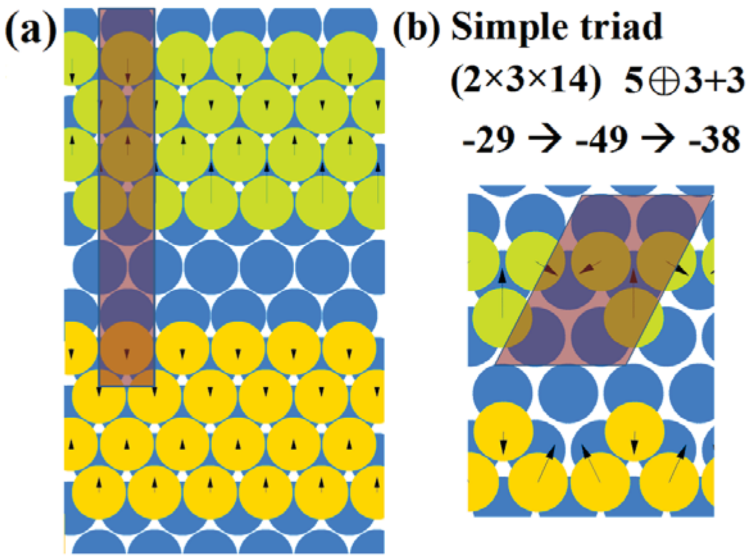

Figure 2.5: (a) Lateral relaxations of adatoms on Pt and Cu surfaces: the upper configuration (green discs) correspond to Pt atoms and the lower configuration (yellow discs) correspond to Cu atoms. The shaded parallelogram illustrates the $(1 \times 8 \times 14)$ supercell used in this calculation. (b) Computation of ΔE_{AB} using a simple triad of adatoms on a minimal $(2 \times 3 \times 14)$ supercell (shaded parallelogram). The notation used is the same as the one mentioned in Fig. 2.3. In both cases, the arrows mark the amount of lateral relaxation of atoms amplified by a factor of ten.

On the other hand, such a minimal configuration proved adequate for obtaining accurate E_A/E_B values on the Cu surface. However on Pt, our results show that for the simple triad configuration, even with total relaxation, the formation energy E_B is - unphysically - larger than E_A. Remarkably, the ΔE_{AB} value obtained with total relaxation is lower by 11 meV than the corresponding value for no-relaxation.

With the exception of a smaller kink-anti-kink separation, the simple triad configuration is identical to the single-row intermediate configuration (Fig. 2.4(a)). Even with total relaxation, the formation energy of B-steps was found to be greater than that of A-steps in both configurations. The similarity between the two configurations is also reflected in the adatom relaxations (see Figs. 2.5(b) and 2.4(a)). In spite of their similarity in relaxations, the ΔE_{AB} value is worse by 23 meV in our simple triad calculation. Due to periodic boundary conditions, the edge-atoms are separated by two atomic distances in the simple triad configuration and by four atomic distances in the single-row configuration. This results in a greater repulsion between an edge-atom and its periodicity-replicated “images” due to the evident frustration of relaxation, especially along the $\hat{x}$ direction, in the stripe in Fig. 2.5(b) compared to Fig. 2.4(a). As a result, the strength of the repulsive interaction between edge-atoms can be gauged from the difference between the ΔE_{AB} values (23 meV) obtained using these two configurations.

Our step formation energy calculations on Pt(1 1 1) show that orientation-dependent trio interactions are very sensitive to the lateral relaxations of adatoms on this surface. As a result, the simple trio-based method seems inadequate for computing ΔE_{AB} values on Pt. The lateral relaxations of adatoms are in turn dependent on the local geometry of adatoms and the size of the supercells used in the calculations. The dependence of the lattice-gas interactions on the local geometry of the adatoms brings into question one of the fundamental assumptions of the lattice-gas model. In the next two sections, we show that the sensitivity of lattice-gas interactions to local relaxations is not unique to Pt but present on other metallic surfaces too.

2.3 Step stiffness anisotropy on Cu(1 0 0)

2.3.1 Background

The stiffness of a step, denoted by $\tilde{\beta}$, is an important parameter in modeling vicinal surfaces. At equilibrium, the stiffness ($\tilde{\beta}$) determines the amount of fluctuations of an isolated step around its mean position. Dieluweit et al. [47] measured the dependence of step stiffness on Cu(1 0 0) surfaces on step orientation (θ), measured relative to the close-packed direction (cf. Fig. 1.1), using two different methods: (i) by measuring step-step distance correlation function and (ii) by analyzing equilibrium shapes of 2D islands. They found that the step stiffness decreased with the step orientation on Cu(1 0 0). They also showed that the NN Ising model is not adequate to account for the experimentally observed step stiffness anisotropy. The behavior predicted by the Ising NN model significantly underestimated the value of step stiffness for all orientations except $\langle 1\ 1\ 0\rangle$ (cf. Fig. 3 in Ref. [48]). Subsequently, Van Moere et al. [49] and Zandvliet et al. [50] proposed that an attractive NNN interaction ($E_2 < 0$) could account for the discrepancy between experimental and theoretical observations.

In an earlier work from our group, Stasevich et al. [48], using the solid-on-solid model, derived the following relation between stiffness ($\tilde{\beta}$) and step orientation (θ)

$$\frac{k_B T}{\tilde{\beta} a} = \frac{m\sqrt{(1-m)^2 + 4me^{\frac{\epsilon_2}{k_B T}}}}{(1+m^2)^{\frac{3}{2}}} \tag{2.4}$$

where a is the lattice constant, $m = \tan\theta$ and ϵ_2 is the effective NNN interaction.

Since the effective NN interaction (ϵ_1) is related to the kink formation energy (ϵ_k) through $\epsilon_1 = -2\epsilon_k$ [48], we can recast the quantity ϵ_2/k_BT in terms of the ratio of the effective NNN and NN interactions

$$\frac{\epsilon_2}{k_BT} = -2\left(\frac{\epsilon_2}{\epsilon_1}\right)\left(\frac{\epsilon_k}{k_BT}\right). \tag{2.5}$$

In the same paper, they also showed a way to include contributions from multi-site interactions to ϵ_1 and ϵ_2. Including contributions from the three-adatom right-isosceles trio (E_d) (see Fig. 2.6) merely shifts ϵ_1 and ϵ_2 by integral multiples of E_d:[7]

$$\epsilon_1 = E_1 + 2E_d \tag{2.6a}$$

$$\epsilon_2 = E_2 + E_d. \tag{2.6b}$$

The dependence of step stiffness on the step orientation for various values of the ratio ϵ_2/ϵ_1 is given in Fig. 3 of Ref. [48]. As is evident from that figure, this model requires ϵ_2/ϵ_1 to be 1/4 to correctly reproduce the experimentally observed anisotropy.

To verify this, they also computed the lattice-gas interactions between Cu adatoms on Cu(1 0 0) using DFT-based VASP [5]. They found $E_1 = -332 \pm 16$ meV, $E_2 = -47 \pm 9$ meV, yielding $E_2/E_1 \sim 1/7$, consistent with previous EAM (embedded atom method)-based modeling of the system. However, they found a large repulsive trio interaction, $E_d = 52 \pm 12$ meV, that roughly cancelled E_2,

---

[7] In contrast, including contributions from the collinear trio interaction (E_c) modifies ϵ_1 and ϵ_2 in a non-trivial manner.

resulting in $\epsilon_2 \sim 0$. Therefore, their theoretical prediction was identical to the NN Ising model which was known to be inadequate in the first place. Whereas the inclusion of an attractive NNN interaction (E_2) in the theoretical model decreases the discrepancy between theoretical prediction and experimental results in the case of Cu(1 0 0), further inclusion of the multi-site right-isosceles trio interaction (E_d) actually aggravates the discrepancy.

2.3.2 Relaxation effects in step stiffness calculations

Since our calculations showed that the strengths of trios are sensitive to adatom relaxations on Pt(1 1 1), we anticipated the presence of similar relaxation effects as the reason behind the discrepancy between theory and experimental measurements of step stiffness anisotropy on Cu(1 0 0). Our initial guess was supported by the following points about Ref. [5]: (i) the computations were carried out using small (3×2) and (4×2) unit cells, and (ii) in all the configurations that included a right-isosceles trio, adatoms were sited such that symmetry prohibits sizeable lateral relaxations. To resolve this issue, we recalculated the strength of the right-isosceles trio (E_d) using VASP but with a careful consideration of relaxation effects. We used ultrasoft pseudopotentials for Cu (with a plane-wave cut-off of 17.2 Ry) and the Perdew-Wang '91 generalized gradient approximation [40]. We used a Methfessel-Paxton width of 0.2 eV [42] to speed up the calculations. The computational parameters are the same as the ones used in Ref. [5] but we used a bigger $(4 \times 4 \times 14)$ supercell sampled by a $(5 \times 5 \times 1)$ **k**-point mesh. Our slab was five atomic layers thick and

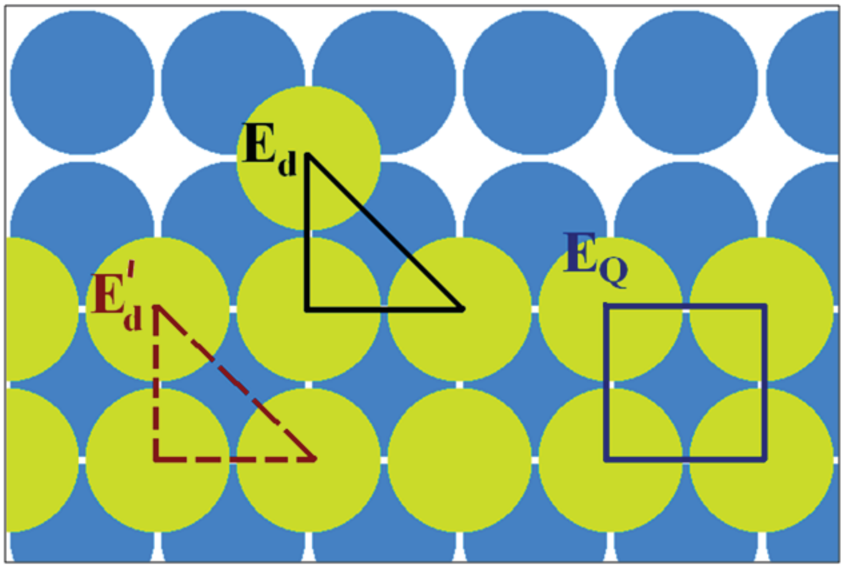

Figure 2.6: Position-dependent right-isosceles trios, E_d and E'_d, used to obtain effective NN and NNN interactions on Cu(1 0 0). Such position-dependent interactions can be accommodated into the lattice-gas picture through the introduction of a four-adatom quarto interaction (E_Q).

the rest of the supercell (equivalent to the thickness of nine atomic layers) was filled with vacuum. We placed adatoms on both the top and the bottom of the slab to eliminate any charge-transfer effects in the computed energies [44]. The middle layer of the slab was fixed, and all other layers were allowed to relax until the net force on the atoms was less than 0.01 eV/Å.

Compared to the calculations in Ref. [5], relaxation effects were incorporated into our calculations in the following ways: (i) we used a bigger supercell, which reduces the amount of frustration in adatom relaxations, and (ii) as shown in Fig. 2.6, we distinguished two types of right-isosceles trios, one in the dense interior of a (1×1) overlayer (E'_d), where symmetry precludes significant lateral relaxation, and another at the step edge (E_d), with one or two of the three atoms of the right-isosceles trio being edge-atoms with just one or two (lateral) NN bonds. Since the local geometry of these adatoms differ, we could anticipate that the associated trio interaction energies would differ. This is based on the idea that the isosceles-right trio (E_d') inside a stripe cannot relax laterally as much as the trios with vertices on the step edge (E_d). The trio interaction calculated in Ref. [5] corresponds to a linear combination of E_d' and E_d, weighted predominantly by E_d'. Since the step stiffness depends on the strengths of the interactions involving step edge atoms, it is appropriate to use the strength of E_d for computing ϵ_1 and ϵ_2. To distinguish these two trios, we calculated the energies of four different adatom configurations and solved the resultant linear system of equations. We found the difference between the energies of E_d' and E_d to be

$$E_d' - E_d = 39.5 \pm 0.5 \text{ meV}, \tag{2.7}$$

which gives the strength of the step-edge isosceles-right trio interaction

$$E_d = 12.5 \pm 0.5 \text{ meV}. \tag{2.8}$$

Using this value of E_d, we get

$$\epsilon_1 = -307 \text{ meV} \quad \text{and} \quad \epsilon_2 = -34 \text{ meV}, \tag{2.9}$$

and the ratio of the effective NNN and NN interactions then becomes

$$\frac{\epsilon_2}{\epsilon_1} \approx \frac{1}{9}. \tag{2.10}$$

The plot of the step stiffness ($\tilde{\beta}$) as a function of step orientation (θ) given in

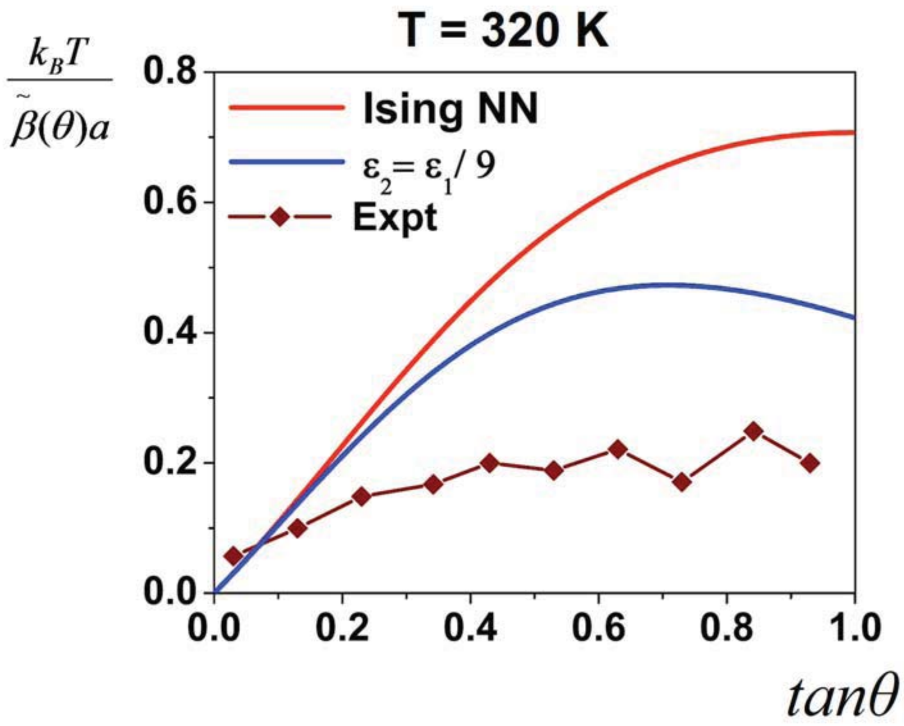

Figure 2.7: Step stiffness anisotropy on Cu(1 0 0): experimental measurements from Ref. [47] (diamonds), behavior predicted by the Ising NN model $\epsilon_2 = 0$ (red curve). The solid blue curve corresponds to the behavior for $\epsilon_2/\epsilon_1 \approx 1/9$, obtained from our computations using bigger ($4 \times 4 \times 14$) supercells and position-dependent trios.

Eq. (2.4) using this ratio is given in Fig. 2.7. As is evident from the plot, careful consideration of the relaxation effects significantly reduce the discrepancy between theoretical prediction and experimental observations of step stiffness anisotropy on Cu(1 0 0). Based on our results, it can be confidently said that with bigger supercells and thicker adatom stripes, similar to the ones employed by Feibelman in his Pt(1 1 1) calculations, the discrepancy can be narrowed down further.

To check if the strengths of pair interactions E_1 and E_2 also changed considerably with adatom relaxations, we computed the strengths of E_1 and E_2 for the cases of total and z-relaxation. To isolate the effects due to lateral relaxations alone, we placed only two adatoms (at NN or NNN positions as relevant) on both top and bottom of the supercell. Coincidentally, we find that the strengths of both E_1 and E_2 interactions increase by 8.5 meV when lateral relaxations are suppressed. This correction due to relaxation effects is negligible in the case of E_1. Even though it is a moderate correction to E_2, it is nevertheless not as important as it is for E_d. Since E_1 and E_2 are attractive, adding these corrections results in a minor shift of the theoretical prediction towards the experimental behavior. Major portion of the reduction in discrepancy between theory and experiments occurs only due to proper consideration of relaxation effects near step edges.

2.3.3 Reconciling position-dependent interactions with the lattice-gas model: Quarto interaction

Even though characterizing adatom interactions using position-dependent trios seems adequate to bridge experimental observations and theoretical calculations on Cu(1 0 0), such position-dependent interactions are not consistent with the lattice-gas picture. As mentioned earlier in section 2.1, lattice-gas interactions should not depend on local position and geometry. However, our calculations show that the two trios E_d' and E_d indeed have different interaction strengths. We can remedy this problem by introducing a four-adatom, non-pairwise and non-trio quarto interaction (E_Q) as shown in Fig. 2.6. If not included explicitly in the lattice-gas parameterization, like in the case of Ref. [5], the quarto interaction gets added to the strength of 2D-bulk trios. Hence, we get the following relation between E_Q and the two right-isosceles trios (E_d and E_d')

$$E_d' = E_d + \frac{3}{4}E_Q. \tag{2.11}$$

Using equ. (2.11), the strength of E_Q on Cu(1 0 0) was calculated to be

$$E_Q = 53 \pm 16 \text{ meV}. \tag{2.12}$$

This is a significant energy in comparison to the collinear trio E_c = -15 meV and third neighbor interaction E_3 = -8 meV. Hence, E_Q is likely to have consequences in calculations of properties related to steps. Since this quarto interaction acts to reconfine the adatoms to their laterally unrelaxed positions, it is repulsive and rather substantial. Even though the possibility of such interactions has been known for over three decades [26, 51], to the best of our knowledge, it has been invoked only once prior to our calculations on Cu(1 0 0) [52]. A recent study has shown the presence of such four-adatom quartos and even five-adatom quinto interactions on homoepitaxial Al(1 1 0) and Al(1 0 0) systems [36].

2.4 Ab-initio calculations of interactions between Cu adatoms on Cu(1 1 0)

2.4.1 Motivation

Experimental studies of Al(1 1 0) homoepitaxy have reported the formation of regular pyramidal islands (nanohuts) under certain growth conditions [53]. Using DFT calculations, Zhu et al. [54] computed the relevant diffusion barriers for understanding the mechanism behind the formation of such nanohuts. Further, mechanisms for upward self-diffusion of individual adatoms and small adatom clusters have also been found to exist on Al(1 1 0) and Cu(1 1 0) surfaces and the formation of nanohuts is predicted on Cu(1 1 0) and other fcc metal (1 1 0) surfaces [55]. Ab-initio calculations [35, 36] have shown that a large number of trio interactions of significant strengths and depending on the parameterization, strong four-atom quarto and five-atom quinto interactions are present in the case of Al adatoms on Al(1 1 0). In addition to that, among pair interactions, only NN interaction was found to be attractive whereas all cross-channel pair interactions were repulsive. As a result, the inclusion of multi-site trios in the lattice-gas parameterization was necessary to account for the formation of 2D islands and nanohuts on Al(1 1 0). Due to the more open nature of (1 1 0) surface compared to the other two high-symmetry surfaces, relaxation effects are expected to be prominent on this surface, as observed in the case of homoepitaxial Al/Al(1 1 0) system. Hence, the Cu/Cu(1 1 0) system provides an ideal system for studying the effectiveness of lattice-gas characterization in the presence of substantial relaxation effects.

As a substrate, Cu(1 1 0) finds application in the molecular self-assembly of a large number of aromatic compounds; particularly in the case of a benzoate molecule, the presence of Cu adatoms influences the orientation of the molecular assembly [56]. Ever since high magnetoresistance was found on Co/Cu [57] multilayers, Co thin-film growth on Cu surfaces has generated much interest among surface scientists due to potential applications in the field of spintronics. All of these findings make the first-principles based study of surface energetics and thin film growth on Cu(1

1 0) technologically important. To get a better understanding of nucleation and growth on Cu(1 1 0) homoepitaxy, we have also computed the diffusion barriers for the basic hops on this surface.

2.4.2 Computational Details

To compute the interactions between Cu adatoms on Cu(1 1 0), we used density-functional theory [15, 16] based VASP [17, 18, 19, 20] along with ultra-soft pseudopotentials and the Perdew-Wang '91 generalized gradient approximation (GGA) [40]. We used an energy cut-off of 17.2 Ry for the plane-wave basis set and, to speed up the calculations, a Methfessel-Paxton [42] width of 0.2 eV. We used a lattice parameter of 3.64 Å determined from a bulk calculation with a $(1 \times 1 \times 1)$ supercell sampled with an $(11 \times 11 \times 11)$ **k**-point mesh. To check for consistency in the computed energy values, we computed the energies using two supercells with different lateral dimensions - $(4 \times 4 \times 16)$ and $(5 \times 4 \times 16)$ along ([1 1 0]×[0 0 1] $\times \hat{z}$) sampled by $(4 \times 3 \times 2)$ and $(3 \times 3 \times 2)$ **k**-point meshes, respectively. Our slab was six atomic layers thick, and the rest of the supercell was filled with vacuum. In Table 2.1, we list the changes in interlayer separations for a plain slab (without any adatoms), computed using a $(4 \times 3 \times 16)$ supercell sampled by a $(4 \times 4 \times 2)$ **k**-point mesh, as a percentage of their bulk separations. The values are in good agreement with previous experimental measurements and theoretical calculations [58]. Since the interlayer separation between the third and fourth layers is very small (less than 1%, approximately 0.01 Å), we allowed only the top three layers to relax in

Table 2.1: Change in the interlayer separation between i and $i+1$ layers expressed as a percentage of the corresponding bulk value. The values were calculated using a $(4 \times 3 \times 16)$ supercell with a slab that is 10 atomic layers thick. Only the top five layers were allowed to relax; the rest of the layers were fixed at their bulk positions. The error bars inside the parentheses give the range of variation of these values for different supercells and different number of relaxing layers.

$(i, i+1)$	$\Delta d_{i,i+1}$ (%)
(1,2)	-9.7 (± 0.6)
(2,3)	+4.0 (± 0.8)
(3,4)	-1.9 (± 0.3)
(4,5)	+0.4 (± 0.4)
(5,6)	+0.08

our calculations. We put adatoms on only one side of the slab to avoid adatom interactions through the slab because the interlayer spacing for layers on a (1 1 0) surface is smaller than on (1 0 0) or (1 1 1) surfaces. Placing adatoms on only side facilitates the usage of slabs of computationally feasible thickness for surface energy calculations. Since charge transfer effects are not expected to be significant for this case, this asymmetry should not have any significant effect. All atoms were allowed to relax till the forces on them were less than 0.01 eV/Å.

We used the leave-n_ν-out cross-validation method [59] to fit the computed energies to the interaction parameters. This method is expected to perform better than the commonly used leave-1-out cross-validation scheme [59]. The interaction strengths were calculated in the following way: for a particular supercell, total energies were computed for, say, n different configurations of adatoms. In addition to that, we posit the number of significant interactions (n_i). We then use n_i (out of n) equations to solve for the interaction energies. These interactions are then used to predict the energies of the remaining n_ν ($n_\nu = n - n_i$) equations. The prediction error per adatom for a particular configuration j ($1 \leq j \leq n_\nu$) is calculated using the following equation

$$\Delta E_j = \frac{E^{pred}(j) - E^{VASP}(j)}{a_j} \tag{2.13}$$

where a_j denotes the number of adatoms in that configuration. The root mean squared (rms) value of those errors

$$\Delta E_{rms} = \sqrt{\frac{1}{n_\nu} \sum_{j=1}^{n_\nu} (\Delta E_j)^2} \tag{2.14}$$

is then calculated. This procedure is repeated for different partitions of (n,n_i), and sets of interactions from only those partitions whose ΔE_{rms} values are lower than a certain threshold value (10 meV/adatom) are considered for the final averaging of interaction values. The number of significant interactions is varied, and the one with the best convergence ($n_i = 9$ for lattice-gas model) is found. This procedure is repeated for both supercells. To test for consistency, we also present cross-validation (CV) scores (rms value of per adatom prediction errors) obtained when interaction energies computed for a particular supercell, say ($4 \times 4 \times 16$), are used to predict energies of adatom clusters in ($5 \times 4 \times 16$) supercell.

2.4.3 Lattice-gas interactions between Cu adatoms on Cu(1 1 0): Large multi-site interactions

The lattice-gas interactions of adatoms calculated using two different supercells are listed in Table 2.2. We considered six pair interactions with a maximum range of 7.28Å (twice the lattice spacing), four trio interactions and three quarto interactions. Except fifth-neighbor and sixth-neighbor interactions, all interactions that were considered are shown in Fig. 2.8. The pair interactions E_5 and E_6 were found to be very weak (around 5 meV) and including them worsened the CV scores. Three of the multi-site interactions, E_{T2}, E_{Q2} and E_{Q3}, were not found to be significant. This makes the presence of sizable five-adatom quinto interactions on this surface improbable; accordingly, we exclude them. Since E_{Q3} is small, presence of a strong collinear quinto is unlikely. Also the two quintos that can be formed by adding an adatom either along the in-channel or along the cross-channel direction to the only sizable quarto interaction, E_{Q1}, can be reasonably neglected due to the smallness of E_{Q2} and E_{C2} interactions.

The interaction energies computed using the two supercells are in very good agreement with each other. The CV scores are very low (at most 9 meV/adatom) and the maximum CV error for any case is only 23 meV/adatom (approximately k_BT at room temperature). As expected, the first-neighbor attraction is the strongest interaction on the surface. Surprisingly, the next strongest interaction is the collinear trio interaction, E_{C1}. The strong attractive nature of both interactions explain the formation of long 1D islands at low temperatures ($T < 220$ K) along the in-channel

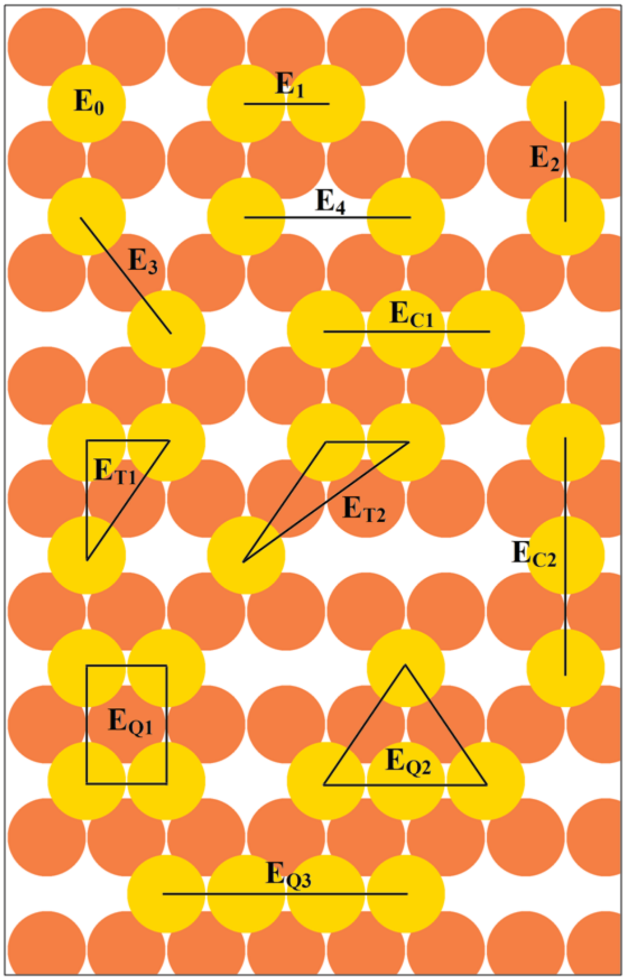

Figure 2.8: Lattice-gas interactions used to characterize Cu adatom interactions on Cu(1 1 0). In all the figures concerning Cu(1 1 0) surfaces, lighter mustard circles represent adatoms and darker orange circles represent atoms in the substrate layer. Multi-site interactions, E_{T2}, E_{Q2} and E_{Q3}, were found to be insignificant. Table 2.2 gives the values of these interaction energies for different relaxation schemes.

direction as seen by Mottet et al. [60] in their kinetic Monte Carlo simulations. Also, the computed values of E_1 and E_2 are in good agreement with their values. The other pair interactions, E_3 and E_4, are small and repulsive. Remarkably, of the five strongest interactions, three are multi-site interactions. Recently, such multi-site interactions have been found on a variety of metallic surfaces [5, 22, 30, 31, 32, 33, 34, 35, 36]. Thus, multi-site interactions become vital for constructing a complete

Table 2.2: Lattice-gas energies of Cu adatoms on Cu(1 1 0) computed using $(4 \times 4 \times 16)$ and $(5 \times 4 \times 16)$ supercells with total, z- and no-relaxation schemes [23]. All energies are given in meV and the CV values are given in meV/adatom. The numbers inside the parentheses indicate the absolute value of maximum CV error.

	Total relaxation		z-relaxation		no-relaxation	
Interactions	(4×4)	(5×4)	(4×4)	(5×4)	(4×4)	(5×4)
E_0	-3536	-3534	-3535	-3529	-3520	-3513
E_1	-223	-235	-209	-215	-230	-246
E_2	-31	-29	-35	-36	-33	-30
E_3	+5	+5	-19	-5	-7	+5
E_4	+13	0	+21	0	+19	0
E_{C1}	-60	-45	-68	-57	-71	-54
E_{C2}	-5	-10	-3	-7	-2	-6
E_{T1}	+16	+17	+20	+16	+7	+3
E_{Q1}	-30	-19	-16	-6	+24	+32
CV(4×4)	4(14)	9(23)	2(3)	9(19)	2(4)	9(19)
CV(5×4)	3(6)	2(4)	5(13)	2(4)	6(13)	2(4)

lattice-gas picture [61].

2.4.3.1 Sensitivity of lattice-gas energies to adatom relaxations

When adatoms were allowed to relax along all directions, the displacements were found to be primarily along the $\hat{z}$ direction. The percentage changes in atomic separations along the three directions due to relaxations are listed in Table 2.3. It is evident that the reductions (both percentage and absolute) in adatom separations along the $\hat{z}$ direction are much greater than the corresponding values for the two lateral directions. To assess the effect of relaxation on the interaction energies, we computed interaction strengths with z- and no-relaxation schemes. The interaction

Table 2.3: Percentage reduction in the distance between adatoms from the bulk value due to adatom relaxation. To get absolute reduction, the values should be scaled by $2a : 2\sqrt{2}a : a$ where a = 3.64 Å is the lattice spacing.

Supercells	$\Delta d_{[1\bar{1}0]}$ %	$\Delta d_{[001]}$ %	Δz %
$(4 \times 3 \times 16)$	-3.1 (%)	-1.3 (%)	-11.3 (%)
$(4 \times 4 \times 16)$	-3.0 (%)	-0.4 (%)	-11.0 (%)
$(5 \times 4 \times 16)$	-3.0 (%)	-0.3 (%)	-11.5 (%)

energies obtained for the cases of z- and no-relaxations are also given in Table 2.2.

Comparing the energy values computed using total and z-relaxation schemes helps to identify the effects of lateral relaxations on lattice-gas energies. When adatom interactions are computed using the z-relaxation scheme, almost all interaction energies, except E_3 and E_{Q1}, are close to the corresponding values obtained with total relaxation. This could be attributed to the point mentioned above about the relative magnitudes of relaxations along the three directions. It is surprising that among the pair interactions, only E_3 changes due to the suppression of lateral relaxations. Since both the interaction and the corresponding change have small magnitudes, we cannot tell whether the change is due to elastic interactions or some unaccounted-for long-range interaction. On the other hand, the decrease in the magnitude of the rectangular quarto interaction, E_{Q1}, is readily explained: E_{Q1} arises from the suppression of lateral relaxations of the trios, E_{T1}, when such trios are found in the 2D-bulk layer of adatoms rather than near island edges. The same issue for Cu(1 0 0) is discussed in detail in the previous section. Since lateral relaxations are suppressed in the z-relaxation scheme, there is no difference in the values between the E_{T1} trios near the island edges and the ones in the 2D-bulk layer. Hence, the magnitude of E_{Q1} decreases significantly in the case of z-relaxation. The CV scores for z-relaxation are as low as the ones obtained in the case of total relaxation.

Most of the interaction energies computed using the no-relaxation scheme do not differ considerably from the ones computed using z-relaxation. The only interactions whose values change remarkably are E_{T1} and E_{Q1}. Compared with the corresponding values in the case of z-relaxation, E_{T1} decreases by more than half; from a moderately strong repulsion, it becomes vanishingly small. The change is even more drastic for values of E_{Q1}. From a strong attractive interaction (comparable in magnitude to E_2) in total relaxation scheme, E_{Q1} changes to a weak attraction when lateral relaxations are suppressed and, in turn, becomes a strong repulsive interaction in the case of no-relaxation. The difference between the z- and no-relaxation schemes is that in the latter, adatoms cannot optimize the lengths of their bonds with underlying substrate atoms. Therefore, it is reasonable that the corresponding changes in interaction values are drastic for those interactions (E_{T1} and E_{Q1}) that share a common substrate atom.[8] Once again, the cases of E_{T1} and E_{Q1} stress the importance of relaxation effects while computing the strengths of multi-site interactions. At the same time, the other two multi-site interactions, E_{C1} and E_{C2}, seem insensitive to relaxation effects. Their values do not undergo any significant change under different relaxation schemes. An explanation for the insen-

---

[8] In the z-relaxation scheme, among all the atoms in the substrate layer, the atom shared by the E_{Q1} quarto adatoms, due to the highest value of its coordination number, gets closest to the adatom layer. It is followed by the substrate atom shared by the E_{T1} trio due to the same reason. The change in the interlayer separation (measured along the $\hat{z}$ direction) between the E_{Q1} quarto and the shared substrate atom is -14.7% and the corresponding change for E_{T1} trio and the shared substrate atom is -13.4%. In comparison, the change in the interlayer separation of a lone adatom and its nearest-neighbor substrate atom is -11.4%.

sitivity of such collinear trios is presented in the summary section of this chapter.

In the lattice-gas parameterization of interactions between Cu adatoms on Cu(1 1 0), certain multi-site interactions, and probably pair interactions, are found to be very sensitive to adatom relaxations. It is noteworthy that the multi-site interactions that are very sensitive to adatom relaxations, E_{T1} and hence E_{Q1}, are the ones necessary to describe energies of adatoms near island edges. These are the interactions relevant for computing experimentally verifiable physical quantities like step stiffness and island shapes. Similar to the cases of Pt(1 1 1) and Cu(1 0 0), our results on Cu(1 1 0) once again emphasize that in the lattice-gas modeling of steps, relaxation effects are crucial for making connections with experiments.

2.4.3.2 Multi-site interactions as corrections to pair interactions - discrepancy in E_4 values

In all relaxation schemes, there is a difference between E_4 values calculated using $(4 \times 4 \times 16)$ and $(5 \times 4 \times 16)$ supercells. The interaction E_4 is mildly repulsive in $(4 \times 4 \times 16)$ supercells, whereas it is negligible in $(5 \times 4 \times 16)$ supercells. This discrepancy can be understood if we consider E_4 values along with E_{C1} values in these two supercells. In the case of total relaxation, the difference in E_4 values is 13 meV with the $(4\times4\times16)$ value being higher. At the same time, their E_{C1} values differ by -15 meV. The discrepancy between these two values is not surprising because the collinear trio interaction (E_{C1}) is, in fact, a correction term to fourth-neighbor (E_4) interaction due to the presence of an adatom between the atoms that make up the pair. Also in $(5 \times 4 \times 16)$ supercells, the numbers of E_4 interactions in all of our adatom configurations are either equal or very close to the corresponding numbers of E_{C1} interactions. Thus, the difference in E_4 is compensated by E_{C1} values such that the sums of those two interactions, calculated using the two supercells, are very close to each other. The difference[9] between $E_{C1}+E_4$ values is -2 meV for total relaxation and 10 meV and 2 meV in the cases of z- and no-relaxations. Such discrepancies might arise when multi-site interactions are used as corrections to pair interactions and also when multi-site interactions that form a non-compact cluster (for example, the quarto interaction, E_{Q2}, is a compact cluster but the same arrangement without the middle atom in the bottom row is a non-compact or an open cluster.) of adatoms are used to parameterize adatom interactions. However, it does not pose a serious problem to the accuracy of the interaction energies in this case can be seen from the low CV scores.

2.4.4 Connector model characterization of adatom interactions

We also characterized the adatom interactions using the connector model [36], which was recently developed as an alternative approach to deal with the presence of many sizable multi-site interactions in a tractable way. In the connector model [36], each adatom in a cluster is mapped onto a particular connector that has the same number of each type of (first-, second-, and if necessary, third-) neighbor bonds. A more accurate model should also take into account the orientations of these bonds.

---

[9] The energy difference (ΔE) is calculated as the energy value computed using $(5 \times 4 \times 16)$ supercells subtracted from the corresponding energy value computed using $(4 \times 4 \times 16)$ supercells.

However, doing so would increase the total number of connectors needed to parameterize the interactions, thereby reducing the efficacy of the model. The energy of the cluster is then written as the sum of the connector energies. One of the main features of this model is that the type of connector contains information about the local geometry of the adatom; hence relaxation effects are expected to be built into the model. For adatom interactions on this surface, we find the number of significant interactions that gives the best convergence is n_i=10. The ten connectors used to characterize adatom interactions on Cu(1 1 0) are shown in Fig. 2.9. Since E_3 is weak, an adatom was mapped to the connector with the same number of first-neighbor and second-neighbor bonds, i.e. adatoms with only a second-neighbor bond are mapped to C_3, while those with a second-neighbor bond along with one or more third-neighbor bonds are mapped to C_{10}.

Connector energies for all three relaxation schemes are listed in Table 2.4. The CV scores are as good as those obtained using the lattice-gas approach. This success is not surprising because each of the connector energies can be expressed as a linear combination of lattice-gas energies. For example, the connector C_6 can be written as

$$C_6 = E_0 + \frac{E_1}{2} + \frac{E_2}{2} + \frac{E_3}{2} + \frac{E_{T1}}{3} + \frac{E_{Q1}}{4} \tag{2.15}$$

The sensitivity of multi-site interactions is not apparent from the connector energy values due to the following reasons - (i) each connector has contributions from adsorption energy (E_0 or C_1) and other pairwise interactions that dominate over

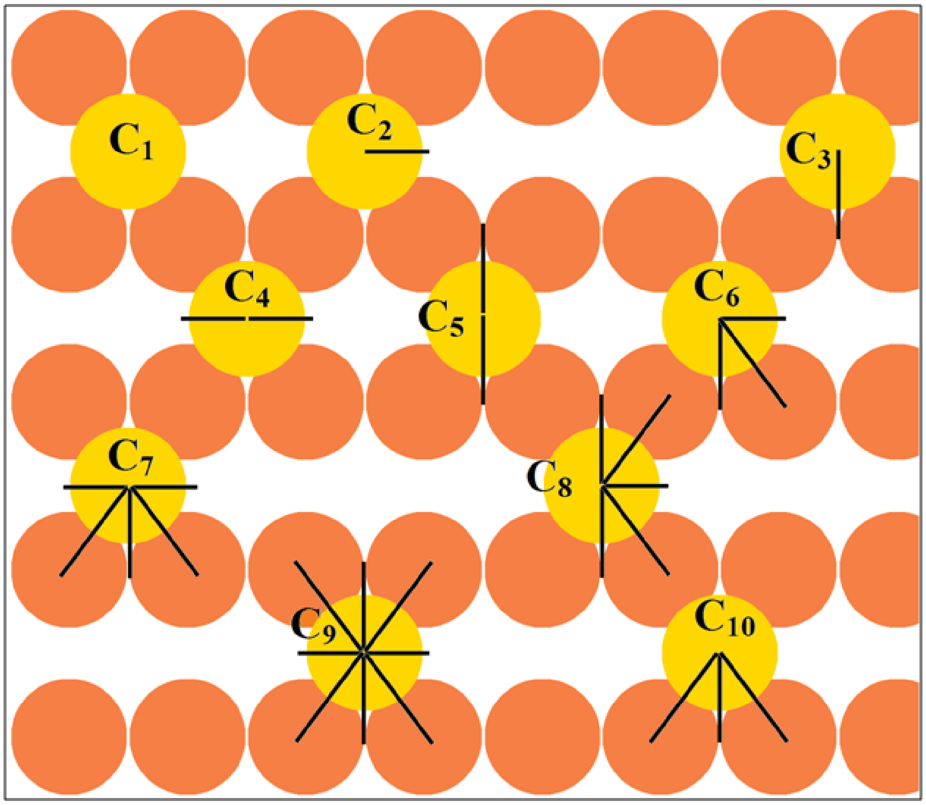

Figure 2.9: Connectors [36] used to characterize Cu adatom interactions on Cu(1 1 0). Table 2.4 gives the values of these interactions for different relaxation schemes.

contributions from multi-site interactions and (ii) also the contribution from a particular multi-site interaction is divided by the number of participating adatoms (see Eq. (2.15)), further making the sensitivity of connector energies to adatom relaxations less apparent. However, this model incorporates such relaxation effects as can be seen from the uniformly low CV scores for all relaxation schemes.

The connector model works well in the case of Cu(1 1 0), Al(1 1 0) and Al(1 0 0) [36]. It remains to be seen whether the connector model provides an adequate solution, without the need for any ad hoc patches, to the overlayer problem. Relaxation effects become prominent during energy calculations of adatoms near step edges; it is in such calculations the simple lattice-gas model runs into problems [22].

Table 2.4: Connector energies of Cu adatoms on Cu(1 1 0) computed using $(4\times4\times16)$ and $(5\times4\times16)$ supercells with total, z- and no-relaxation schemes [23]. All energies are given in meV and the CV values are given in meV/adatom. The numbers inside the parentheses indicate the absolute value of maximum CV error.

	Total relaxation		z-relaxation		no-relaxation	
Connectors	(4×4)	(5×4)	(4×4)	(5×4)	(4×4)	(5×4)
C_1	-3540	-3533	-3538	-3530	-3522	-3512
C_2	-3647	-3651	-3641	-3639	-3635	-3638
C_3	-3561	-3549	-3559	-3547	-3537	-3528
C_4	-3795	-3815	-3796	-3809	-3810	-3822
C_5	-3555	-3555	-3553	-3553	-3535	-3535
C_6	-3649	-3655	-3647	-3646	-3642	-3643
C_7	-3800	-3791	-3794	-3791	-3800	-3795
C_8	-3669	-3661	-3665	-3661	-3656	-3651
C_9	-3795	-3791	-3804	-3798	-3797	-3794
C_{10}	-3532	-3538	-3521	-3535	-3508	-3519
CV(4×4)	3(7)	9(25)	3(8)	8(21)	2(5)	7(17)
CV(5×4)	6(13)	1(3)	6(12)	2(7)	6(11)	2(5)

At the same time, accommodating the relaxation effects encountered in such calculations within the connector model might require the usage of connectors that account for the orientations of neighbor bonds, resulting in an undesirably large number of connectors in the model. A DFT-based study that compares these two models on a surface like Pt(111), where such lateral relaxation effects are known to complicate surface energy calculations, would shed some light on that matter.

2.4.5 Diffusion barriers and formation of 2D islands

Diffusion barriers for Cu adatoms on Cu(1 1 0) have been calculated using a variety of methods in the past [60, 62, 63] but, to our knowledge, not with a DFT-based method.[10] To this end, we calculated the diffusion barriers for the most common hops on a (1 1 0) surface (cf. Fig. 2.10) using the nudged elastic band (NEB) method [64, 65]. We did not compute the barriers for long jumps and correlated exchange processes that are expected to occur on this surface at high temperatures ($T > 450$K) [66] since these processes are tangential to the goals of this chapter. The anisotropic bond-breaking model describes the diffusion barriers on (1 1 0) surfaces accurately; Mottet et al. computed the barriers on Cu(1 1 0) using Rosato, Guillopé and Legrand (RGL) potentials,[11] and their results showed that the barriers computed using the anisotropic bond-breaking model approximation are very close (within 25 meV) to the directly computed barriers [60]. Hence, the diffusion barriers for the most common hops are sufficient to model growth in the low temperature ($T < 300$ K) range. Also, diffusion through metastable walk [68] and leapfrog mechanisms [69, 70] are not relevant on this surface because Cu(1 1 0) does not reconstruct. We used a $(4 \times 3 \times 16)$ supercell sampled with a $(4 \times 4 \times 2)$ **k**-point mesh. The in-channel and cross-channel hopping barriers in the case of other two bigger supercells, computed by placing an adatom at the respective bridge sites,

---

[10] Stepanyuk et al. [63] employed (VASP-GGA) to compute a few diffusion barriers for Co adatoms on Cu(1 1 0) but the barriers for diffusion of Cu adatoms were computed using molecular static (MS) calculations based on the second-moment approximation but fitted to ab-initio calculations rather than to experimental data.

[11] The attractive part of the potential is derived using the second-moment approximation to the tight-binding model and the repulsive part is assumed to be of a Born-Mayer type [67].

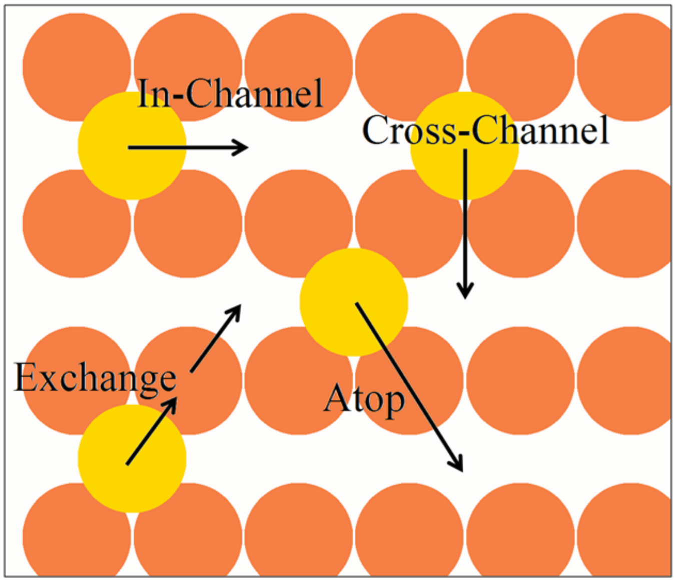

Figure 2.10: Adatom hops along high-symmetry directions on a (1 1 0) surface. The corresponding barriers are given in Table 2.5.

were found to be very close to the ones obtained using the (4 × 3 × 16) supercell. Seven images were used to sample the potential energy surface.

The obtained barriers (cf. Table 2.5) are in good agreement with previous theoretical calculations [60, 62, 63]. From the computed diffusion barriers, we can say that the in-channel hopping and the exchange are the dominant mechanisms responsible for intralayer diffusion. Our in-channel hopping and exchange barriers computed using VASP (PW91-GGA) are higher than the corresponding values from

Table 2.5: Hopping barriers calculated using the NEB method. The hops are shown in Fig. 2.10.

Hop	Barrier (eV)
In-channel	0.322
Cross-channel	1.049
Exchange	0.351
Atop	1.448

second-moment methods [60, 62, 63]. Our in-channel diffusion barrier is 0.12 eV higher than the value computed using RGL potentials [60, 62] and by about 0.06 eV higher than the value from MS calculation [63]. Similarly, the exchange barrier is about 0.05-0.1 eV higher than the values from RGL potentials and MS calculations. The reason behind the higher value of diffusion barriers in the case of VASP (PW91-GGA) is not clear. However, it should be noted that the diffusion barriers for Co on Cu(1 1 0) computed using VASP (PW91-GGA) are also higher than the corresponding values from MS calculations [63]. Even though some cross-channel interactions like E_3 and E_{T1} are repulsive, the attractive nature of E_1, E_2 and E_{C1} and the small barrier for exchange hopping lead us to expect the formation of compact 2D islands. In their kinetic Monte Carlo simulations, Mottet et al. [60] did show such formation over a suitable temperature range.

2.5 Summary and discussion

Multi-site interactions are essential for sophisticated lattice-gas modeling of steps on vicinal surfaces. Using DFT-based VASP calculations, we have shown that multi-site interactions that have significant contributions from direct interactions are very sensitive to relaxations on Pt and Cu homoepitaxial systems. In particular, BEBO [46] arguments predict that the bond lengths decrease near step edges in a way that compensates for the loss of NN atoms. As a result, adatom relaxations are expected to be substantial for step edge atoms, which complicates the accurate evaluation of multi-site interaction strengths. We showed that a straightforward application of the lattice-gas model in such situations leads to incorrect theoretical predictions.

Our calculation comparing lateral adatom relaxations on Pt and Cu(1 1 1) surfaces using a (1 × 8 × 14) supercell provides a way to detect the presence of substantial lateral relaxations near step edges. Similar calculations could provide some insight into the possibility of relaxation effects on surfaces. However, relaxations need not be along lateral directions alone. As in the case of Cu(1 1 0) [23], a major portion of atomic relaxations could take place along the vertical direction. This makes difficult an a priori prediction about the existence of relaxation effects on a particular surface. However, certain broad generalizations can be made about situations in which lateral relaxations are likely to play a part. For configurations that involve atoms that are sufficiently distant (usually second-neighbor or beyond) such that the indirect (through-substrate) interaction accounts overwhelmingly for the lateral interaction, such relaxation effects should be insignificant. Likewise, for heteroepitaxial systems in which the adatoms are much smaller than the substrate atoms, the direct interaction is likely to be unimportant even for nearest neighbors. At the same time, it would be interesting to study relaxation effects on heteroepitaxial systems in the case of a small lattice mismatch. The cases of Cu(1 1 0) [23] and Al(1 1 0) [35] show that relaxation effects are likely to be important on open surfaces, so long as the adatoms are still close enough to experience direct interactions.

In Ref. [22], we gave the following argument for the higher sensitivity of multisite interactions to relaxations compared to pair interactions: *in pair interactions, owing to symmetry, lateral relaxations must occur along the bond direction. Since* *stretching or squeezing a bond is energetically expensive, the relative position of those adatoms does not change much, thereby making pair interactions less sensitive to relaxations. However, no such symmetry constraints exist for triangular trios (*E_a *and* E_b *on Pt(1 1 1),* E_d *on Cu(1 0 0) and* E_{T1} *on Cu(1 1 0)) and quartos (*E_Q *on Cu(1 0 0) and* E_{Q1} *on Cu(1 1 0)). Hence, the participating atoms can shift by a considerable amount from their high-symmetry lattice sites along non-bond directions. This results in significant changes in their interaction strengths, thereby leading to a higher sensitivity to adatom relaxations.* The same reasoning also explains why certain multi-site interactions like E_{C1} and E_{C2} are not sensitive to adatom relaxations. Due to symmetry, the adatoms in E_{C1} and E_{C2} interactions on Cu(1 1 0) are forced to relax either along the close-packed [1 1 0] or the [0 0 1] directions, the two primary bond directions on (1 1 0). As a result, the strengths of E_{C1} and E_{C2} interactions are unaffected by adatom relaxations. In addition to that, among the pair interactions on Cu(1 1 0), only the E_3 adatom pair is not compelled by symmetry to relax along any bond directions. This could explain its fluctuations with respect to relaxation schemes.

Accounting for relaxation effects in surface energies calculations normally involves either the introduction of higher order multi-site interactions or the use of large supercells (to minimize frustrated relaxations). On Cu(1 0 0) and Al(1 1 0) surfaces, the relaxation effects could be handled efficiently through the introduction of higher-order multi-site interactions. This approach does not work in the case of Pt(1 1 1) because a four-atom parallelogram-shaped quarto interaction with NN legs consists of both an a-trio and a b-trio and hence would not be able to distinguish between the two steps.[12] To distinguish between *A*- and *B*-step atoms using compact clusters other than orientation-dependent trios, we need to introduce five-atom quinto interactions in the model. The inclusion of a large number of multi-site interaction parameters makes the lattice-gas model intractable. On Cu(1 1 0), our results show that even such higher order multi-site interactions are not immune to relaxation effects. In addition to increasing the computational cost associated with the problem, such ad hoc approaches also severely undermine the efficacy of lattice-gas models.

Our results provide a stark warning about blithely applying multi-interaction lattice-gas models to overlayer systems involving adatoms having size comparable to the substrate atoms and residing in structures with nearest-neighbor occupation. Given the fundamental place of the lattice-gas picture in modeling behavior, such complications in the model could impede its applicability to a wide variety of systems. Progress calls for imaginative approaches that go beyond ad hoc patches. The connector model provides a good alternative for the lattice-gas model on certain surfaces and holds some promise as a possible alternative for characterizing adatom interactions. However, conclusive evidence has not yet been presented to show that the connector model is immune to surface relaxation effects. We look forward to development of parameterization methods that can consistently take subtle relaxation effects on direct interactions into account.

---

[12] We consider only compact clusters because open clusters are again prone to relaxation effects.

Chapter 3

Growth instabilities on Cu vicinals: Role of metallic impurities

3.1 Background

Spontaneous pattern formation through kinetically controlled epitaxial growth provides a viable route for nanostructuring of surfaces. A thorough understanding of atomistic mechanisms along with the knowledge of relevant surface energetics is required to realize the potential of this method. The Cu surface is ideal for such growth related studies because Cu(1 0 0) and its vicinals do not reconstruct. Ernst and coworkers performed STM studies of homoepitaxial growth in the step-flow mode on Cu(0 2 24) and Cu(1 1 17) [7]. Both surfaces have 2.17 nm wide (1 0 0) terraces separated by open $\langle 0\ 0\ 1 \rangle$ (zigzag) steps on Cu(0 2 24) and close-packed $\langle 0\ 1\ 1 \rangle$ steps on Cu(1 1 17). The results of their experiments can be summarized as follows - (i) in the 250-400 K temperature range, step meandering occurs on both surfaces for deposition flux between 7.5×10^{-4} and 1×10^{-2} ML/s; the meandering wavelength (λ_m) scales with the deposition rate (F) as $\lambda_m \sim F^{-\gamma}$ with an exponent $\gamma = 0.17$ on Cu(0 2 24) and 0.21 on Cu(1 1 17), (ii) both close-packed $\langle 0\ 1\ 1 \rangle$ and open $\langle 0\ 0\ 1 \rangle$ steps undergo meandering instability and (iii) when deposition is continued beyond 10 MLs at higher flux ($F > 1 \times 10^{-2}$ ML/s), small pyramids appear on the surface [7]. The most common instability mechanism, the Bales-Zangwill instability [71], caused by the presence of a sizeable Ehrlich-Schwoebel

(ES) barrier [72, 73] (explained in detail in section 3.5), predicts $\gamma = 1/2$. In the Bales-Zangwill mechanism, the presence of a large ES barrier makes the attachment of adatoms to step edge from the terrace in front of the step edge more favorable than the attachment of atoms from the terrace behind the step edge. This asymmetry in adatom attachment makes the straight shape of the steps unstable and causes step meandering. The experimental values of $\gamma = 0.17 \pm 0.09$ on Cu(0 2 24) and $\gamma = 0.21 \pm 0.08$ on Cu(1 1 17) rule out the Bales-Zangwill mechanism as the possible source of instability.

The failure of the Bales-Zangwill mechanism to account for the observed instabilities led to the discovery of several alternate instability mechanisms [74, 75, 76, 77]. All of these alternate mechanisms rely on step edge diffusion (the dominant mode of matter transport on metallic surfaces) of atoms as the possible source of instability. Most of these models [74, 75, 76] showed that the presence of a kink Ehrlich-Schwoebel barrier is sufficient to cause step meandering. Similar to the Bales-Zangwill mechanism, the instability caused by the kink Ehrlich-Schwoebel effect (KESE) also predicts a power-law relation between the meandering wavelength (λ_m) and the deposition rate (F) with $\gamma = 1/4$. Even though this value of γ is closer to the experimental observations, KESE also predicts that open $\langle 0\ 0\ 1 \rangle$ (zigzag) steps do not undergo meandering, in contradiction to experimental observations. Subsequently, F. Nita and A. Pimpinelli [77] proposed a novel instability mechanism, namely the unhindered step-edge diffusion (USED), in which atoms diffuse along step edges in the presence of a vanishing or an extremely small kink ES barrier. The USED mechanism makes both close-packed $\langle 1\ 1\ 0 \rangle$ and open $\langle 1\ 0\ 0 \rangle$ steps susceptible to meandering. Further, with a small kink ES barrier of 0.01 eV, the USED mechanism could reproduce morphologies very similar to experimentally observed morphologies. However, the USED mechanism fails to account for the formation of pyramids. Thus, both KESE and USED mechanisms could only account for some of the key experimental observations. Also, it is known that step-edge diffusion-induced meandering dominates over ES-barrier-induced meandering only for small values of ES barrier [78]. However, low-energy electron microscopy (LEEM) experiments give an ES barrier of 0.125 eV [79], and computational estimates based on VASP give an ES barrier of 0.258 eV for close-packed steps and 0.143 eV for open steps [80]. These results severely challenge the adequacy of the KESE and the USED models in the case of Cu vicinals. As a result, a convincing explanation for the experimental observations of Ernst and co-workers [7] was missing.

Using kinetic Monte Carlo simulations on a solid-on-solid lattice, A. B-H. Hamouda et al. [81] showed that impurities codeposited on the surface (two-species model) during growth could reproduce all the experimental observations. Their simulations showed that, except for the appearance of pyramids, a combination of the Bales-Zangwill and the USED mechanisms is sufficient to reproduce experimentally observed morphologies (see Fig. 2 in Ref. [81]). However, impurity atoms are required to obtain the observed $\lambda_m - F$ scaling behavior and also to account for the formation of small pyramids. They considered only the case of (codeposited) substitutional impurities (impurities that sit at high-symmetry lattice sites like Cu atoms) in their model. Hence, the most important energetic parameters in their model are the strengths of the Cu-Cu and Cu-impurity NN bonds and the barrier for hopping between NN sites (terrace diffusion) for an isolated atom. By varying the strength of these energy parameters in simulations and comparing the results with experimental morphologies, they found that only those impurity atoms (i) *whose nearest-neighbor (NN) bond to Cu adatom is about 1.6 times the strength of the NN Cu-Cu bond* and (ii) *whose terrace diffusion barrier is greater than 1.6 times the barrier of Cu adatom could cause the observed instabilities.* Due to higher diffusion barriers and higher binding energy to Cu adatoms, impurity atoms diffuse more slowly than Cu adatoms. Also due to their stronger bonds with Cu adatoms, impurity atoms obstruct Cu adatom diffusion and shorten their diffusion length. This makes λ_m less sensitive to deposition rate (F), resulting in smaller values of the exponent γ. Also, impurity atoms act as nucleation centers for the formation of small pyramids. However, the impurity concentrations required to reproduce the experimental value of γ is 2% on Cu(1 1 17) and 0.5% on Cu(0 2 24). In spite of its reliance on impurity concentrations that are slightly above the normal values, the impurity-based mechanism remains the only model that could account for all of the experimental observations.

Kinetic Monte Carlo simulations of A. B-H. Hammouda et al. [81] have shown that the presence of impurity atoms is responsible for the observed instabilities on Cu. By computing the energy parameters in their model, i.e., NN binding energies and terrace diffusion barriers for certain candidate impurity atoms using ab initio software packages, the relevant impurity atoms could be identified. In addition to providing an answer to the long-standing puzzle of growth instabilities on Cu vicinals, knowledge about those impurity atoms could be used to achieve nanostructuring of Cu vicinals. Using DFT [15, 16]-based VASP [17, 18, 19, 20], we have computed the NN binding energy (E_{NN}) and terrace diffusion barrier (E_d) for certain candidate impurity atoms. The specifics of our VASP calculations and our results for candidate impurity atoms are given in the following section. We also present surface morphologies after deposition of 40 MLs of Cu codeposited with 2% of impurities. Section 3.3 deals with simulations of growth in the submonolayer regime in the presence of different impurity atoms. Remarkably, qualitative differences in island nucleation behavior are observed based on the type of codeposited impurity. In section 3.4, we discuss the distributions of capture-zone areas in the submonolayer growth regime. In addition to terrace diffusion, there are other adatom diffusion mechanisms on this surface, such as hopping over a step, exchanging near a step edge, and embedding on a terrace (cf. Fig. 3.7). In section 3.5, we present the barriers for these diffusion mechanisms for the most likely impurity atoms (Fe, Mn and W) and the Cu atom. A summary of our results and concluding remarks are presented in section 3.6.

3.2 What impurities are causing these instabilities?

To identify the impurity atom(s) responsible for meandering and mounding instabilities on Cu vicinals, we initially chose a set of candidate impurity atoms that consisted of both common vapor-phase impurities and heavier metallic atoms. In typical growth experiments, there are two possible sources of impurities - (i) elements like O, S, and C that are present in the vapor phase and (ii) heavier metallic impurities like Fe, Sn, and Zn from the experimental apparatus, such as sample holder, heating coil, etc. We calculated the E_{NN} and E_d values for all candidate impurity atoms using VASP [17, 18, 19, 20] with the all-electron (frozen core) projector augmented-wave (PAW) method [82]. For the exchange-correlation functional, we used the generalized gradient approximation (GGA) of Perdew, Burke, and Ernzerhof (PBE) [83] supplied with the VASP package. The PAW-PBE potentials are expected to give more accurate results than ultrasoft pseudopotentials for systems involving transition metals with a large magnetic moment and transition metals at the left side of the periodic table (e.g., Sc-Mn) [84]. The lattice constant was found to be 3.64 Å (the same value as obtained in our calculations using GGA ultrasoft pseudopotentials [22, 23]) from a bulk calculation using a $(1 \times 1 \times 1)$ supercell sampled by a $(15 \times 15 \times 15)$ **k**-point mesh. We used a $(4 \times 4 \times 14)$ supercell sampled by a $(5 \times 5 \times 1)$ **k**-point mesh. We modeled the Cu(1 0 0) surface on a slab of six atomic-layer thickness. To speed up the calculations, we used a Methfessel-Paxton width of 0.2 eV [42]. Adatoms were placed on only one side of the slab. To take into account the effects of charge-transfer, we set the IDIPOL tag to 3 [85]. The sum of dipole and quadrupole corrections were found to be on the order of a few meV (maximum correction = 6 meV) for all impurity atoms. Such a small correction is expected because of the few adatoms (a maximum of two) used in the calculations. Atoms in the bottom three layers were fixed in their bulk positions, and all other layers were allowed to relax until the net force on the atoms was less than 0.01 eV/Å. For VASP calculations involving more than one atomic species, unless specified explicitly in the INCAR file, the higher of the two ENMAX values prescribed in the POTCARs of the two species is used as the energy cut-off for the plane-wave basis set [85]. For consistency in the calculated energy values, we set the energy cut-off for the plane-wave basis to 400 eV, the highest prescribed ENMAX value [85] among all candidate impurity atoms.

The NN bond strength (E_{NN}) between an impurity atom (X) and a Cu adatom is calculated using the following formula:

$$E_{NN}(Cu - X) = E(slab \oplus Cu - X) - E(slab \oplus Cu) - E(slab \oplus X) + E(slab) \tag{3.1}$$

where $E(A)$ denotes the total energy of the configuration A. The configurations are written in the slab $\oplus$ adatom format; adatoms sit at high-symmetry lattice sites and a hyphen (-) denotes a NN bond. To compute the energy barrier for terrace diffusion (E_d), we calculated the total energy of the configuration with the adatom at a bridge site. A nudged elastic band (NEB) [64, 65] calculation for the terrace diffusion of an isolated Cu atom using seven images showed that the bridge site is indeed the saddle point along the path of terrace diffusion. The barrier for terrace diffusion (E_d) then becomes

$$E_d = E(slab \oplus X_{bridge}) - E(slab \oplus X). \tag{3.2}$$

The computed E_{NN} and E_d values for all candidate impurity atoms are listed in Table 3.1. On this surface, the strength of the Cu-Cu NN bond is 0.350 eV (very close to previous estimate based on VASP-GGA [5]), and the terrace diffusion barrier for

Cu atoms is 0.564 eV. These values are much higher than the corresponding values ($E_{NN} = 0.15$ eV and $E_d = 0.4$ eV) used in the simulations of Ref. [81]. Accordingly, no significant adatom motions were observed in the experimental temperature range. In order to simulate growth in the step-flow mode, the temperature was raised to 425 K in the simulations.[1] The raising of the temperature in simulations is reasonable because atoms deposited on surfaces during molecular-beam epitaxy initially possess kinetic energy that could help them overcome such high barriers at lower temperatures, the so-called "transient-mobility" [86, 87]. From the conditions deduced from KMC simulations in Ref. [81], the responsible impurity atoms should have a bond strength of around 0.5 eV and a diffusion barrier greater than 0.8 eV to cause the observed instabilities.

Based on their E_{NN} and E_d values the candidate impurity atoms can be classified into four sets (cf. Fig. 3.1). The sets are named using the chemical symbols of the elements in the set and the sequence of the elements in the set name is determined by their E_{NN} value. Our simulations show that codeposition of Cu with impurities from different sets results in qualitatively different surface morphologies; at the same time, codeposition of Cu with different impurities from the same set results in similar surface morphologies. All the vapor-phase impurity atoms, O, C, and S, form the first set, henceforth called OCS set in this chapter. All of these atoms, despite adsorbing strongly on Cu(1 0 0), actually repel Cu adatoms at

---

[1] The temperature used in the simulations of Ref. [81] falls in the experimental temperature range. To see significant atomic motion for the case of barriers computed using VASP, we scaled the simulation temperature (compared to the temperature used in Ref. [81]) by the same factor as the ratio of the E_d values for Cu used in the two sets of simulations. This is reasonable because the diffusion of lone Cu atoms is the predominant atomic motion in this case.

Table 3.1: Nearest-neighbor bond strengths and terrace diffusion barriers for several impurity atoms on Cu(1 0 0) computed using VASP. Within each set, the impurities are arranged based on their E_{NN} values. The values inside the parantheses are computed with an energy cut-off of 275 eV for the plane-wave basis set.

Element	E_{NN} (eV)	E_d (eV)
Cu	0.350	0.564 (0.563)
O	-0.337	0.775
C	-0.251	1.827
S	-0.119	0.900
Ag	0.277	0.309
Sn	0.307	0.432
Zn	0.312	0.314
Al	0.422	0.493
Pd	0.343	0.698
Ni	0.384	0.795
Si	0.386	0.862
Co	0.414	0.891
Fe	0.444	0.909(0.902)
Mn	0.474	0.879(0.872)
W	0.639 (0.640)	0.913 (0.895)

nearest-neighbor positions. The repulsion is strongest in the case of O. Thus, these impurity atoms do not satisfy the condition that they bind more strongly to Cu atoms. At the same time, their E_d values are very high and are well in the range expected of responsible impurities. The surface morphology after deposition of 40 MLs of Cu atoms with 2% of C impurity atoms is shown in Fig. 3.2(a). From the figure it can be seen that no mounds are formed in the presence of C impurities, and there is very little variation in the height of the surface. Morphologies obtained while doping Cu with other impurities in this set are very similar to the one shown in Fig. 3.2(a). We later learnt from Dr. Thomas Maroutian, who was involved with the experiments, that since S was a well known impurity in Cu samples during the time

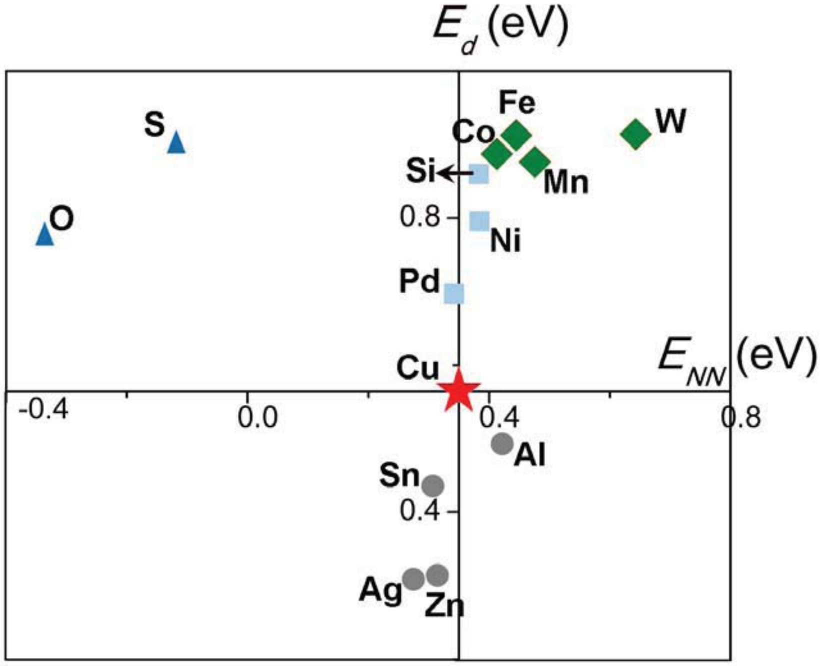

Figure 3.1: Plot of E_{NN} and E_d values for candidate impurity atoms (except C, whose values lie beyond the range of this plot) relative to the values for Cu (origin). Each set is marked with a distinct symbol: blue triangles - OCS impurities, grey discs - AgSnZnAl impurities, cyan squares - PdNiSi impurities and green diamonds - CoFeMnW impurities.

this set of experiments was performed, the sample was desulfurized carefully; hence, sulfur could not have caused the instabilities, which is consistent with our results. These results conclusively show that vapor phase impurities are not responsible for the growth instabilities on Cu observed in experiments.

The second set consists of the elements Ag, Sn, Zn, and Al. The E_{NN} (with the exception of Al) and E_d values of all the atoms in the AgSnZnAl set are smaller than the corresponding values for Cu. The electronic configuration of all elements in this set consists of either a completely filled d-orbital or a no valence d-orbital (Al). Similar to the case of pure Cu, smooth layer-by-layer growth occurs when one of these impurity atoms is codeposited with Cu. Also, no mounds form when

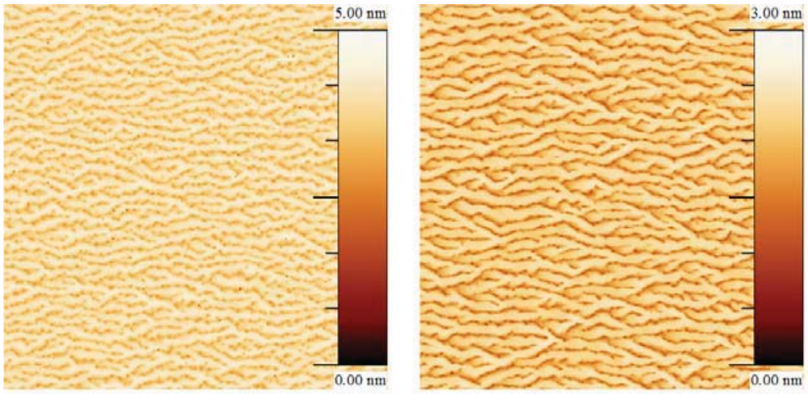

(a) Cu+C **(b) Cu+Al**

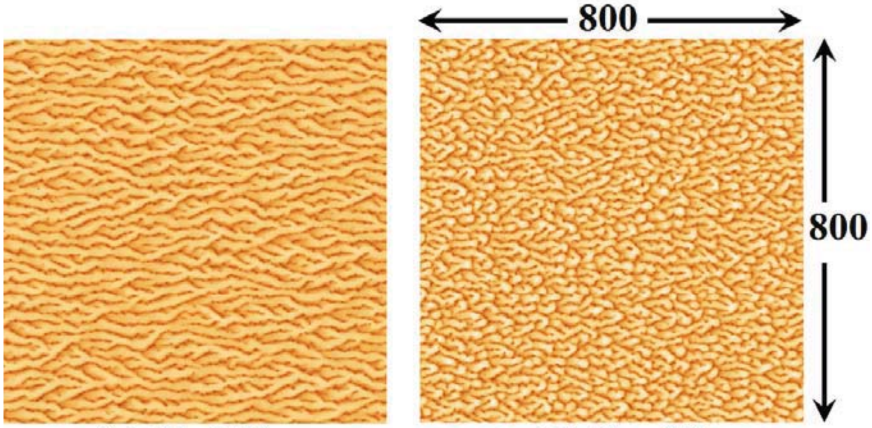

(c) Cu+Ni **(d) Cu+W**

Figure 3.2: Surface morphologies from our kinetic Monte Carlo simulations after deposition of 40 MLs of Cu with 2% of (a) C, (b) Al, (c) Ni, and (d) W impurity atoms. The color scheme covers a height range of 0-5 nm in (a) and 0-3 nm in all other panels. The lateral dimensions of the panels are 800 × 800 in units of lattice spacings (1 lattice spacing = 2.57 Å). Similar morphologies are obtained if a particular impurity is replaced by another impurity from the same set.

any of these metallic impurities are codeposited on the surface during growth (see Fig. 3.2(b)). The E_{NN} values of elements in the PdNiSi set are close to the E_{NN} value of Cu but their diffusion barriers are higher than (1.25-1.5 times) that of Cu. Except for Si, the other elements in this set have nearly filled d-orbitals. Again no mounds form during the codeposition of impurities in this set. The surface morphology obtained with Ni impurity (see Fig. 3.2(c)) is very similar to the one obtained with Al impurity. The main difference lies in the smaller meandering wavelength in the case of the PdNiSi set of impurities compared to AgSnZnAl set of impurities.

The last set of impurities consists of the mid-transition elements Co, Fe, Mn and W, hence called CoFeMnW set. Their E_{NN} values are higher than that of Cu and their E_d values fall in the range expected of impurity atoms. Of the four atoms, only W has E_{NN} and E_d values expected of responsible impurity atoms. At the same time, square-shaped pyramids form on the surface for all impurity atoms in this set except Co. Even though the energies for Co are comparable to those of Fe and Mn, fewer mounds appear during its codeposition with Cu. Whether this is due to the lower E_{NN} value of Co or due to an unsuitable temperature range in the simulations is not clear. It could also be due to the fact that the E_{NN} and E_d values for Co are close to those of Ni. A higher E_d barrier does not make a big difference, since impurity atoms are mostly immobile in the simulations. As a result, Co could equally well be categorized in the PdNiSi set. An analysis of whether Co actually belongs to the CoFeMnW set is tangential to the goal of this study. Fig. 3.2(d) shows the morphology obtained when Cu is codeposited with W atoms. This simulated surface morphology is very similar to the one obtained in experiments (cf. Fig. 3(c) in Ref. [7]). The impurity concentration of 2% is much higher than the typical impurity concentrations in experiments. At the same time, the areal density of pyramids in Fig. 3.2(d) is also much higher than the areal density observed in the experiments. Hence, experimentally observed surface morphologies could be obtained at much lower (less than 1% impurity).

From our VASP calculations and KMC simulations, we have narrowed down the possible set of impurity atoms to Fe, Mn and W. Further narrowing down is possible only with more information regarding the experiments. There are two possible sources of the impurities - (i) impurity atoms from the source that were activated at higher temperatures and (ii) impurities from the experimental apparatus. If the impurities really originated from the source, no further narrowing down is possible because the exact composition of the sample is very difficult to ascertain. However, if the responsible impurities originated from the experimental apparatus, then W and Fe have a higher chance than Mn of being the responsible impurity atom. In fact, Dr. Thomas Maroutian has confirmed that a W heating element was indeed used in the experiments. Further evidence in favor of W comes from the fact that in the experiments, pyramids begin to appear only when deposition flux is greater than 1×10^{-2} ML/s. A higher deposition flux is attained by raising the temperature of the source and an increase in the temperature of the heating element results in the evaporation of more W atoms from the wire. All of these points indicate that W atoms from the heating element are most likely responsible for the observed instabilities on Cu vicinals.

Our results show that impurity atoms codeposited during growth can significantly affect the resultant surface morphologies. Depending on their E_{NN} and E_d values relative to the corresponding values for Cu, codeposition of these impurity atoms results in specific surface morphologies. Thus, by computing the E_{NN} and E_d values for any element, we can predict the morphologies that would result during the codeposition of Cu with a small concentration of atoms of that particular element. Even though this study concerns only the case of impurities on Cu, these results can be easily extended to other metallic surfaces. Our results show that by introducing the right type of impurity during growth, we can manipulate the resulting surface morphology. Attaining the ability to manipulate resultant morphologies is an important step towards achieving nanostructuring of vicinal surfaces. From Fig. 3.2, it is very clear that surface morphologies obtained after 40 MLs of deposition of Cu with impurity atoms from different sets are different from each other. To explore if such differences in morphologies are already present at early stages of island nucleation, we simulated island growth in the presence of impurities in the submonolayer regime. Our results are presented in the next section.

3.3 Island nucleation in the presence of impurities

To study the early stages of island nucleation in the presence of impurities, we simulated surface morphologies for coverage (θ) up to 0.7 ML. In the submonolayer regime, deposition of pure Cu results in the formation of monatomic height islands. Fig. 3.3(a) shows the surface at 0.3 ML coverage. For the case of pure Cu, nucleation in the second layer is very rare for $\theta \leq 0.7$ ML. This behavior is consistent with the layer-by-layer growth observed in the step-flow mode for Cu. At the temperature used in our simulations (T = 425 K), Cu atoms diffuse freely on the surface and combine with already nucleated islands. The number of islands (N_i) shows little variation with θ (cf. Fig. 3.4(a)), whereas the average island size[2] (AIS) increases linearly with θ (cf. Fig. 3.4(b)). For $\theta > 0.4$ ML, N_i decreases with θ, indicating the

---

[2] The island size is the areal spread of the island at the first layer measured in units of lattice sites. Since the atoms in the second layer are not considered, this is not equal to the number of atoms in islands.

onset of coalescence of islands. Since the barriers for impurities in the AgSnZnAl are smaller than the corresponding barriers for Cu, codepositing 2% of Zn or Al impurities with Cu also leads to qualitatively similar results. Similar to the case of pure Cu, nucleation in the second layer is very rare for Cu codeposited with AgSnZnAl impurities (see Fig. 3.3(c)). Also, the variation of N_i with θ in the presence of these two impurities is very similar to the behavior observed for pure Cu. For all coverages, the AIS obtained with the codeposition of either Zn or Al impurities is very close to the value obtained for pure Cu (cf. Fig. 3.4(b)). Fig. 3.3(b) shows that Al atoms are located in the interior of Cu islands.

In the case of C and O impurities, N_i increases rapidly with θ throughout the regime. Since O and C repel Cu atoms at NN positions, they separate from Cu islands. Both impurities have very high barriers for terrace diffusion; hence, they remain immobile at the simulation temperature. As a result, the surface consists of two types of adatom structures - (i) large Cu islands with very few O or C atoms in them and (ii) single O or C atoms (see Fig. 3.3(b)). For all coverages, single-atom islands form a huge proportion (approximately 60-88%) of the total number of islands. Further, the proportion of single-atom islands[3] increases with θ. When Ni or Si atoms (impurities from the PdNiSi set) are codeposited with Cu, N_i increases linearly with θ for small coverages ($\theta \leq 0.3$ ML) and remains almost constant in the $0.4 \leq \theta \leq 0.5$ ML regime. Beyond a certain coverage ($\theta = 0.5$ for Ni, 0.6 for Si), coalescence sets in, resulting in a decrease in N_i with θ. This behavior is very

---

[3] Since single O or C atoms remain isolated irrespective of θ, we treat them as single-atom islands throughout this study. Treating them as islands also provides notational ease during the characterization of capture-zone areas (see following section).

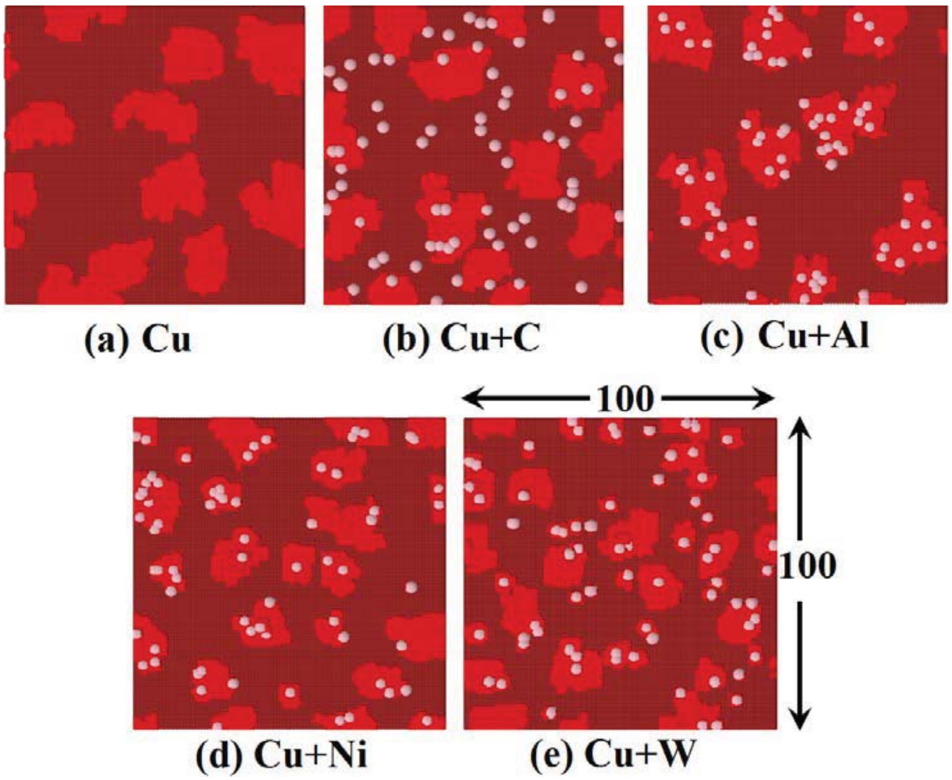

Figure 3.3: Surface morphologies after a deposition of 0.3 ML of (a) pure Cu and Cu codeposited with 2% of (b) C, (c) Al, (d) Ni, and (d) W impurities. The darker (brown) atoms denote substrate atoms, the lighter (bright red) atoms denote Cu adatoms and the pale (whitish-gray) atoms on the adatom layer are the impurities. The lateral dimensions of the panels are 100 × 100 in units of lattice spacings (1 lattice spacing = 2.57 Å).

similar to the cases of pure Cu and Cu with AgSnZnAl impurities. Fig. 3.3(d) shows that the islands are smaller compared to the case of pure Cu which is also reflected in the smaller values of average island size compared to the case of pure Cu (see Fig. 3.4(a)). As is clear from Fig. 3.3(d), Ni impurities are found inside the islands.

Island nucleation behavior in the submonolayer regime is very similar for the cases of Fe, Mn and W impurities. The N_i and AIS values for both Fe and W impurities are close to each other for all coverages (see Fig. 3.4). For both cases, N_i increases with coverage (θ) but the rate of increase becomes smaller with coverage

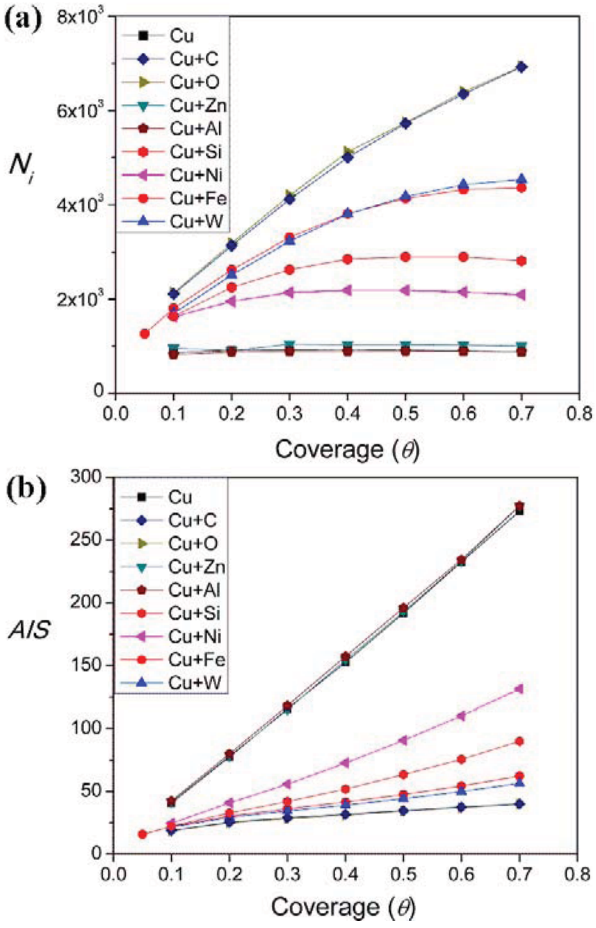

Figure 3.4: Dependence of (a) number of islands (N_i) and (b) average island size (AIS) on coverage (θ).

(θ). For neither impurity does coalescence of islands occur. Similar behavior is observed for Mn impurities but coalescence sets in near our highest examined coverage ($\theta = 0.6$ ML). As is clear from Fig. 3.3(e), many small islands (≤ 10 atoms) form on the surface during the codeposition of W impurities. Such small islands also form for Fe impurities, as reflected in the much smaller (compared to pure Cu) AIS values.[4] All of these small islands contain an impurity atom, which shows that

---

[4] The proportion of small islands ($\leq$ 10 atoms) to the total number of islands is 26-35% for Cu with W impurities, 24-38% for Cu with Fe impurities and 18-38 % for Cu with Mn impurities but it is only 2-11 % for pure Cu. The proportion monotonically decreases with θ for all of these cases, and the lower end of the values correspond to $\theta = 0.7$ ML.

impurities act as nucleation centers for the formation of islands.

Some limited nucleation occurs in the second layer in the cases of PdNiSi and CoFeMnW set impurities and extremely rare instances of third layer nucleation occurs only for CoFeMnW set impurity atoms at high coverages ($\theta \geq 0.5$ ML). Neglecting the case of OCS impurities in which the presence of single-atom islands clouds the picture, our results show that higher E_{NN} values between Cu and impurity atom leads to higher N_i values at all coverages (cf. Fig. 3.4(a)), consistent with the results in Ref. [88]. Our KMC simulations have shown that distinct island nucleation behavior is obtained depending on the type of impurity codeposited with Cu. In addition to that, the panels in Fig. 3.4 show that similar behavior is obtained when Cu is codeposited with two different impurities from the same set, justifying our characterization of impurities into sets. To further quantify the differences in island nucleation behavior, we have also computed the distribution of capture-zone areas. The following section discusses these distributions.

3.4 Distribution of capture-zone areas

One of the important parameters in characterizing submonolayer epitaxial growth is the critical-nucleus size (i), i.e., the size of the largest unstable island on that surface. The value of i depends on quantities like the bond strength, temperature and deposition flux (F). Studies based on simulations have shown that i uniquely determines the island-size distribution (ISD) [89]. This connection led to several, albeit unsuccessful, attempts at finding an analytic expression for describing ISDs. A simple description for ISDs has remained elusive due to the following reasons - (i) the mean-field nature of the approach that neglects spatial fluctuations in island sizes and (ii) the dependence of ISD on the ratio of the monomer diffusion coefficient (D) to that of the deposition flux (F). To overcome these difficulties, Mulheran and Blackman [90] proposed an alternative approach to extract i from the distribution of capture zone[5] (CZ) areas. However, due to the complexity involved in extracting i in this approach, a semi-empirical formula was normally used to extract i from experimental data.

Random matrix theory has been very successful in handling fluctuations in energy-level spacings [91], and the Wigner surmise [92] derived using random matrix ideas gives an excellent description of spacing distributions in a wide range of physical systems [91, 93]. In the field of surface science, the Wigner distribution was generalized to describe the terrace-width distributions of steps [9]; this approach provides a direct way to measure the step-step interaction strength. Chapter 4 deals with this issue in greater detail. Recently, Pimpinelli et al. [93] showed that the fluctuations in the CZ areas are similar to the fluctuations in level spacings and that the generalized Wigner distribution (GWD)

$$P_\beta(s) = a_\beta s^\beta \mathrm{e}^{-b_\beta s^2}, \quad b_\beta = \left[\frac{\Gamma(\frac{\beta+2}{2})}{\Gamma(\frac{\beta+1}{2})}\right]^2, \; a_\beta = \frac{2b_\beta^{(\beta+1)/2}}{\Gamma(\frac{\beta+1}{2})} \tag{3.3}$$

gives an excellent description of CZ area distribution during island growth. The constants b_β and a_β are fixed by the conditions of unit-mean and normalization.The fit parameter (β) is related to the critical-nucleus size (i)

---

[5] Capture zones are Voronoi polygons built around the nucleation centers of islands.

$$\beta = \frac{2}{d}(i+1) \tag{3.4}$$

where d is the spatial dimension for 1D and 2D systems.[6] The GWD gives an excellent fit for the CZ areas for data from both simulations [93] and experiments [94, 96]. At the same time, the single-parameter gamma distribution ($\Pi_\alpha(s) = \frac{\alpha^\alpha}{\Gamma(\alpha)} s^{\alpha-1} e^{-\alpha s}$) gives a comparably good description of the distribution of CZ areas. In 1D, the spacing distribution of N interacting particles is determined by the range of interparticle interaction - interaction up to nearest-neighbors results in the single-parameter gamma distribution ($\Pi_\alpha(s)$) whereas an infinite-range interaction results in GWD [97]. Since it is hard to identify the range of interaction in the case of CZs, no formal justification can be made for the choice of fitting function. Also, it is very hard to identify the correct fitting function based on the quality of fits. Nevertheless the GWD fit is preferable due to a simple connection between the fit parameter (β) and the critical-nucleus size (i). In the case of the gamma distribution, there is no way, to the best of our knowledge, to extract physical information about the system from the fit parameter α.

Even though Eq. (3.4) was derived for the case of deposition of a single species, it provided useful insights regarding the nucleation of pentacene islands in the presence of pentacenequinone impurities [96]. Also, the GWD gives a very good fit for the areas of CZs constructed around InAs quantum dots on GaAs [94]. One of the problems involved in extending the GW-based approach to two-species deposition is the ambiguity in the definition of i. For impurities on Cu, this issue is especially

---

[6] $d = 2$ in 3D but its value in 4D is unclear [94, 95].

Table 3.2: The values of β obtained from the GW fits to our simulation data. The impurity concentration is 2%. The values in bold font correspond to the island coalescence regime.

θ(ML)→	0.05	0.1	0.2	0.3	0.4	0.5	0.6	0.7
Cu	-	4.5	4.4	4.7	5.3	**6.0**	**6.2**	**6.0**
Cu + O	-	1.9	1.6	1.7	1.4	1.3	1.2	1.1
Cu + O	-	1.9	1.7	1.6	1.7	1.5	1.4	1.4
Cu + Zn	-	4.5	5.7	5.6	6.5	**6.7**	**7.2**	**7.1**
Cu + Al	-	5.2	5.3	5.8	6.0	6.2	**6.3**	**7.0**
Cu + Ni	-	2.9	3.5	3.8	4.5	**4.9**	**5.5**	**5.9**
Cu + Si	-	2.5	2.7	3.3	3.5	**4.0**	**4.3**	**4.9**
Cu + Fe	2.3	2.1	2.2	2.4	2.9	3.1	3.3	3.5
Cu + Mn	2.2	2.0	2.4	2.5	3.1	3.0	3.5	3.6
Cu + W	-	2.2	2.0	2.3	2.6	2.7	2.8	2.9

important for the OCS and the CoFeMnW set impurities, whose E_d values are much higher than that of Cu atoms. Due to very high diffusion barriers, codeposition of these impurities leads to the formation of either single-atom (in the case of OCS impurities) or few atom (CoFeMnW set impurities) islands on the surface along with large islands. In addition to that, the GW formalism is applicable only during the early stages of nucleation, i.e., before the onset of coalescence. In spite of these issues, our results show that the GWD gives a very good fit to our data (cf. Fig. 3.5). The fits are good even for coverages beyond the onset of coalescence of islands. To determine the fit parameter (β) we used the non-linear fitting function in MATHEMATICA®. All the data points were weighed equally in obtaining the fits. The β values obtained from our fits are listed in Table 3.2. The variation of β with coverage (θ) is plotted in Fig. 3.6.

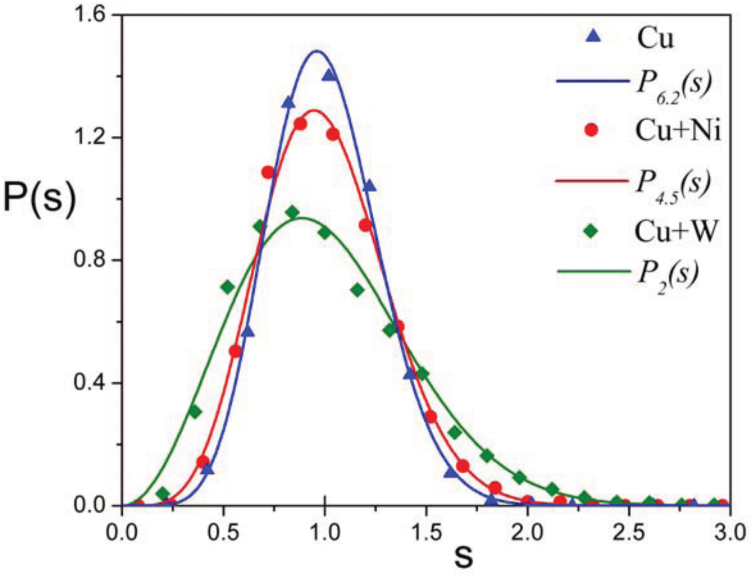

Figure 3.5: Distribution of CZ areas from our simulations (symbols) fitted with the GWD (solid curves): pure Cu at $\theta = 0.6$ ML (blue triangles) fitted with $P_{6.2}(s)$ (blue curve), Cu with 2% Ni impurities at $\theta = 0.4$ ML (red circles) fitted with $P_{4.5}(s)$ (red curve) and Cu with 2% W impurities at $\theta = 0.2$ ML (green diamonds) fitted with $P_2(s)$ (green curve). The case of pure Cu at $\theta = 0.6$ ML falls in the coalescence regime.

Certain interesting results emerge from the GW fits to our simulation data (refer Table 3.2). Except for the case of OCS impurities, β tends to increase monotonically with θ. For pure Cu, β remains a constant during the initial stages of nucleation. From Eq. (3.4), we see that i lies between 3 and 4 for $\theta \leq 0.4$ ML. The fit parameter β continues to increase for θ above 0.4 ML (coalescence regime). Similar trends are obtained for Zn and Al impurities. For the same coverage, the β values for AgSnZnAl impurities are slightly higher than the corresponding value for pure Cu, which implies an increase in i value during the codeposition of AgSnZnAl impurities. This increase in i is due to the higher mobility of AgSnZnAl impurities compared to Cu atoms. For OCS impurities, β decreases with coverage throughout the regime. The β values for O and C impurities lie between 1 and 2, denoting a

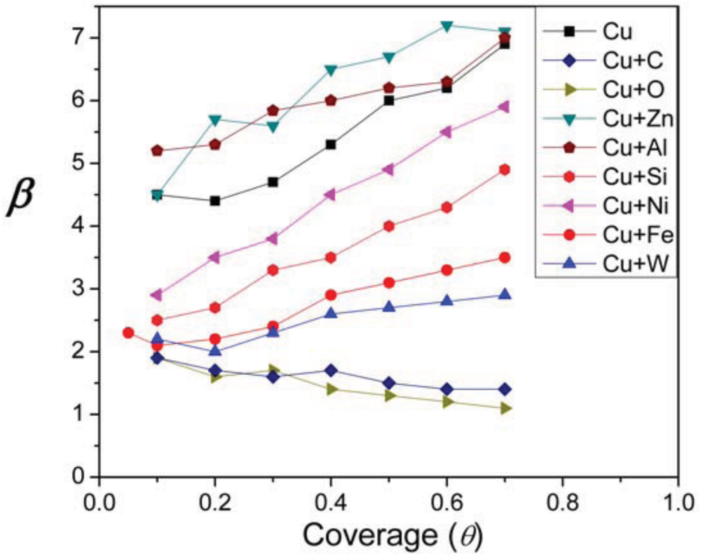

Figure 3.6: Dependence of β on coverage (θ) when Cu is codeposited with 2% of impurity atoms.

critical-nucleus size between 0 and 1. The value of β gets closer to 1 as coverage is increased. As is clear from Fig. 3.3(b), the surface consists of many single-impurity-atom islands interspersed with large Cu islands. Hence, the critical-nucleus size (i) becomes a weighted average of the corresponding value for these impurities ($i = 0$) and the value for Cu ($3 < i < 4$). Since the proportion of single-impurity-atom islands increases with coverage, i is weighed more by the value for impurities and hence shifts towards 0 for higher θ. This results in a decrease in β values with θ.

For the CoFeMnW set impurities, the obtained β values are much less (by 2-4) than those for pure Cu, indicating a significant reduction in the critical-nucleus size. This reduction in i is understandable because the CoFeMnW impurities have higher barriers for diffusion, and hence, are immobile at the experimental temperature range. Due to stronger bonds with Cu atoms, these impurities act as nucleation centers for the formation of islands, as reflected in the large number of small islands in Fig. 3.3(e). Hence, similar to the OCS impurities, $i = 0$ for the CoFeMnW impurities. Since they do not separate from Cu islands, unlike OCS impurities, the behavior of β with θ for the CoFeMnW impurities is similar to the cases of Cu with AgSnZnAl, PdNiSi impurities and pure Cu. For all coverages, the β values for PdNiSi impurities lie between the β values for pure Cu and those for Cu with CoFeMnW impurities. The PdNiSi impurities have higher barriers for diffusion than Cu and hence, have a smaller i value than Cu. At the same time, unlike CoFeMnW impurities, they are not immobile at the simulation temperature, which is also confirmed by the absence of small islands in the case of Ni impurity (cf. Fig. 3.3(d)). Application of the GW-formalism developed in Ref. [93] provides valuable insights about early stages of island nucleation for the case of impurities on Cu. Once again, similar behavior is obtained for codeposition of impurities from the same set.

3.5 Embedding, Exchange, Hopping and Ehrlich-Schwoebel barriers

As mentioned in section 3.2, the E_d values for all candidate impurity atoms listed in Table 3.1 were computed as the difference in energies between the configuration in which the impurity atom is at a FCC site and the configuration in which the impurity atom is at a bridge site. Since a nudged elastic band (NEB) [64, 65] calculation for the terrace diffusion of a Cu atom showed that the bridge site is the point of highest energy, we did not perform NEB-based computations of E_d for all impurity atoms to minimize the expense of computational resources. In this section, we present the results of our NEB calculations of E_d for Fe, Mn and W. In addition to terrace diffusion, there are other adatom diffusion mechanisms, such as embedding, hopping over a step-edge, and exchange near a step-edge (cf. Fig. 3.7) through which adatom transport takes place on vicinal surfaces. The NEB method [64, 65] implemented in VASP provides a useful way to compute the barriers for these diffusion mechanisms.

The embedding process is a concerted diffusion process involving an adatom and one of its NN substrate atoms (cf. Fig. 3.7). During embedding, an adatom displaces one of its NN substrate atoms and gets embedded in the substrate layer while the substrate atom is pushed to the adatom layer. For homoepitaxial systems, this process leads to no net energy change. However when impurity adatoms that bind more (less) strongly to Cu atoms undergo embedding, it results in a reduction (increase) in the total energy of the system because four lateral Cu-Cu NN bonds are replaced by four Cu-impurity NN bonds during embedding. The embedding of adatoms in the substrate layer plays an important role during the early stages of nucleation. For instance, the embedding process leads to a reduction in total energy for a system of Co adatoms on Cu(1 1 0), and the embedding barrier for Co adatoms was found to be comparable to their in-channel diffusion barrier [63]. As a result, Co adatoms undergo embedding upon deposition and act as nucleation centers for displaced Cu atoms. This behavior was crucial to explain the paramagnetic behavior of Co thin films on Cu(1 1 0) [63]. Since Fe, Mn and W bind more strongly to Cu atoms, embedding of these atoms leads to a decrease in the total energy of the system. If their embedding barriers (E_{emb}) are not higher than their respective terrace diffusion (E_d) barriers, these atoms could undergo embedding upon deposi-

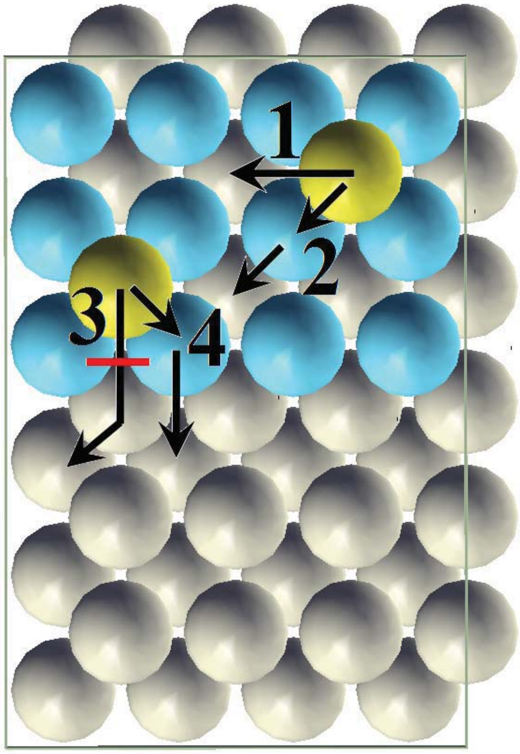

Figure 3.7: Adatom diffusion mechanisms on a (1 0 0) surface: (1) terrace diffusion, (2) embedding process, (3) hopping over a step, and (4) exchange process. The green atoms represent the diffusing adatom, the blue atoms represent the topmost layer of the substrate and the grey atoms represent atoms in the slab. The point of intersection of the hopping path (3) and the horizontal line (red line) marks the saddle point for this process.

tion. Once embedded, due to lower energies in the embedded state, these impurities remain embedded and act as nucleation centers for the growth of pyramids. This further strengthens the connection between impurity atoms and nucleation centers for pyramids. Thus, it becomes important to compute E_{emb} values for all of these impurity atoms.

One of the important parameters in KMC simulations of growth in the step-flow mode is the ES barrier. The ES barrier is the extra energy required to diffuse across a step edge (from an upper terrace to a lower terrace) compared to diffusion on a flat terrace

$$E_{ES} = E_{hop} - E_d. \tag{3.5}$$

As mentioned earlier, a high ES barrier would rule out step-edge diffusion-induced meandering as the dominant instability mechanism on this surface [78]. Hence, a high ES barrier, if found, would exclude the KESE and the USED mechanisms as the possible instability mechanism on this surface. Prior to the computation of actual ES barriers, an ES barrier about half the strength of E_{NN} for Cu was assumed for both Cu and impurity atoms in the simulations. In the case of Cu, this value ($E_{ES} = 0.175$ eV) is very close to a previous calculation of E_{ES} using VASP [98]. In addition to hopping over a step, adatoms also diffuse to a lower terrace through an exchange process (cf. Fig. 3.7). The relative magnitudes of the hopping and exchange barriers determine the dominant adatom diffusion mechanism between neighboring terraces. One of the experimental features that is absent from the KMC simulations of Ref. [81] is the alignment of the pyramids along the step direction. Since impurities act as nucleation centers for the growth of pyramids, the diffusion of impurity atoms near the step edge could explain this minor discrepancy between experimental observations and KMC simulations. Among these diffusion mechanisms, only terrace diffusion and hopping over step edges are considered in the KMC simulations of Ref. [81] and this study. Since both embedding and exchange diffusion processes are concerted two-atom processes, it is harder to incorporate them in kinetic Monte Carlo simulations; accordingly, they were neglected in our simulations. For a complete understanding of the step-flow growth on Cu vicinals in the presence of impurities, it is important to include these diffusion mechanisms for both Cu atom and impurity atoms in our study. This section discusses the results of our barrier calculations for hopping (E_{hop}), embedding (E_{emb}) and exchange (E_{exc}) processes.

To compute the terrace diffusion (E_d) and embedding (E_{emb}) barriers, we used a $(4\times6\times14)$ supercell and sampled it with a $(4\times3\times1)$ **k**-point mesh. We used a slab that is six atomic layers thick, with the bottom three layers fixed, and all other layers were allowed to relax until the net force on the atoms was less than 0.01 eV/Å. Since Cu and the three impurity atoms are all transition metals, a high energy cut-off of 400 eV for the plane-wave basis set is not required to obtain reasonably accurate values. The ENCUT values mentioned in the respective POTCAR files for all three atoms fall in the 223-273.2 eV range. Hence, we used an energy cut-off of 275 eV for the plane wave basis set in these calculations. To check that reducing the energy cut-off does not affect the accuracy of the computed energy values significantly, we recalculated E_d values for Cu, Fe, Mn and W on a $(4 \times 4 \times 14)$ supercell with an energy cut-off of 275 eV. The results are listed inside the parentheses in Table 3.1. Since the recalculated E_d values are very close (maximum difference of 18 meV, within 2% difference) to the values computed with 400 eV cut-off, an energy cut-off of 275 eV was deemed sufficient for the barrier calculations. All of the diffusion barriers were computed using the nudged elastic band (NEB) method [64, 65] in VASP.

The terrace diffusion barrier (E_d) was computed using the NEB method with

Table 3.3: Embedding, hopping and exchange diffusion barriers for Cu, Fe, Mn and W atoms on Cu(1 0 0) computed using VASP. The respective ES barriers are listed inside the parantheses next to the hopping barriers. All energy values are given in eV.

Element	E_d	E_{emb}	E_{hop} (E_{ES})	E_{exc}
Cu	0.550	0.695	0.695 (0.145)	0.510
Fe	0.911	0.427	1.316 (0.405)	0.295
Mn	0.865	0.397	1.334 (0.469)	0.233
W	0.880	0.262	1.845 (0.965)	0.094

three images between the high-symmetry FCC site and the nearest bridge site. Since the diffusion path is symmetric, it is sufficient to sample only half of the diffusion pathway. Similar to Cu, our calculations show that, for all atoms, the bridge site is the saddle point along the diffusion pathway. The E_d values from our calculations are listed in Table 3.3. It is clear that the terrace diffusion barriers computed using the large ($4 \times 6 \times 14$) supercell are very close to the values from ($4 \times 4 \times 14$) supercell.[7] To compute E_{emb} values, we sampled the diffusion pathway using five images. For the three impurity atoms, the final configurations are 0.76 eV (Fe), 0.86 eV (Mn), and 1.7 eV (W) lower in energy than the respective initial configurations. The results of our embedding barrier calculations are listed in Table 3.3. Except for Cu, the E_{emb} values of these elements are less than 1/2 the magnitude of their corresponding E_d values. Since the E_{emb} values for all three impurity atoms are

---

[7] Due to a very high adsorption energy (approximately 8 eV), subtle relaxation effects affect the accurate computation of E_d in the case of W. The value of E_d for a path along $\hat{x}$ is 0.767 eV and for a path along $\hat{y}$ is 0.880 eV. For the path along $\hat{x}$, substrate atoms in contact with the diffusing W adatom are 5 atomic spacings (along $\hat{y}$) apart from their periodicity-replicated "images" compared to 3 atomic spacings (along $\hat{x}$) for the path along $\hat{y}$. Hence, the substrate atoms in contact with the diffusing W atom can shift more in the former case than the latter, resulting in a smaller separation between the W atom and the substrate layer. Since W adsorbs strongly on the substrate, the saddle point is at a lower energy in the former case. Such relaxation effects are known to complicate lattice-gas characterization of adatom interactions on many metallic surfaces. Chapter 2 deals with this issue in detail.

lower than the E_d values for Cu, these atoms could undergo embedding easily at the simulation temperature. As mentioned earlier, due to their stronger bond to Cu, the embedded impurity atoms then act as nucleation centers for the growth of islands. For Cu, even though E_{emb} is higher than E_d, Cu atoms can still undergo embedding at the simulation temperature. Hence the embedding process becomes an important adatom diffusion mechanism on this surface.

To compute the hopping (E_{hop}) and exchange (E_{exc}) barriers, we removed three (four-atom) rows from the sixth layer to create a three atomic rows wide upper terrace (sixth layer) and lower terrace (fifth layer) (cf. Fig. 3.7). For both E_{hop} and E_{exc} calculations, we sampled the pathway using five images. In the case of hopping over a step, the saddle point was found to be on the upper terrace slightly beyond the step edge towards the lower terrace (cf. Fig. 3.7). The E_{hop}, and hence E_{ES}, values are listed in Table 3.3. For Cu, we find E_{ES} to be 0.145 eV, close to the previous theoretical calculations [80, 98] and the value used in our KMC simulations. Compared to Cu, the hopping barriers (E_{hop}) of the responsible impurity atoms, Fe, Mn, and W, are very high. The high values of E_{hop} would prohibit this process in the temperature range at which the experiments were performed. Hence, the presence of these impurities obstructs the smooth layer-by-layer growth observed in the case of pure Cu.

In the case of the exchange process, the final configuration is about 0.98 eV (Fe), 1.1 eV (Mn), and 1.8 eV (W) lower in energy compared to the initial configuration for impurity atoms. The E_{exc} values (cf. Table 3.3) for all four atoms are much smaller than the respective E_{hop} values. Also, the E_{exc} values for all atoms are such that the exchange process can take place easily at the experimental temperature. This shows that the dominant mechanism for adatom diffusion from an upper terrace to a lower terrace is via the exchange process. The E_{exc} values for all three impurity atoms are much smaller than the value for Cu. This is consistent with the reasoning in Ref. [99] that the exchange barrier for adatoms that are strongly bonded to the substrate atoms should be smaller than that for weakly bonded adatoms. In this study, we extend this generalization to other diffusion barriers - *atoms with higher NN binding energies with the substrate atoms (E_{NN}) have higher barriers for terrace diffusion (E_d) and hopping over a step (E_{hop}) but lower barriers for embedding (E_{emb}) and exchange (E_{exc}) processes.* Except for a high E_d value for Fe, this generalization holds true for the values listed in Table 3.3. Due to small barriers for embedding and exchange processes in the case of responsible impurities, Fe, Mn and W, these atoms undergo an embedding or exchange process after deposition. This would explain why such a high concentration of impurity atoms went undetected in the experiments. Both embedding and exchange processes result in the impurity atom being lodged in a position with four NN atoms; this restricts further motion of the impurity atoms. Hence, including these two process in the KMC simulations should not change our results in any significant way. However, it would be interesting to investigate the connection between the exchange process and the alignment of pyramids along the direction of a step.

3.6 Summary

Growth on Cu vicinals has been studied thoroughly by the late H.-J. Ernst and co-workers [7]. However, the instabilities observed in their experiments lacked proper explanation. The failure of the Bales-Zangwill instability mechanism to account for the observed instabilities has resulted in the discovery of several alternate instability mechanisms. None of these instability mechanisms could account for all experimental observations. The instability mechanism based on codeposition of impurities during growth [81] alone could reproduce all the experimental observations. Using KMC simulations and DFT-based VASP calculations, we have narrowed down to Mn, Fe and W the impurity atoms responsible for growth instabilites on Cu. Discussions with members of Ernst's group who performed the experiments indicate W atoms originating from the heater in the experimental apparatus as the possible cause behind the observed instabilities.

In addition to identifying W as the most likely impurity atom responsible for growth instabilities on Cu vicinals, our study has shown that impurity atoms can be categorized into sets based on their E_{NN} and E_d values relative to the corresponding values for the substrate atoms (Cu in our case). Qualitatively similar surface morphologies result when any one of the impurities from the same set is codeposited with Cu during growth. As a result, by computing the E_{NN} and E_d values for atoms of a particular element and categorizing that element into an appropriate set, we can predict the surface morphologies that would result when a small proportion of these atoms is codeposited with Cu atoms. Our results also show that distinct surface morphologies are obtained when two impurities from different sets are codeposited (separately) with Cu. Further, snapshots of the surface in the submonolayer regime show that these differences in surface morphologies originate during early stages of nucleation. We have also characterized the differences in the surface morphologies in the submonolayer regime through GW fits to the distributions of CZ areas. Even though our results pertain to the case of Cu, they can be easily generalized to other surfaces. This study shows a method to achieve nanostructuring of surfaces through the codeposition of suitable impurity atoms during growth.

Chapter 4

Terrace-width Distributions of Touching Steps[1]

4.1 Overview

Physical quantities, such as the kink formation energy (ϵ_k) and the step-step interaction strength ($\tilde{A}$), that are normally used to understand and predict morphological evolution of vicinal surfaces can be estimated from statistical analysis of step fluctuations [2, 3]. With the development of advanced surface imaging techniques, such as scanning tunneling microscopy (STM), low energy electron microscopy (LEEM), reflection electron microscopy (REM), step fluctuations can now be studied thoroughly. The terrace-width distribution (TWD) provides an useful quantity for characterizing both equilibrium and non-equilibrium step fluctuations. It is expressed as the probability distribution, $\hat{P}(\ell)$, of finding neighboring steps at separation ℓ.

At low-temperatures (relative to the roughening temperature of the terrace plane), the predominant thermal excitations on vicinal surfaces are kinks along the step, with kink formation energy (ϵ_k). There are negligibly few adatom or vacancy excitations along the terrace, since their energy is much higher than ϵ_k ($4\epsilon_k$ per atom on a simple cubic lattice routinely used in Monte Carlo simulations). Hence, the terrace-step-kink (TSK) model is well suited for modeling such surfaces. According

---

[1] Adapted from Ref. [8].

to the "Maryland notation", the position of the i-th step edge in this TSK model is $\mathsf{x}_i(\mathsf{y}_n)$, where sans serif denotes discreteness; y_n is defined only at the centers of step-edge atoms, with the index n changing by 1 for unit displacement along $\hat{y}$. The energy contribution from kinks is $\epsilon_k \sum_{i,n} |\mathsf{x}_i(\mathsf{y}_{n+1}) - \mathsf{x}_i(\mathsf{y}_n)|$.

Since overhangs are energetically forbidden, steps cannot cross each other (no-crossing condition). This leads to a decrease in configurational entropy whenever two steps get closer to each other, resulting in an $1/\ell^2$-type entropic repulsion between steps. In addition to this entropic repulsion, there can also be an elastic (or possibly dipolar) repulsion between steps, which decays asymptotically as $1/\ell^2$, the same behavior as the entropic repulsion. The elastic repulsion is approximated by the "instantaneous" form[2] $A \sum_{j>0} |\mathsf{x}_{i+j}(\mathsf{y}_n) - \mathsf{x}_i(\mathsf{y}_n)|^{-2}$. This expression is well defined for non-touching steps ($\mathsf{x}_{i+1}(\mathsf{y}_n) > \mathsf{x}_i(\mathsf{y}_n)$). Combining the contribution from kinks with energetic interactions, the Hamiltonian of a surface with fluctuating steps can be written as[3]

$$H = \sum_{\mathsf{y}_n=1}^{L_y} \left(\sum_{\substack{i,j=1 \\ i>j}}^{N} \frac{A}{|\mathsf{x}_i(\mathsf{y}_n) - \mathsf{x}_j(\mathsf{y}_n)|^2} + \sum_{i=1}^{N} \epsilon_k |\mathsf{x}_i(\mathsf{y}_{n+1}) - \mathsf{x}_i(\mathsf{y}_n)| \right). \tag{4.1}$$

With only $1/\ell^2$ repulsions, there is just one characteristic length, the mean step separation $\langle \ell \rangle$, in the $\hat{x}$ direction, and so the TWD essentially depends only on the dimensionless length $s = \ell/\langle \ell \rangle$:

$$P(s = \ell/\langle \ell \rangle) = \langle \ell \rangle \hat{P}(\ell). \tag{4.2}$$

---

[2] The repulsion acts only between step edge atoms with the same y_n values. Hence, the interaction is termed instantaneous due to the time-like nature of y.

[3] To include screw periodic boundary condition, the first term is changed to $A|\mathsf{x}_j(\mathsf{y}_n) + N\langle \ell \rangle - \mathsf{x}_j(\mathsf{y}_n)|^{-2}$ for $i > j + (N/2)$.

Along with the no-crossing condition, it is normally assumed that steps do not touch each other except at corners (e.g., $\mathsf{x}_{i+1}(\mathsf{y}_n) = \mathsf{x}_i(\mathsf{y}_{n+1})$), i.e., all the steps are taken to be of monatomic height. This is a reasonable assumption because formation of double-, and hence multi-layer high step costs energy.

For analytic modeling it is more convenient to use the step-continuum approximation [2], which allows $x_i(y)$ to vary continuously with y. Since $x_i(y)$ is single valued, the configuration of steps in two spatial dimensions (2D) can be viewed as the worldlines of particles evolving in 1D: y becomes time-like. The non-touching condition underlies their characterization as spinless fermions (or hard bosons) in 1D, and the stiffness $\tilde{\beta}$, which can be related to ϵ_k, is their "mass". In this framework, the instantaneous interstep repulsion strength A enters only as a dimensionless combination

$$\tilde{A} = A\tilde{\beta}\beta^2 \tag{4.3}$$

where β is $1/(k_BT)$. Since $\tilde{A}$ determines the morphology of and communication between steps, gauging it is crucial to understanding step behavior. One of the straightforward ways of measuring $\tilde{A}$ is through the measurement of TWDs. An excellent review of the various approximation schemes used to extract $\tilde{A}$ from TWDs can be found in Ref. [9]. The non-touching condition together with screw-periodic boundary conditions along $\hat{x}$ direction make the step edges analogous to the spinless fermions along a chain [or on a 1D ring] of the Calogero-Sutherland models [21]. The key parameter in these models ϱ is related to $\tilde{A}$ through[4]

---

[4] We use ϱ rather than the conventional β to avoid confusion with stiffness or inverse temper-

$$\varrho = 1 + \sqrt{1 + 4\tilde{A}}; \quad \tilde{A} = \frac{\varrho}{2}\left(\frac{\varrho}{2} - 1\right). \tag{4.4}$$

For ϱ =1,2,4, the ground-state probability density, which corresponds to $P(s)$, reduces to the distribution of eigenvalues for random matrices with orthogonal, unitary and symplectic symmetry, respectively [91]. Accordingly, they are excellently approximated by the Wigner surmise [92]:

$$P_\varrho(s) = a_\varrho s^\varrho \mathrm{e}^{-b_\varrho s^2} \tag{4.5}$$

where the constants b_ϱ and a_ϱ are fixed by the conditions of unit-mean and normalization

$$b_\varrho = \left[\frac{\Gamma(\frac{\varrho+2}{2})}{\Gamma(\frac{\varrho+1}{2})}\right]^2, \quad a_\varrho = \frac{2b_\varrho^{(\varrho+1)/2}}{\Gamma(\frac{\varrho+1}{2})}. \tag{4.6}$$

For stepped surfaces there is no reason for $\tilde{A}$ to have the special values 0 or 2 ($\varrho = 2$ or 4), and -1/4 ($\varrho = 1$) is unphysical. Thus, we have taken Eq. (4.5) to apply for arbitrary $\varrho \geq 2$ or $\tilde{A} \geq 0$ and call it the generalized Wigner distribution (GWD). The GWD gives a better description of TWDs measured from both experiments and numerical simulations than any of the preexisting models [9, 100]. Though there is no formal justification based on random matrix theory for generalizing the Wigner surmise for arbitrary values of ϱ, Eq. (4.5) was shown to be the steady-state solution of the Fokker-Planck equation derived for the case of 1D Coulomb gas [101]. In addition to putting the GWD on a firm theoretical footing, the Fokker-Planck

---

ature.

formalism also gives valuable information about the relaxation of TWDs from an initially strained configuration towards equilibrium. Recently, the time constant of relaxation (τ) was found to be related to the atomistic processes that underlie step fluctuations [102]. All of these findings emphasize the importance of the GWD in studying properties of step fluctuations.

Adding the more restrictive non-touching condition to the veridical non-crossing condition makes the fermion analogy possible, enabling the analytic treatment of TWDs. The fermion analogy would also preclude steps from coinciding, to form multilayer steps. However, double- or multi-layer high steps could occur physically during step fluctuations. This issue has largely been ignored or glossed over. In this chapter, we show how the loosening of this non-touching condition alters the form of the terrace-width distribution (TWD) and, thence, the apparent strength of the step-step repulsion ($\tilde{A}$) deduced from it. Such touching steps are more likely to be found on surfaces with one or more of the following properties - (i) low step stiffness, (ii) closely spaced steps (small separation ℓ) and (iii) steps with little or no energetic interaction between them. In the case of ABAB stacking, steps separated by half lattice spacing ($a/2$), the smallest possible separation between adjacent steps, also constitute instances of step touching [103].

If we allow touching steps, two or more step edges can be at the same position ($\mathsf{x_i(y_n) \leq x_{i+1}(y_n)}$), the analogy with 1D fermions is not strictly valid. This issue is much more significant for discrete models. Since touching is a contact interaction, its effect on TWDs should be insignificant for larger step separations (higher values of s), and TWDs of touching steps should converge to the GWD for large s. In the opposite small-s limit, where ϱ (and hence $\tilde{A}$) is sensitive to the TWD, touching effects should be significant, impacting measurements of step-step interaction strength. Such a situation gives rise to the following questions: How do touching steps alter the TWD? How should one measure the step-step interaction on a surface with touching steps? Using Monte Carlo simulations, we have studied the TWDs of touching steps. The specifics of our simulation are given in section 4.2 and our results are presented in section 4.3. In section 4.4, we show how to incorporate the effects of touching in step-step interaction strength ($\tilde{A}$) measurements. In section 4.5, we discuss the mapping of touching steps to non-touching steps under specific conditions. Section 4.6 deals with the possibility of multi-step bunching and faceting transitions in the case of AT steps.

4.2 Monte Carlo simulations of touching steps

Since we are interested in equilibrium TWDs (rather than step dynamics) of touching steps, we used the Metropolis method in our Monte Carlo simulations. We modeled the vicinal surface using the TSK model with steps along the $\langle 1\ 0\ 0\rangle$ direction (straight steps). The underlying lattice was taken to be simple cubic. Steps were allowed to fluctuate via the attachment-detachment process. Step edge diffusion was suppressed in our simulations. To focus clearly on the problem of concern, we considered only the case of "free-fermions": $A = \tilde{A} = 0 \Rightarrow \varrho = 2$. This eliminated divergences of the elastic repulsion term when the steps touched and also avoided the issue of whether all steps or just neighboring steps experienced this repulsion. There are two energy parameters in this model - (i) the kink formation energy (ϵ_k) and (ii) the energy (ϵ_t) of two adjacent steps touching to form a double-height unit segment. For the sake of simplicity, we assumed a linear relationship between the height of the step and the formation energy of a double-height step, i.e., the energy required to form a p-layer high step is $(p-1)\epsilon_t$. We set the temperature of the simulations such that $\beta\epsilon_k = 2$, as in our group's previous simulation studies [100, 101]. We simulated the TWDs for values of ϵ_t ranging from $\beta\epsilon_t = \infty$ (non-touching case) down to $\beta\epsilon_t < 0$.[5] In the rest of this chapter, we refer to steps with an energy cost for doubling ($\beta\epsilon_t \geq 0$) as RT (repulsively touching) steps, and steps for which doubling is energetically favored ($\beta\epsilon_t < 0$) as AT (attractively touching) steps. The rationale behind such a categorization is discussed later in this section.

We simulated the TWDs of touching steps on surfaces with $\langle \ell \rangle$ = 6, 8, 10, 12 and 16. We fixed the length of the steps (L_y) to be $L_y = 500$ for terraces with $\langle \ell \rangle$ = 6, 8, 10 and $L_y = 600$ for terraces with $\langle \ell \rangle$ = 12 and 16. These L_y values were found to be sufficient to eliminate the finite-size effect due to short step lengths in the resulting TWDs. On surfaces with touching steps, once a N-layer high step (N = total number of steps on the surface) forms at a certain lattice point, the no-crossing condition forbids further step fluctuations at that lattice point. As a result, all the steps get pinned at that point, leading to a zippering transition in which all steps on the surface eventually form a N-atom high bunch. To avoid this unpleasant scenario, we used N = 40 for terraces with $\langle \ell \rangle$ = 6, 8, 10, 12 and N = 28 for the $\langle \ell \rangle$ = 16 terrace. Even though using higher value of N does not preclude

---

[5] Alternately, we could fix the value of $\beta\epsilon_t$ and simulate the TWDs for different values of ϵ_t/ϵ_k.

the bunching transition, it drastically reduces the probability of the occurrence of such a transition.

To investigate the effect of step stiffness $\tilde{\beta}$ on TWDs of touching steps, we also simulated the TWDs of surfaces with steps along the $\langle 1\ 1\ 0 \rangle$ direction (fully kinked steps). Further motivation comes from the fact that the applicability of the generalized Wigner formalism for this case has not been reported. Since fully kinked steps have smaller $\tilde{\beta}$ than straight steps [4], we consider the simplest case in which $\langle 1\ 1\ 0 \rangle$ steps fluctuate freely (without energy cost). However, attachment and detachment processes were allowed to take place only at kink sites to maintain an equal number of kinks and anti-kinks. We restricted ourselves to the freely touching ($\epsilon_t = 0$) case. To measure step separations between fully kinked steps, we followed the mapping method proposed by Abraham et al. [104]. In all of our simulations, we started with an initial surface configuration of equally spaced steps. We let the steps fluctuate until the variance of the TWD reached a steady value before measuring the TWDs. The results of our simulations are presented in the following section.

4.3 The modified generalized Wigner distribution and effective attraction

From our Monte Carlo simulations, we find that allowing step touching alters the resulting TWDs ($P(s)$) from that of non-touching steps ($P_2(s)$) in two major ways: (i) $P(0) > 0$ and (ii) $P(s)$ is broader than $P_2(s)$ [8]. For terraces with the same step touching energy (ϵ_t), the deviation is greater for surfaces with smaller $\langle \ell \rangle$

values (cf. Fig. 4.1(a)) and for surfaces with the same $\langle \ell \rangle$, the deviation is greater for surfaces with smaller ϵ_t values (cf. Fig. 4.1(b)) [8]. The deviation from $P_2(s)$ can also be quantified as follows: $P_2(s)$ divides the TWDs of touching steps into three regions as marked in Fig. 4.1(a). In regions I ($0 \leq s \lesssim 0.5$) and III ($s \gtrsim 1.5$), TWDs of touching steps have higher values compared to $P_2(s)$, while in region II, they have lower values. Despite the deviation, the TWDs of both touching and non-touching steps rise as power-laws for small s and decay as Gaussian for large s. For the TWD of touching steps, we make the ansatz

$$P_{\gamma,\varrho} = P^t(s) + a_{\gamma,\varrho} s^{\varrho} e^{-b_{\gamma,\varrho} s^2}; \quad P^t(s) \equiv P(0) e^{-\gamma s} \tag{4.7}$$

where $P^t(s)$ describes the distribution for small values of s, capturing the effect of touching. The second term is the generalized Wigner distribution modified to accommodate the first term; γ and ϱ are the fit-parameters and $P(0)$ is the value of the distribution at $s = 0$ measured experimentally or through simulations. The quantity $\langle \ell \rangle^{-1} P(0)$ (cf. Eq. (4.2)) gives the ratio of double- or multiple-atomic height step edge lengths to the total length of step edges on the surface. From the normalization and unit-mean constraints of $P_{\gamma,\varrho}(s)$, we get

$$\frac{b_{\gamma,\varrho}}{b_{\varrho}} = \frac{1}{\lambda^2}, \; \lambda \equiv \frac{1 - \frac{P(0)}{\gamma^2}}{1 - \frac{P(0)}{\gamma}} \tag{4.8a}$$

and

$$\frac{a_{\gamma,\varrho}}{a_{\varrho}} = \frac{\Theta}{\lambda^{\varrho}}, \; \Theta \equiv \frac{1 - \frac{P(0)}{\gamma}}{\lambda}. \tag{4.8b}$$

Substituting the values of $a_{\gamma,\varrho}$ and $b_{\gamma,\varrho}$ in Eq. (4.7) and rearranging the terms, the

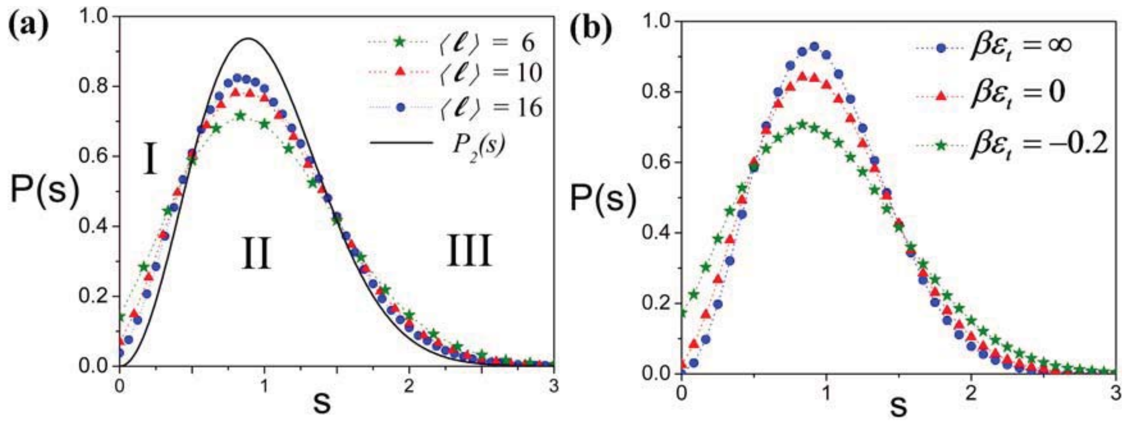

Figure 4.1: TWDs of touching steps computed (a) for different $\langle \ell \rangle$ values with $\beta\epsilon_t = -0.1$. The solid curve is $P_2(s)$, the GWD for non-touching steps with no energetic interactions. (b) for different $\beta\epsilon_t$ values with $\langle \ell \rangle$ =12.

TWDs of touching steps can be written conveniently in terms of $P_\varrho(s)$ (cf. Eq. (4.5)) as

$$P_{\gamma,\varrho}(s) = P(0)e^{-\gamma s} + \Theta P_\varrho(s/\lambda). \tag{4.9}$$

The argument s/λ of P_ϱ can be reduced to s if we work in terms of an effective mean step spacing $\langle \ell \rangle_{\text{eff}} = \lambda \langle \ell \rangle$. The distribution, $P_{\gamma,\varrho}(s)$, gives an excellent fit to the TWDs of touching steps from our simulations (see Fig. 4.2). We refer to $P_{\gamma,\varrho}(s)$ as the modified generalized Wigner distribution (MGWD). Broadly speaking, the values of $P(0)$ and γ determine $P_{\gamma,\varrho}(s)$ in region I, Θ determines its peak height in region II, and λ determines the decay rate of $P_{\gamma,\varrho}(s)$ in region III. For fixed values of ϱ and γ, higher (lower) values of $P(0)$ and λ combined with a lower (higher) value of Θ implies a broader (narrower) distribution.

The values of $P(0)$ for straight steps obtained from our simulations are listed in Table 4.1. The proportion of double- or multiple-atomic height step segments,

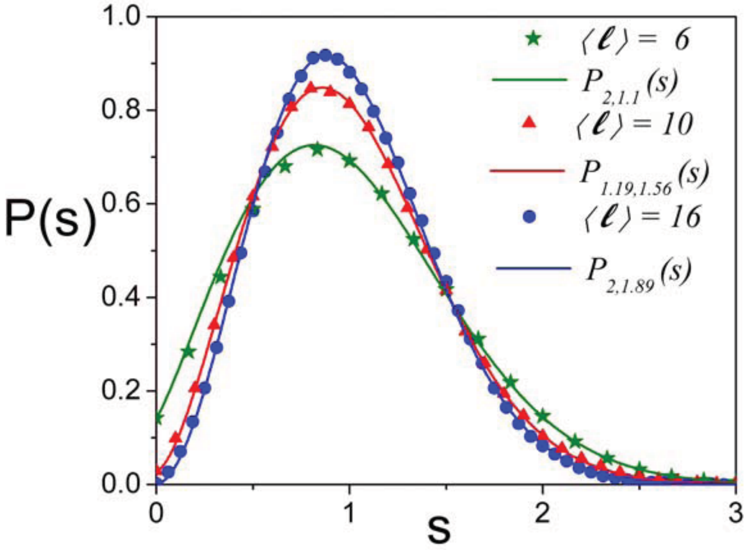

Figure 4.2: MGWD fits (solid curves) to the TWDs (symbols) of both straight and fully kinked touching steps. The $\beta\epsilon_t$ values for $\langle\ell\rangle = 6$ is -0.1, $\langle\ell\rangle = 10$ (fully kinked steps) is 0 and $\langle\ell\rangle = 16$ is 0.5.

$P(0)$, is higher for surfaces with smaller $\langle\ell\rangle$ and lower ϵ_t (cf. Figs. 4.1(a) and 4.1(b)), as expected: with smaller $\langle\ell\rangle$, step segments are more likely to meet during fluctuations, and the lower ϵ_t, the more likely such steps stay touched. To determine the values of γ and ϱ, we used the non-linear fitting function in MATHEMATICA®. All data points were weighed equally in obtaining the fits. The values of γ and ϱ obtained from our fits are listed in Table 4.1. For straight steps, the parameter γ is invariably 2 regardless of $\langle\ell\rangle$ and ϵ_t, until negative ϵ_t heralds the instability of the steps to collapse. Especially for RT steps, the very small values of $P(0)$ values lead to insensitivity to γ in the quality of the fit. Due to its weak dependence on $\langle\ell\rangle$ and ϵ_t, no physically relevant information can be extracted from the value of γ.

However, an interesting trend emerges from ϱ values. From Table 4.1, we see that $\varrho < 2$ whenever touching is allowed ($\beta\epsilon_t < \infty$) [8].[6] This implies an effective at-

---

[6] $\varrho \lesssim 2$ even for $\beta\epsilon_t = \infty$ (non-touching) and $\langle\ell\rangle$=6,8,10,12, mainly due to finite-size effect due to small $\langle\ell\rangle$ and ϱ does become 2 for $\langle\ell\rangle$=16.

Table 4.1: Values of $P(0)/\gamma/\varrho$ obtained from our simulations for different values of $\langle \ell \rangle$ and $\beta\epsilon_t$ in the case of straight $\langle 1\ 0\ 0 \rangle$ steps.

$\langle \ell \rangle$	$\beta\epsilon_t = \infty$	0.5	0	-0.05	-0.1	-0.2
6	0.000/n.a./1.80	0.012/2/1.62	0.076/2/1.3	0.102/2/1.2	0.142/2/1.1	0.321/4/0.8
8	0.000/n.a./1.87	0.008/2/1.70	0.049/2/1.41	0.068/2/1.4	0.098/2/1.3	0.253/3/0.9
10	0.000/n.a./1.90	0.005/2/1.75	0.035/2/1.48	0.041/2/1.42	0.070/2/1.34	0.213/3/1.0
12	0.000/n.a./1.96	0.003/2/1.82	0.026/2/1.55	0.040/2/1.39	0.055/2/1.44	0.173/2/1.1
16	0.000/n.a./2.00	0.002/2/1.89	0.015/2/1.67	0.023/2/1.57	0.038/2/1.46	0.129/2/1.13

traction between steps ($\tilde{A}_{\text{eff}} < 0$, cf. Eq. (4.4)). We term this an effective interaction because no such attraction actually exists between steps; $\tilde{A} = 0$ in our simulations. This attraction is greater for surfaces with smaller $\langle \ell \rangle$ and smaller ϵ_t. The fact that touching leads to an attraction between steps has also been observed in a recent analytic study [103]. These two studies show that touching could impact step-step interaction strength measurements significantly.

The TWDs of fully kinked steps are very similar to those for straight steps with $\epsilon_t = 0$. Hence, the MGWD gives a very good fit even in the case of fully kinked steps (see Fig. 4.2). The fitted values of $P(0)$, γ and ϱ are listed in Table 4.2. The values of $P(0)$ in the case of fully kinked steps are very close but slightly lower than the corresponding values for straight steps. Unlike straight steps, the parameter γ varies with $\langle \ell \rangle$ for fully kinked steps. However, the variation is neither uniform nor huge to detect any dependence on $\langle \ell \rangle$. All values of ϱ are less than 2 signalling the presence of effective attraction between steps even in the case of kinked steps. The ϱ values for fully kinked steps are only slightly higher than those for straight steps, while the values of $P(0)$ and γ are slightly lower. Hence, step stiffness has at most

Table 4.2: Values of $P(0)/\gamma/\varrho$ obtained from our simulations for different values of $\langle \ell \rangle$ in the case of fully kinked $\langle 1\ 1\ 0 \rangle$ (zigzag) steps with $\beta\epsilon_t = 0$.

$\langle \ell \rangle$	$\beta\epsilon_t = 0$
6	0.058/2/1.41
8	0.036/1.5/1.50
10	0.029/1.19/1.56
12	0.017/1.7/1.641
16	0.011/1.2/1.645

a weak effect on the TWDs of touching steps [8].

The following relations are consistent with the $P(0)$ and γ values listed in Tables 4.1 and 4.2:

$$\gamma > 1 \quad \& \quad P(0) < 1 \quad \Rightarrow \quad \lambda > 1 \quad \& \quad \Theta < 1. \tag{4.10}$$

Since $\lambda > 1, \langle \ell \rangle_{\text{eff}} = \lambda \langle \ell \rangle > \langle \ell \rangle$: steps now see an effective mean spacing greater than the actual value. This is because the formation of multi-layer steps reduce the step density on the remaining vicinal surface. Since $\Theta < 1$, the peak of the TWDs of touching steps is smaller than that of $P_2(s)$. For a fixed value of γ, using Eqs. (4.8a) and (4.8b), we can show the following:

$$\frac{\partial \lambda}{\partial P(0)} > 0 \quad \& \quad \frac{\partial \Theta}{\partial P(0)} < 0. \tag{4.11}$$

From Eq. (4.11), we see that λ increases and Θ decreases with $P(0)$. Hence, a higher value of $P(0)$ implies a broader distribution. Results from our Monte Carlo simulations show that allowing step touching broadens the TWD. The MGWD gives an excellent fit to the TWDs of both straight and fully kinked touching steps, showing that the fermion picture is still relevant for touching steps. However, in the fermion picture, step touching leads to an effective attraction between steps. In the following section, we show how this effective attraction can be incorporated into the fermion picture.

4.4 Finite-size scaling in step-step interaction strength ($\tilde{A}$) measurements

Our Monte Carlo simulations have shown that allowing step touching broadens the TWD and gives rise to an effective attraction between steps. As discussed earlier, steps that are far apart ($\langle \ell \rangle \gg 1$) hardly come into contact with neighboring steps and steps that have higher step doubling energy ($\beta\epsilon_t \gg 0$) are less likely to form double-layer high steps even when they meet neighboring steps, both cases resulting in fewer instances of step touching. Thus, the strength of effective attraction should decrease (i.e. $\varrho \to 2$) with increasing $\langle \ell \rangle$ or $\beta\epsilon_t$. This trend is also reflected in the ϱ values listed in Tables 4.1 and 4.2. Since the strength of this effective attraction vanishes for high $\beta\epsilon_t$ and high $\langle \ell \rangle \gg 1$ values, this effective attraction can be modeled as a finite-size effect. We can relate the measured ϱ value and the corresponding value when step touching is absent, ϱ_∞, through a finite-size scaling function:

$$\varrho_\infty = \varrho + f(\langle \ell \rangle, \beta\epsilon_t). \tag{4.12}$$

To account for our simulation results, the finite-size scaling function, $f(\langle \ell \rangle, \beta\epsilon_t)$, should satisfy the condition

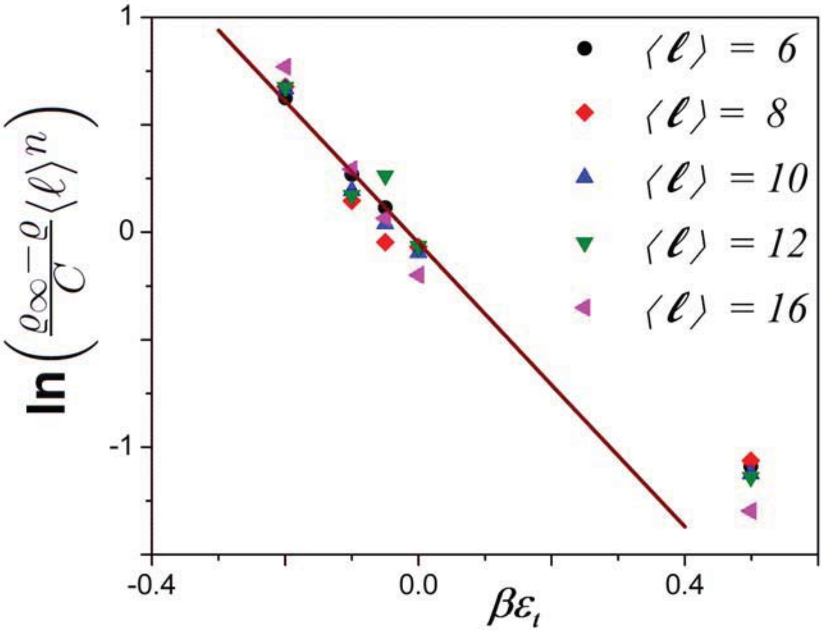

Figure 4.3: Collapse of our simulation data (slope of the line is $-m = -3.3$) onto the finite-size relation given in Eqs. (4.12) and (4.14).

$$f(\langle\ell\rangle,\beta\epsilon_t)\xrightarrow[\langle\ell\rangle\to\infty\ \text{or}\ \beta\epsilon_t\to\infty]{}0. \tag{4.13}$$

We tried a combination of power-law and exponential decays of $\langle\ell\rangle$ and $\beta\epsilon_t$ for $f(\langle\ell\rangle,\beta\epsilon_t)$. Among those functions, we find that the following functional form of $f(\langle\ell\rangle,\beta\epsilon_t)$

$$f(\langle\ell\rangle,\beta\epsilon_t) = C\langle\ell\rangle^{-n}e^{-m\beta\epsilon_t} \tag{4.14}$$

accounts well for the simulation data.[7,8] The values of the parameters in the finite-size scaling function, C, m, and n, were determined using the non-linear fitting function (with all data points weighed equally) in MATHEMATICA®. From our

---

[7] The functional form with exponential decays of both $\langle\ell\rangle$ and $\beta\epsilon_t$ ($Ce^{-n\langle\ell\rangle}e^{-m\beta\epsilon_t}$) gives a marginally worse fit to our data. Functions that have power-law decay with $\beta\epsilon_t$ run into problems for the freely touching case ($\beta\epsilon_t$=0).

[8] Since $\beta\epsilon_k$=2, the finite-size scaling function can also be written as $C\langle\ell\rangle^{-n}e^{-2m\epsilon_t/\epsilon_k}$.

fits, we find $C = 0.9 \pm 0.1$, $m = 3.3 \pm 0.2$, and $n = 0.29 \pm 0.07$. The data from our simulations nicely collapse onto the functional form given in Eq. (4.14) with these values (see Fig. 4.3) [8].

In addition to touching, there are other effects that become important at relatively small step separations. Since the step-continuum approximation underlies the generalized Wigner formalism, differences between between Eq. (4.5) and its discrete analogue are important on surfaces with small $\langle \ell \rangle$. Richards et al. [105] emphasized that such differences become nonnegligible for $\langle \ell \rangle \lesssim 4$. Higher-order corrections ($\mathcal{O}(\ell^{-3})$, $\mathcal{O}(\ell^{-4})$) to the repulsive interaction are known to play a role at small step separations [106]. If present, such repulsive interactions would prohibit neighboring steps from coming closer than a few lattice spacings. We simulated the TWDs of steps that cannot come closer than two lattice spacings; we call them nearest-neighbor excluding (NNE) steps. The TWDs of NNE steps and comparisons with TWDs of touching and non-touching steps are presented in Appendix B.

Our results clearly show that touching affects $\tilde{A}$ measurements. Further, the effects of step touching can be incorporated into the generalized Wigner formalism through a finite-size scaling function. Our results show that the finite-size scaling, $f(\langle \ell \rangle, \beta\epsilon_t)$, decays with $\langle \ell \rangle$ with a power-law exponent close to 1/3. Due to the dependence of $f(\langle \ell \rangle, \beta\epsilon_t)$ on $\langle \ell \rangle$, comparison of $\tilde{A}$ measurements of the same material for several $\langle \ell \rangle$ values would provide a clue to the presence of touching effects. Thus to eliminate such touching effects in $\tilde{A}$ measurements, experiments should involve several misorientations, at least some of which should be shallow ($\langle \ell \rangle \gg 1$).

4.5 Mapping touching steps to non-touching steps

For the special case $\epsilon_t = 0$, a surface with touching steps can be mapped to a surface with non-touching steps through addition of a single row of atoms along the step edge direction to all terraces. This procedure is also used by Kim et al. [103] to map nearest neighbor overlap steps to 1D ring of "spinless" fermions and is based on the procedure developed in Ref. [107]. In this mapping, a surface of touching steps with mean step spacing $\langle \ell \rangle$ is equivalent to a surface of non-touching steps with mean step spacing $\langle \ell \rangle + 1$, which leads to the following linear relation between the normalized step spacing of touching (s_T) and non-touching steps (s_{NT})

$$s_{NT} = \frac{\langle \ell \rangle}{\langle \ell \rangle + 1} \left(s_T + \frac{1}{\langle \ell \rangle} \right) \tag{4.15}$$

where $\langle \ell \rangle$ is the mean step spacing for touching steps. Since $P_2(s)$ describes the TWD of non-touching steps, replacing s_{NT} with the expression on right side of Eq. (4.15) gives a fitting function for the TWDs of touching steps. In this mapping, the TWD of touching steps ($P_T^m(s)$, where m denotes mapping) then becomes

$$P_T^m(s) = \left(\frac{\langle \ell \rangle}{\langle \ell \rangle + 1} \right) P_2 \left(\frac{\langle \ell \rangle}{\langle \ell \rangle + 1} \left(s + \frac{1}{\langle \ell \rangle} \right) \right) \tag{4.16}$$

where the prefactor $\langle \ell \rangle / (\langle \ell \rangle + 1)$ comes from Eq. (4.2). Further corrections to the distribution are required to satisfy the unit-mean and normalization conditions. The distribution $P_T^m(s)$ gives an excellent fit to the TWDs of both straight and fully-kinked (zigzag) steps (cf. Fig. 4.4). The fit is even better for the TWDs of fully-kinked steps.

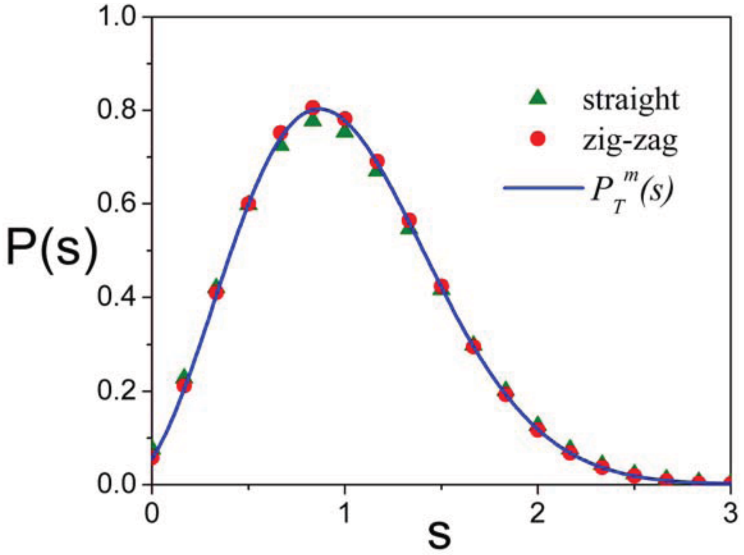

Figure 4.4: $P_T^m(s)$ fit (solid blue curve) to the TWDs of straight steps (triangles) and zigzag steps (discs) with $\langle \ell \rangle = 6$ and $\beta\epsilon_t = 0$.

From Eq. (4.16), the quantity $P(0)$ in the case of touching steps can then be computed using

$$P_T^m(s=0) = \left(\frac{\langle \ell \rangle}{\langle \ell \rangle + 1}\right) P_2 \left(\frac{1}{\langle \ell \rangle + 1}\right). \tag{4.17}$$

The values of $P(0)$ computed using Eq. (4.17) are in very good agreement with the

Table 4.3: Comparison of $P(0)$ values obtained through the mapping method (Mapping) and corresponding values from our simulations when $\beta\epsilon_t = 0$ for both straight (⟨1 0 0⟩ Sim.) and fully kinked (⟨1 1 0⟩ Sim.) steps.

$\langle \ell \rangle$	Mapping	⟨1 0 0⟩ Sim.	⟨1 1 0⟩ Sim.
6	0.055	0.076	0.058
8	0.035	0.049	0.036
10	0.024	0.035	0.029
12	0.018	0.026	0.017
16	0.011	0.015	0.011

values obtained from our simulations for both straight ⟨1 0 0⟩ and fully-kinked ⟨1 1 0⟩ steps. The agreement is especially striking in the case of fully-kinked ⟨1 1 0⟩ (zigzag) steps.

The simple mapping between touching and non-touching steps presented in this section gives a direct method to finding fits for touching steps. However, this method is applicable only for $\beta\epsilon_t = 0$ case and even for $\beta\epsilon_t = 0$, measurement of ϱ in this procedure is not trivial as shown in Ref. [103]. Hence, our Monte Carlo simulations combined with the finite-size scaling function provide a straightforward way to quantify touching effects on TWDs.

4.6 Step bunching transition

Earlier in the chapter, we made a distinction between RT steps ($\beta\epsilon_t > 0$) and AT steps ($\beta\epsilon_t < 0$). Since the formation of multi-layer high steps is energetically favorable in AT steps, collapse (bunching [108, 109]) should occur once $\beta\epsilon_t$ goes below a particular value. Previous theoretical studies [108, 109, 110, 111] have shown

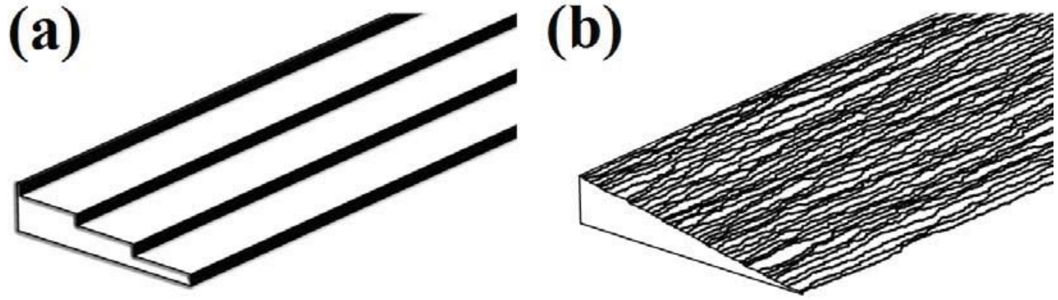

Figure 4.5: Evolution of a surface with $\beta\epsilon_t = -1/20$ from an initially bunched configuration towards equilibrium: (a) initial configuration of 4 step bunches, each with 10 steps, (b) equilibrium configuration in which the steps have separated from the bunches.

that surfaces with negative step touching energies ($\beta\epsilon_t < 0$) without the presence of a long-range repulsion are unstable and inevitably collapse. Therefore, RT steps are considered physically dissimilar to AT steps and hence, such a classification was introduced in our study. However, in our simulations, we do not find any striking dissimilarities between TWDs of steps with $\beta\epsilon_t = 0^+$ and TWDs of steps with $\beta\epsilon_t = 0^-$. We do not see multistep bunching for ϵ_t modestly negative ($\beta\epsilon_t \gtrsim -0.25$) [8] and the MGWD gives an excellent fit to the data down to $\beta\epsilon_t = -0.2$ (cf. Fig. 4.2). The threshold $\beta\epsilon_t$ value depends weakly on $\langle \ell \rangle$. This behavior is reminiscent of the extensively studied problems of step pinning/[de]wetting [110, 112, 113] and doubling [114].

To check whether the time and length scales in our simulations are too small to see such bunching, we also simulated the evolution of AT steps with longer step edges (up to $L_y = 10,000$ - over an order of magnitude larger than the L_y used for earlier calculations). Since longer step edges take more time to attain equilibrium, the number of Monte Carlo steps per site was increased by about a factor of ten. Instead of our usual procedure of starting with equally spaced steps, we chose an initial configuration of 4 step bunches, each with 10 steps, and allowed the steps to evolve. Our results show no indication of such collapse for modestly negative $\beta\epsilon_t$ values. We see no evidence for further coalescence; rather the steps separate from the bunches (see Fig. 4.5). Also, the variance of the TWD for the initially bunched configuration converges to the equilibrium variance of the TWD for equally spaced steps at equilibrium (cf. Fig. 4.6). This behavior is qualitatively different from the unstable, sensitive behavior for $\beta\epsilon_t \lesssim -0.3$ when steps do not separate from their

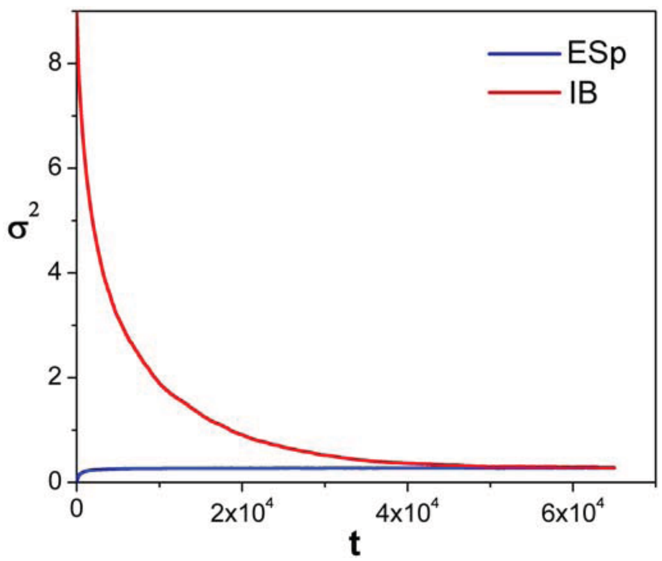

Figure 4.6: Evolution of the variance of the TWD (σ^2) as a function of Monte Carlo time (t) for a (a) surface with an initial configuration of equally spaced (ESp) steps (blue/lower curve), (b) surface with an initial configuration of 4 step bunches (IB), each with 10 steps (red/upper curve).

initial bunches. In our simulations, bunching occurs at $\beta\epsilon_t \sim -0.3$ rather than at $\beta\epsilon_t = 0$, presumably due to the finite density of steps in the system. The entropic energy of the steps stabilizes the surface for moderately negative values of $\beta\epsilon_t$.

4.7 Summary

The step-step interaction strength ($\tilde{A}$) is an important parameter in modeling morphological evolution on vicinal surfaces. The 1D spinless fermion picture provides an useful framework for connecting $\tilde{A}$ and the equilibrium TWDs of steps. The no-crossing condition is a fundamental and genuine assumption but it is the more restrictive non-touching condition that connects step fluctuations to the fermion picture. The fermion picture has been very useful in elucidating both equilirbium and dynamic properties of step fluctuations on vicinal surfaces. However, there is no physical reason that would prohibit steps from coinciding to form double-layer or even multi-layer high steps. This observation has been neglected in all prior treatments of the subject. As a result, the applicability of the fermion picture in the absence of the non-touching condition has not been reported to the best of our knowledge.

Results from our Monte Carlo simulations show that step touching leads to a broadening of the TWDs. The MGWD gives an excellent fit to the TWDs of touching steps, showing that the fermion picture is relevant even for the case of touching steps. However, a straightforward application of the fermion picture leads to an effective attraction between steps. Our results listed in Tables 4.1 and 4.2 show that step touching, through this effective attraction, could affect the interaction strength measurements significantly. This issue is very important for experiments on surfaces with small mean step separation (fewer than about a dozen lattice spacings), as is the case with almost all STM experiments. At the same time, this issue is less relevant for LEEM and REM experiments that normally deal with surfaces with higher $\langle \ell \rangle$ values.

Since the effects of step touching vanish for large $\langle \ell \rangle \gg 1$ values and high $\beta\epsilon_t$ values, they can be incorporated into the fermion picture as a finite-size effect. Our finite-size scaling function given in Eq. (4.14) provides a very good description of our simulation data. In addition to step touching, there are other effects that become significant at small step separations. In the light of such results, a careful consideration of step behavior at small separations is important for an accurate interpretation of data from both simulations and experiments. Thus, experiments seeking to extract $\tilde{A}$ of a particular material should employ several vicinals, some of them with large $\langle \ell \rangle$ values. We look forward to experiments that can verify the form of our finite-size scaling function.

Chapter 5

Summary and future work

5.1 Summary

Due to their applications in a wide range of fields, the study of vicinal surfaces is technologically important. A thorough understanding of the surface morphologies and the factors that affect them is necessary for using vicinal surfaces in manufacturing devices and components at the nanometer scale. Due to the vastly different length scales involved, multi-scale approaches are well suited for studying vicinal surfaces. One such approach, the continuum step model provides a useful way to account for both atomistic processes and large scale morphological evolution. In this model, morphological evolution is described in terms of motion of steps which is implicitly connected to atomic motion at step edges and terraces. The continuum step model relies on the assumption that morphological evolution of vicinal surfaces can be characterized using minimal models with a few key, experimentally measurable parameters. With a tremendous increase in the computational power combined with the development of sophisticated computational packages, these key parameters can now be computed with good accuracy. In this thesis, using a combination of Monte Carlo methods and DFT-based VASP calculations, we have computed various physical parameters that are important for modeling steps on vicinal surfaces. Our results are in excellent agreement with experimental observations. In addition to explaining experimental measurements of step properties, we also offer certain predictions that require validation from experiments.

Lattice-gas models are useful tools for categorizing structural properties, energetics and evolution of adatoms and steps on surfaces, allowing efficient statistical-mechanical calculations. Even though pair interactions are usually sufficient to account for a wide range of overlayer phenomena, non-pairwise multi-site interactions are essential to account for experimental observations concerning properties related to steps. On Pt and Cu, our results show that multi-site interactions with significant contributions from direct interactions are sensitive to adatom relaxations. Using DFT-based VASP calculations, we have shown that adatom relaxations affect the computation of multi-site interaction strengths (trios and quartos) on homoepitaxial Pt(1 1 1), Cu(1 0 0) and Cu(1 1 0) systems.

Computing the difference in formation energies of A- and B-steps (ΔE_{AB}) on fcc (1 1 1) surfaces using orientation dependent trios requires the usage of fewer adatoms and smaller supercells than normally used to compute ΔE_{AB} values. This leads to a significant reduction in computational cost associated with such calculations. The trio-based approach has also had some success in reproducing the experimentally observed E_A/E_B value on Cu(1 1 1). However, on Pt(1 1 1), our VASP calculations show that the strengths of the orientation dependent trios, and hence ΔE_{AB} values, are extremely sensitive to lateral relaxation of adatoms. For all adatom configurations, including the Feibelman configuration, the ΔE_{AB} values are negative for no- and z-relaxation schemes in contradiction with experimental observations. This shows that greater energy reduction due to lateral relaxation of adatoms happens at B-step edges compared to A-step edges. The range of ΔE_{AB} values obtained from different adatom configurations show that local positions of adatoms in turn affect lattice-gas interactions.

Inspired by our results for Pt(1 1 1), we reinvestigated the discrepancy between theoretical calculations and experimental observations of step stiffness anisotropy on Cu(1 0 0). To take into account the effect of adatom relaxations on the computed strengths of right-isosceles trio, we distinguished right-isosceles trios based on their local position. As expected, the right-isosceles trio in the dense interior of (1 × 1) overlayer (E'_d) has a higher energy than the one at the step edge (E_d) due to the suppression of adatom relaxation in the former case. Our results show that a careful consideration of relaxation effects through the introduction of position-dependent right-isosceles trios significantly narrows the discrepancy between theory and experiments. However, the usage of position-dependent lattice-gas interactions is inconsistent with the traditional lattice-gas model. In this particular case, this issue can be reconciled through the introduction of a four-adatom quarto (E_Q) interaction.

The Cu(1 1 0) surface is used as a substrate in the molecular self-assembly of a large number of aromatic compounds. Our first principles calculations of adatom interactions show that strong multi-site interactions are present on this surface. The adatom interactions and diffusion barriers computed from our VASP calculations are in excellent agreement with previous theoretical estimates of these parameters. Unlike Al(1 1 0), attractive cross-channel interactions are present on this surface. The results of our calculations do not preclude the prediction of nanohut formation on this surface. We look forward to experimental growth studies that would validate this prediction. Relaxation effects are prominent for multi-site interactions but are not present in the case of pair interactions. A careful consideration of these effects through the introduction of higher-order multi-site interactions is sufficient to achieve an excellent lattice-gas characterization on this surface. Our results also show that the recently developed connector model is as efficient as the lattice gas model in characterizing adatom interactions on this surface.

Our results presented in Chapter 2 show that multi-site interactions between closely-spaced adatoms are sensitive to adatom relaxations. At the same time, pair interaction strengths remain stable with different relaxation schemes. Since multi-site interactions are more relevant for computing properties related to steps, neglecting relaxation effects in the computations of multi-site interaction strengths could lead to discrepancies between theoretical predictions and experimental observations, as exemplified by the cases of step formation energies on Pt(1 1 1) and step stiffness anisotropy on Cu(1 0 0). One of the ways to handle such relaxation effects is through the introduction of higher-order multi-site interactions. Even this prescription fails in the case of Pt(1 1 1) for reasons mentioned in Chapter 2. Our results emphasize the importance of multi-site interactions and the role of adatom relaxations in lattice-gas modeling of overlayer systems. Right now, only ad hoc approaches are present to handle this problem. We look forward to the development of alternate models that can deal with adatom relaxations efficiently.

The meandering and mounding instabilities on Cu vicinals observed by Ernst and co-workers has eluded theoretical explanation for almost a decade. Further motivation to study this problem comes from the fact that the exact mechanism behind these instabilities could be used for planar nanostructuring surfaces. Kinetic Monte Carlo simulations of A. B-H. Hamouda showed that a small percentage of impurities codeposited with Cu atoms during growth could cause the observed instabilities. To narrow down the impurity atoms responsible for the observed instabilities, we computed the E_{NN} and E_d values for several candidate impurity atoms on Cu(1 0 0). Based on the conditions derived from kinetic Monte Carlo simulations, our VASP calculations indicate Mn, Fe and W as the potential impurity candidates. Further discussions with people involved in the original experiments indicate W as the most probably impurity.

In addition to identifying the impurity atom responsible for the observed instabilities, our calculations also show certain interesting trends in growth morphologies. Based on their E_{NN} and E_d values relative to the values for Cu, the impurities can be classified into four sets. In Chapter 3, we have shown that codeposition of impurities from different sets leads to very different surface morphologies. This shows that the resulting surface morphologies during growth can be manipulated through codeposition of a suitable impurity atom. Snapshots of early stages of growth show that the differences in surface morphologies for the cases of impurities from different sets are already present in the submonolayer growth regime. Our results for Cu can be easily extended to other metallic surfaces. The results of our study presented in Chapter 3 can be used for achieving planar nanostructuring of vicinal surfaces.

The step-step interaction strength ($\tilde{A}$) is an important parameter in modeling vicinal surfaces. Analytical treatment of this problem has been made possible through the mapping of a system of fluctuating steps to fermions on a 1D ring. The resulting generalized Wigner distribution has provided a straightforward method to measure $\tilde{A}$ through experimental measurements of TWDs. However, in addition to the realistic no-crossing condition, the fermion picture imposes a more restrictive non-touching condition. Using the Metropolis Monte Carlo method, we have studied the effects of loosening this non-touching condition on the resulting TWDs. Our results show that the TWDs of touching steps are broader than the TWDs of non-touching steps. At the same time, the generalized Wigner distribution with minor modifications at small ℓ values gives very good fits to the TWDs of touching steps. We have shown that a direct application of the generalized Wigner formalism, neglecting the effects of touching, results in an effective attraction between steps. The strength of this effective attraction can be modeled as a finite-size effect in $\tilde{A}$ measurements. In the light of such results, experiments seeking to extract $\tilde{A}$ of a particular material should check for occurrences of touching during step fluctuations. In addition to that, these experiments should employ several vicinals, at least some of them with large $\langle \ell \rangle$ values. We look forward to experiments that can verify the form of finite-size scaling function.

5.2 Future work

This thesis focusses on modeling of steps on vicinal surfaces using a few key parameters. There are several directions in which the results presented in this work could be extended. Foremost among them is the formulation of a model for characterizing adatom interactions that handles relaxation effects more efficiently than the traditional lattice-gas model. This issue is very important for lattice-gas modeling of steps because of greater relaxations of step edge atoms compared to atoms in the 2D bulk. The biggest challenge in constructing such a model is to accommodate relaxation effects with few parameters (preferably around 10). Both lattice-gas and connector models could handle relaxation effects with a large set of interaction parameters. Hence, any model that seeks to improve on these two models should achieve this with fewer number of interaction parameters.

An equally important direction is the further exploration of the role of codeposited impurities in growth morphologies. Our results for impurities codeposited during growth on Cu vicinals show that even a small concentration of impurities could effect significant changes in the resulting surface morphologies. Hence, impurities could be used to create nanostructures with desired morphological features. Even though our study concerns the role of impurities in the formation of pyramidal structures, there are other nanostructures, such as nanowires and nanorings, that could be fabricated through codeposition of appropriate impurity atom(s). Our results indicate that the resulting surface morphology is determined by the E_{NN} and E_d values of the impurity atom relative to the corresponding values for the substrate. We invite studies that explore this connection between the surface morphology and the relative values of E_{NN} and E_d for the impurity atoms. Also, there are certain common characteristics among the elements of these sets, e.g., all elements of the AgSnZnAl set contain either completely filled or fully empty d-orbitals and all elements in the CoFeMnW set are mid-transition elements. Studying whether other elements with these characteristics fall into the same sets using DFT-based VASP calculations would serve as a straightforward, but nevertheless fruitful, extension of this work. All of these studies should be aimed towards attaining the ability to predict resulting surface morphologies for a particular impurity-substrate system at the given experimental conditions.

The modified generalized Wigner distribution (MGWD) provides a very good description of the TWDs of touching steps. However, no strong theoretical explanation for either the MGWD or the form of finite-size scaling function presented in Chapter 4 exists at present. Our preliminary results for fully kinked (zigzag) steps show that their equilibrium TWDs are very similar to the case of straight steps. However, the Metropolis method does not provide any information regarding the evolution of TWDs toward their equilibrium value for fully kinked steps. For the case of straight steps, the Fokker-Planck formalism has been very useful in understanding the equilibration of TWDs of straight steps. A study based on kinetic Monte Carlo simulations of fluctuations of fully kinked steps would shed light on the applicability of the Fokker-Planck picture for fully kinked steps.

Appendix A

Size-distribution of second-level administrative divisions

The topic of county sizes has been one of long standing interest in the field of social sciences [115, 116]. Even though numerous models have been proposed to describe the size of counties, especially in the United States, none of them could provide a complete description due to the complex nature of the problem [116]. An analytic treatment of this problem is difficult due to the influence of several political, ecological, and geographical factors in the county formation process. Here, we investigate similarities between island nucleation on vicinal surfaces and the formation of second-level administrative divisions (SLAD), such as counties, districts, and arrondissements, in the United States and some European countries. The problem of 2D island growth has been studied extensively; hence such similarities, if present, could lead to a deeper understanding of the process of county formation. We focus on the SLAD due to the following reason: the first level administrative divisions (states) in a country are too few to be described by any continuous distribution and the third level administrative divisions, though numerous, are unsuitable due to the difficulty involved in obtaining the relevant data. In the past, models based on diffusion-limited aggregation and percolation have been used to explain the fractal nature of city morphology [117]. Our work is motivated by the fact that the polygons formed by county boundaries in the size-division model (see Fig. 3.8J in [115]) resemble capture-zones (CZ) in island nucleation. Also, the formation of counties in several states in the United States (especially in the southeast), as nicely visualized in this website [118], look qualitatively similar to the nucleation and growth of islands on vicinal surfaces. Hence, we surmise that the GWD ($P_\varrho(s)$) and the single-parameter Gamma distribution ($\Pi_\alpha(s) = \frac{\alpha^\alpha}{\Gamma(\alpha)} s^{\alpha-1} e^{-\alpha s}$), distributions that are normally used to describe CZ areas, should give a very good description of county-size distribution.

It is very difficult to translate the effects of political, ecological, and geographical factors in the problem of nucleation and growth; accordingly, we neglect them in this study. Our aim is to start out with a simple model of island nucleation that captures the essence of the county formation process. Since the effects of influencing factors are neglected, the simple island nucleation picture can be applied to the county-size distribution only in countries that: (i) have a uniform or near-uniform geographical profile, (ii) have a large geographical area such that the boundary effects are kept to a minimum, and (iii) included the notion of distance from the county center during the formation of counties. There are very few countries that satisfy the first two conditions. Two countries that meet all three conditions are the Thirteen Colonies of the United States of America and France. The Thirteen Colonies later became eighteen states in the present day United States of America but the boundaries of the Thirteen Colonies do not coincide with the present day boundaries of these eighteen states [119]. There are three types of counties in these eighteen states: New England, southern and mixed types [115]. Of these three types, only the southern type counties satisfy the third condition. For people of a county to assemble at the "county court" on a particular day, the county boundaries should not be too far away from the seat of the county [115]. Similarly, the French departments (*Départements* in French) were formed such that one could travel to the chef-lieu from any part of the department within a day on a horse [120]. We focus on arrondissements, the sub-division of departments, which are actually the SLAD in France.

We gathered our data mainly from two sources: (i) the statoids website [121] and (ii) wikipedia [122]. Due to their small size, we omitted all urban counties (e.g. Baltimore city county, Paris and the three surrounding inner ring departments, etc.) from our analysis. Since there are few urban counties, this does not affect our results in any significant manner. Also, we did not consider the arrondissements in the overseas departments of France. Hence, our data corresponds to 692 counties spread across 8 states (Maryland, Virginia, West Virginia, Kentucky, Tennessee, North Carolina, South Carolina, and Georgia) in the US and 314 arrondisements in 90 departments[1] in France. We used both single-parameter Gamma distribution ($\Pi_\alpha(s)$) and the GWD ($P_\varrho(s)$) to fit the size distribution of SLAD. To determine the values of γ and ϱ, we used the non-linear fitting function in MATHEMATICA$^{\circledR}$. All data points were weighed equally in obtaining the fits. The values of γ and ϱ obtained from our fits are listed in Table A.1.

The distributions of SLAD sizes in the Thirteen Colonies (only southern type counties) and France are plotted in Figs. A.1. The quantity s denotes the normalized

---

[1] There are 94 departments in mainland France of which Paris and the three inner ring departments are omitted.

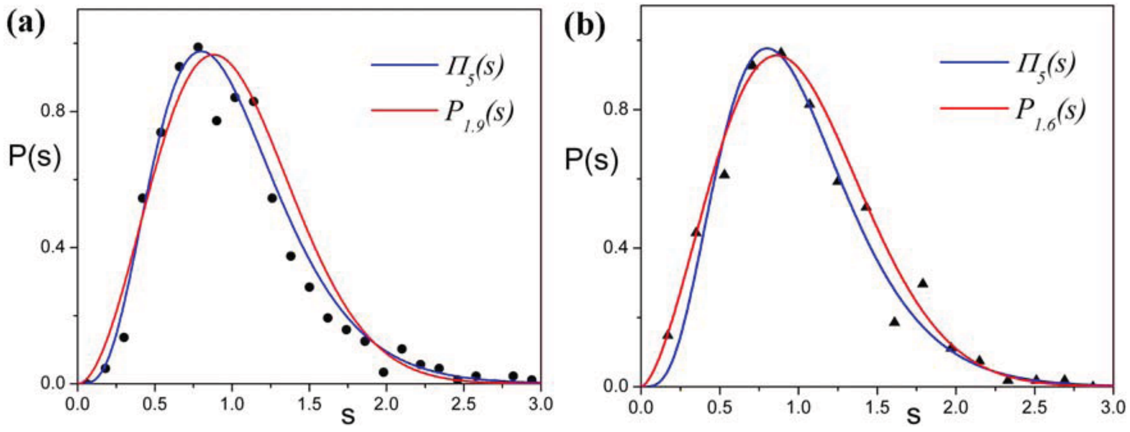

Figure A.1: Size distribution of SLAD in (a) the Thirteen Colonies (circles) and (b) France (triangles). The solid curves correspond to fits with $\Pi_\alpha(s)$ (blue curve) and $P_\varrho(s)$ (red curve). The values of the fit parameters are listed in Table A.1.

surface area, i.e. the ratio of county area to the mean area of all counties. It is clear from Fig. A.1(a) that $\Pi_5(s)$ gives a better fit than $P_{1.9}(s)$ in the case of Thirteen Colonies. In addition to failing to capture the key features of the distribution, the peak of the GWD ($P_{1.9}(s)$) occurs at a s value higher than the corresponding value for the distribution. At the same time, both $\Pi_5(s)$ and $P_{1.6}(s)$ give equally good fits for the size distribution of French arrondissements (cf. Fig. A.1(b)). In our analysis, we find that the size-distribution of SLAD in several countries that do not explicitly satisfy the aforementioned conditions, are also described well by both the Gamma distribution and the GWD. Even though the states Alabama, Louisiana and Florida were not part of the Thirteen Colonies, the formation of counties in these states (see Ref. [118]) resemble island nucleation and growth on vicinal surfaces. The county-size distribution when the counties in these three states are taken together with the counties in the Thirteen Colonies is well described by both the Gamma distribution and the GWD with $\alpha = 3.8$ and $\varrho = 1.3$ respectively. Also, the size-

Table A.1: The fit parameters α and ϱ obtained from our MATHEMATICA$^{®}$ fits to the size-distribution of SLAD in different countries/regions. The symbol 13C denotes regions in the Thirteen Colonies and N.A. denotes cases where we could not find a fit using MATHEMATICA$^{®}$.

Country/Region	α	ϱ
France	N.A.	1.6 ± 0.2
Germany	N.A.	1.4 ± 0.3
Italy	3.3 ± 0.4	1.1 ± 0.3
Mixed type (13C)	3.0 ± 0.2	0.9 ± 0.1
Southern type (13C)	5.0 ± 0.5	1.9 ± 0.3
Southern type + AL, FL and LA (13C)	3.8 ± 0.3	1.3 ± 0.3
Poland	4.9 ± 0.4	1.8 ± 0.3

distribution of counties in New York, New Jersey, Pennsylvania, and Delaware, the mixed type counties, is fit well by $\Pi_3(s)$ and $P_{0.9}(s)$.[2] Similarly, we find that the size-distributions of rural districts in Germany (Landkreise), provinces in Italy and powiaty in Poland are very well described by both distributions. The values of the fit parameters α and ϱ for these cases are listed in Table A.1. In most of the cases, the fit with $\Pi_\alpha(s)$ is slightly better than the fit with $P_\varrho(s)$ mainly due to the peak of $P_\varrho(s)$ occurring at a higher s value compared to the distribution.

Region-specific factors could play an important role in the formation of counties. For instance, the three different types of county formation processes disrupt a generic treatment of county-size distribution in the Thirteen Colonies. The southern and the mixed type counties are fit well by both $\Pi_\alpha(s)$ and $P_\varrho(s)$ but with different values of the fit parameters (see Table A.1); at the same time, both distributions

---

[2] There are only 67 New England type counties. Both $\Pi_\alpha(s)$ and $P_\varrho(s)$ do not give a very good fit to the size distribution of these counties.

fail to give a good description of the size distribution of New England type counties. Since the county formation process varies across states, an effective way to incorporate its effects in our analysis is to consider the distribution of county sizes normalized by the respective statewise averages. When the county areas are normalized by statewise averages, our results show that the county-size distribution in the Thirteen Colonies (eighteen states in the present day United States of America) and the Thirteen Colonies with Alabama, Florida and Louisiana are fit very well by both $\Pi_\alpha(s)$ and $P_\varrho(s)$. The values of α and ϱ for these two cases are listed in Table A.2.

The statewise normalization of SLAD areas only serves to increase the number of data points and is not inconsistent with the rest of our analysis. As mentioned earlier, one of the main reasons behind focusing on SLAD than on first level administrative divisions is that the SLADs in many countries are sufficiently numerous to be fit by a continuous distribution. Hence, there is no compelling reason to focus on the county-size distribution across a country. In fact, the distributions of county

Table A.2: The fit parameters α and ϱ for the size-distribution of SLAD after statewise normalization in different countries/regions.

Country/Region	α	ϱ
Thirteen Colonies	5.7 ± 0.2	2.3 ± 0.3
Thirteen Colonies + AL, FL and LA	6.0 ± 0.3	2.4 ± 0.3
Georgia	5.4 ± 0.3	2.1 ± 0.3
Kentucky	5.4 ± 0.4	2.4 ± 0.3
Virginia	5.7 ± 0.9	2.3 ± 0.7
India	4.0 ± 0.1	1.4 ± 0.2

sizes in Georgia, Kentucky, and Virginia, the three states with the maximum number of counties in the Thirteen Colonies, considered separately, are again described very well by the Gamma distribution and the GWD. The values of the fit parameters (cf. Table A.2) for all three states are very close. In addition to that, the statewise normalization of SLAD areas increases the range of applicability of our model. In India, where the division of states is along linguistic lines [122], there is a vast difference in the state areas (the ratio of the areas of the largest to the smallest state is 92.4), which results in a wide variation in the average district (SLAD in India) size between states. Hence, the size distribution of districts (SLAD in India) is not fit well by either $\Pi_\alpha(s)$ or $P_\varrho(s)$. However, when the district areas are normalized by the average district size in the respective state, we find that the distribution is fit very well by both $\Pi_4(s)$ and $P_{1.4}(s)$.

Our results show that similar to the nucleation and growth of islands on vicinal surfaces, both the Gamma distribution ($\Pi_\alpha(s)$) and the GWD ($P_\varrho(s)$) give very good fits for the size distribution of SLAD in several countries. It is noteworthy that $\Pi_\alpha(s)$ has been proposed to describe the size distribution of Poisson Voronoi cells[3] in 1, 2, and 3 spatial dimensions [123], where the fit parameter (α) is related to the spatial dimension (d) through

$$\alpha = \left(\frac{3d+1}{2}\right). \tag{A.1}$$

The fact that the α values from our fits are not equal to 3.5, the value for Poisson Voronoi cells in 2D, indicates that SLAD are not random tesselations of 2D space

---

[3] Voronoi polygons constructed using a set of points that are randomly distributed in space.

but possess certain correlations like CZ in island nucleation. It would be interesting to investigate the connection between the fit parameters α and ϱ and various factors that influence the SLAD formation process. Including the effects of such influencing factors would widen the range of applicability of this model.

Appendix B

Appendix B

B.1 Nearest-neighbor excluding steps

As mentioned in Chapter 2, in addition to the long-range inverse-square repulsion, higher-order repulsive interactions ($\mathcal{O}(\ell^{-3})$, $\mathcal{O}(\ell^{-4})$) could play a role at small step separations [106]. The presence of such repulsive interactions would preclude neighboring steps from being closer than a few lattice spacings. In the simplest case, steps cannot get closer than nearest-neighbors ($2a$, where a is the lattice constant)[1], the so-called nearest-neighbor excluding (NNE) steps. Since our Monte Carlo simulations showed that step touching leads to an effective attraction, we anticipated nearest-neighbor exclusion to result in an effective repulsion between steps. To check if nearest-neighbor exclusion affects $\tilde{A}$ measurements, we simulated the TWDs of straight NNE steps using the Metropolis method in Monte Carlo simulations. We used the same simulation parameters (N, L_y, and $\beta\epsilon_k$) mentioned in Chapter 4. We considered only the case of free-fermions. However, unlike touching steps, introduction of energetic interactions between NNE steps does not lead to divergence in the repulsion term.

Our results show that the GWD gives an excellent fit to the TWDs of NNE steps (see Fig. B.1). Since $P(0) = 0$, no corrections to the GWD are needed to

---

[1] Even though the nearest-neighbor distance on a simple cubic lattice is $\sqrt{2}a$, the nearest-neighbor distance in the direction perpendicular to the step edge ($\hat{x}$) is $2a$.

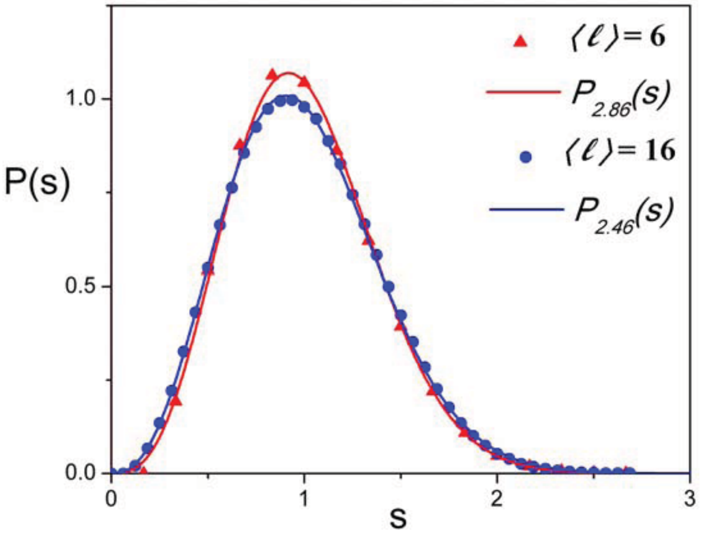

Figure B.1: TWDs of NNE steps from our simulations (symbols) and respective GWD fits (solid curves). The values of the fit parameter (ϱ) are listed in Table B.1.

obtain fits to TWDs of NNE steps. To obtain the values of ϱ, we used the non-linear fitting function with equal weight assigned to all data points. The ϱ values obtained from MATHEMATICA® are listed in Table B.1. As expected, the ϱ values are higher than 2, indicating an effective repulsion between steps. Similar to touching steps, the strength of this effective repulsion decreases with $\langle \ell \rangle$.

Using the mapping scheme mentioned in Section 4.5, a surface of NNE steps can be mapped to a surface with non-touching steps by deleting a row of atoms

Table B.1: Values of ϱ obtained from fits to our simulations of TWDs of NNE steps for different $\langle \ell \rangle$ values.

$\langle \ell \rangle$	ϱ
6	2.86 ± 0.01
8	2.610 ± 0.008
10	2.511 ± 0.004
12	2.470 ± 0.002
16	2.455 ± 0.005

along the step-edge direction [103, 107]. However, unlike the case of touching steps, where this mapping provided a way to compute $P(0)$ values for the $\beta\epsilon_t = 0$ case, it does not provide any physically relevant information for NNE steps.

B.2 Finite-size scaling

Similar to the case of touching steps, we model the strength of this effective repulsion as a finite-size effect. Once again, we write

$$\varrho = \varrho_\infty + g(\langle \ell \rangle), \quad g(\langle \ell \rangle) \overset{\langle \ell \rangle \to \infty}{\longrightarrow} 0^+ \tag{B.1}$$

and the following power-law decay with $\langle \ell \rangle$ gives the best fit to our data (cf. Fig. B.2)

$$g(\langle \ell \rangle) = \frac{E}{\langle \ell \rangle^r} \quad \text{with} \quad E = 3 \pm 1, r = 0.8 \pm 0.1. \tag{B.2}$$

As can be seen from Fig. B.2, the finite-size scaling function, $g(\langle \ell \rangle)$, also gives a very good fit to the scaling of the effective attraction with $\langle \ell \rangle$ in the case of touching steps. At the same time, the finite-size scaling function derived for touching steps, $f(\langle \ell \rangle, \beta\epsilon_t = 0)$, gives only a moderate fit for the scaling of both NNE and touching steps.

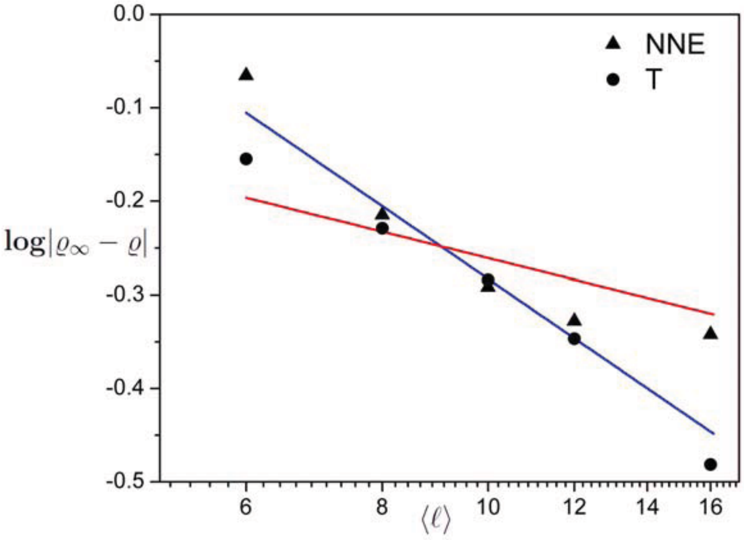

Figure B.2: Finite-size scaling of effective interaction strengths in the cases of NNE (triangles) and touching (discs) steps. The solid blue curve is the plot of Eq. (B.2) and the solid red curve is plot of finite-size scaling function derived for touching steps Eq. (4.14).

Bibliography

[1] J. V. Barth, G. Constantini, K. Kern, Nature **437**, 671 (2005).

[2] H.-C. Jeong, E.D. Williams, Surf. Sci. Rep. **34**, 171 (1999).

[3] M. Giesen, Prog. Surf. Sci. **68**, 1 (2001).

[4] T. J. Stasevich, H. Gebremariam, T. L. Einstein, M. Giesen, C. Steimer, H. Ibach, Phys. Rev. B **71**, 245414 (2005).

[5] T. J. Stasevich, T. L. Einstein, Phys. Rev. B **73**, 115426 (2006).

[6] T. Michely, G. Comsa, Surf. Sci. **256**, 217 (1991).

[7] N. Néel, T. Maroutian, L. Douillard, H.-J. Ernst, J. Phys.: Cond. Matt. **15**, S3227 (2003) and references therein.

[8] R. Sathiyanarayanan, A. BH. Hamouda, T. L. Einstein, Phys. Rev. B **80**, 153415 (2009).

[9] T. L. Einstein, Appl. Phys. A **87**, 375 (2007) and references therein.

[10] C. Schwennicke, X.-S. Wang, T. L. Einstein, E. D. Williams, Surf. Sci. **418**, 22 (1998).

[11] J.C. Slater, G.F. Koster, Phys. Rev. **94**, 1498 (1954).

[12] C.M. Goringe, D.R. Bowler, E. Hernández, Rep. Prog. Phys. **60**, 1447 (1997).

[13] M. S. Daw, M. I. Baskes, Phys. Rev. B **29**, 6443 (1984).

[14] S. M. Foiles, M. I. Baskes, M. S. Daw, Phys. Rev. B **33**, 7983 (1986).

[15] P. Hohenberg, W. Kohn, Phys. Rev. **136**, 11169 (1964) .

[16] W. Kohn, L. J. Sham, Phys. Rev. **140**, A1133 (1965).

[17] G. Kresse, J. Hafner, Phys. Rev. B **47**, R558 (1993).

[18] G. Kresse, J. Hafner, Phys. Rev. B **49**, 14251 (1994).

[19] G. Kresse, J. Furthmüller, Comp. Mater. Sci. **6**, 15 (1996).

[20] G. Kresse, J. Furthmüller, Phys. Rev. B **54**, 11169 (1996).

[21] F. Calogero, J. Math. Phys. (N.Y.) **10**, 2191 (1969); **10**, 2197 (1969); B. Sutherland, J. Math. Phys. (N.Y.) **12**, 246 (1971); Phys. Rev. A **4**, 2019 (1971).

[22] R. Sathiyanarayanan, T. J. Stasevich, T. L. Einstein, Surf. Sci. **602**, 1243 (2008).

[23] R. Sathiyanarayanan, T. L. Einstein, Surf. Sci. **603**, 2387 (2009).

[24] L. D.Roelofs, in: R. Vanselow, R. F. Howe (Editors), Chemistry and Physics of Solid Surfaces IV, Springer, Berlin, 1982 (Chapter 10).

[25] B. N. J. Persson, Surf. Sci. Rep. **15**, 1 (1992).

[26] T. L. Einstein, in: W. N. Unertl (Editor), Physical Structure of Solid Surfaces, Handbook of Surface Science, Vol. 1, Elsevier, Amsterdam, 1996, p.577.

[27] A. Patrykiejew, S. Sokolowski, K. Binder, Surf. Sci. Rep. **37**, 207 (2000).

[28] A. Groß, *Theoretical Suface Science: A Microscopic Perspective*, 1st ed., (Springer, Berlin 2002).

[29] D. S. Sholl, J. A. Steckel, *Density Functional Theory: A Practical Introduction*, 1st ed., (Wiley, New Jersey 2009).

[30] S. -J. Koh, G. Ehrlich, Phys. Rev. B **60**, 5981 (1999).

[31] C. Stampfl, H. J. Kreuzer, S. H. Payne, H. Pfnr, M. Scheffler, Phys. Rev. Lett. **83**, 2993 (1999).

[32] L. Österlund, M. Ø. Pederson, I. Stensgaard, E. Lægsgaard, F. Besenbacher, Phys. Rev. Lett. **83**, 4812 (1999).

[33] C. Stampfl, Catalysis Today **105** (2005) 17; M. Borg et al., Chem. Phys. Chem. **6**, 1923 (2005).

[34] Y. Zhang, V. Blum, K. Reuter, Phys. Rev. B **75**, 235406 (2007).

[35] Y. Tiwary, K. A. Fichthorn, Phys. Rev. B **75**, 235451 (2007).

[36] Y. Tiwary, K. A. Fichthorn, Phys. Rev. B. **78**, 205418 (2008).

[37] P. J. Feibelman, Surf. Sci. **463**, L661 (2000).

[38] P. J. Feibelman, Phys. Rev. B **60**, 11118 (1999).

[39] M. -C. Marinicia, C. Barreteau, M. -C. Desjonquères, D. Spanjaard, Phys. Rev. B **70**, 075415 (2004).

[40] J. P. Perdew in P. Ziesche, H. Eschrig (Eds.), Electronic Structure Theory of Solids, Akademie Verlag, Berlin, 1991; J. P. Perdew , J. A. Chevary, S. H. Vosko, K. A. Jackson, M. R. Pederson, D. J. Singh, C. Fiolhais, Phys. Rev. B **46**, 6671 (1992).

[41] G. Boisvert, L. J. Lewis, M. Scheffler, Phys. Rev. B **57**, 1881 (1998).

[42] M. Methfessel, A. T. Paxton, Phys. Rev. B **40**, 3616 (1989).

[43] http://cms.mpi.univie.ac.at/vasp/guide/node124.html

[44] K. A. Fichthorn, M. Scheffler, Phys. Rev. Lett. **84**, 5371 (2000); K. A. Fichthorn, M. L. Merrick, M. Scheffler, Phys. Rev. B **68**, 041404(R) (2003).

[45] R.C. Nelson, T.L. Einstein, S.V. Khare, P.J. Rous, Surf. Sci. **295**, 462 (1993).

[46] H. S. Johnston, C. Parr, J. Am. Chem. Soc. **85**, 2544 (1963).

[47] S. Dieluweit, H. Ibach, M. Giesen, T. L. Einstein, Phys. Rev. B **67**, 121410(R) (2003).

[48] T. J. Stasevich, T. L. Einstein, R. K. P. Zia, M. Giesen, H. Ibach, F. Szalma, Phys. Rev. B **70**, 245404 (2004).

[49] R. Van Moere, H. J. W. Zandvliet, B. Poelsema, Phys. Rev. B **67**, 193407 (2003).

[50] H. J. W. Zandvliet, R. Van Moere, B. Poelsema, Phys. Rev. B **68**, 073404 (2003).

[51] W. A. Harrison, Phys. Rev. B **7**, 2408 (1973).

[52] L. D. Roelofs, S. M. Foiles, M. S. Daw, M. I. Baskes, Surf. Sci. **234**, 63 (1990).

[53] F. B. de Mongeot, W. Zhu, A. Molle, R. Buzio, C. Boragno, U. Valbusa, E. G. Wang, Z. Y. Zhang, Phys. Rev. Lett. **91**, 016102 (2003).

[54] W. Zhu, F. B. de Mongeot, U. Valbusa, E. G. Wang, Z. Y. Zhang, Phys. Rev. Lett. **92**, 106102 (2004).

[55] H. Yang, Q. Sun, Z. Zhang, Y. Jia, Phys. Rev. B **76**, 115417 (2007).

[56] C. C. Perry, S. Haq, B. G. Frederick, N. V. Richardson, Surf. Sci. **409**, 512 (1998).

[57] S. S. P. Parkin, Z. G. Li, D. J. Smith, Appl. Phys. Lett. **58**, 2710 (1991).

[58] Y. Shu, J.-M. Zhang, K.-W. Xu, V. Ji, Solid State Communications **141**, 384 (2007) and references therein.

[59] J. Shao, J. Am. Stat. Assoc. **88** (422), 486 (1993).

[60] C. Mottet, R. Ferrando, F. Hontinfinde, A. C. Levi, Surf. Sci. **417**, 220 (1998) and references therein.

[61] T.L. Einstein, Langmuir **7**, 2520 (1991).

[62] U.T. Ndongmouo, F. Hontinfinde, Surf. Sci. **571**, 89 (2004) and references therein, especially for EAM calculations.

[63] O. Stepanyuk, N. N. Negulyaev, A. M. Saletsky, W. Hergert, Phys. Rev. B **78**, 113406 (2008).

[64] G. Mills, H. Jónsson, G. K. Schenter, Surf. Science **324**, 305 (1995).

[65] H. Jónsson, G. Mills, K. W. Jacobsen, in: B. J. Berne, G. Ciccotti, D. F. Coker (Editors), Classical and Quantum Dynamics in Condensed Phase Simulations, World Scientific, 1998.

[66] F. Montalenti, R. Ferrando, Phys. Rev. B **59**, 5881 (1999).

[67] V. Rosato, M. Guillopé, B. Legrand, Philos. Mag. A **59**, 321 (1989).

[68] F. Montalenti, R. Ferrando, Phys. Rev. B **58**, 3617 (1998).

[69] T. R. Linderoth, S. Horch, L. Petersen, S. Helveg, E. Lægsgaard, I. Stensgaard, F. Besenbacher, Phys. Rev. Lett. **82**, 1494 (1999).

[70] F. Montalenti, R. Ferrando, Phys. Rev. Lett. **82**, 1498 (1999).

[71] G. S. Bales, A. Zangwill, Phys. Rev. B **41**, 5500 (1990).

[72] R. L. Schwoebel, E. J. Shipley, J. Appl. Phys. **37**, 3682 (1966).

[73] G. Ehrlich, F. G. Hudda, J. Chem. Phys. **44**, 1039 (1966).

[74] O. Pierre-Louis, M. R. D'Orsogna, T. L. Einstein, Phys. Rev. Lett. **82**, 3661 (1999) 3661.

[75] M. V. Ramana Murty, B. H. Cooper, Phys. Rev. Lett. **83**, 352 (1999).

[76] P. Politi, J. Krug, Surf. Sci. **446**, 89 (2000).

[77] F. Nita, A. Pimpinelli, Phys. Rev. Lett. **95**, 106104 (2005).

[78] J. Kallunki, J. Krug, M. Kotrla, Phys. Rev. B **65**, 205411 (2002).

[79] R. Gerlach, T. Maroutian, L. Douillard, D. Martinotti, H.-J. Ernst, Surf. Sci. **480**, 97 (2001).

[80] H. Yildirim, A. Kara, S. Durukanoğlu, T. S. Rahman, Surf. Sci. **600**, 484 (2006).

[81] A. B-H. Hamouda, N. Absi, P. E. Hoggan, A. Pimpinelli, Phys. Rev. B **77**, 245430 (2008).

[82] P.E. Blöchl, Phys. Rev. B **50**, 17953 (1994).

[83] J.P. Perdew, K. Burke, M. Ernzerhof, Phys. Rev. Lett. **77**, 3865 (1996).

[84] G. Kresse, D. Joubert, Phys. Rev. B **59**, 1758 (1999).

[85] http://cms.mpi.univie.ac.at/vasp/vasp/

[86] W. F. Egelhoff, I. Jacob, Phys. Rev. Lett. **62**, 921 (1989).

[87] J. W. Evans, P. A. Thiel, M. C. Bartelt, Surf. Sci. Rep. **61**, 1 (2006).

[88] M. Kotrla, J. Krug, P. Šmilauer, Phys. Rev. B **62**, 2889 (2000).

[89] J. G. Amar, F. Family, Phys. Rev. Lett. **74**, 2066 (1995).

[90] P. A. Mulheran, J. A. Blackman, Philos. Mag. Lett. **72**, 55 (1995); P. A. Mulheran, J. A. Blackman, Phys. Rev. B **53**, 10261 (1995).

[91] M.L. Mehta, *Random Matrices*, 2nd ed. (Academic, New York, 1991).

[92] F. Haake, *Quantum Signatures of Chaos* (Springer, Berlin, 1991).

[93] A. Pimpinelli, T. L. Einstein, Phys. Rev. Lett. **99**, 226102 (2007) and references therein.

[94] T. L. Einstein, P31.00009 March Meeting of the American Physical Society (2008).

[95] F. Shi, Y. Shim, J. G. Amar, Phys. Rev. E **79**, 011602 (2009).

[96] B. R. Conrad, E. Gomar-Nadal, W. G. Cullen, A. Pimpinelli, T. L. Einstein, E. D. Williams, Phys. Rev. B **77**, 205328 (2007).

[97] A. Pimpinelli, unpublished.

[98] T. S. Rahman, H. Yildirim, Q12.00007 March Meeting of the American Physical Society (2009) and preprint.

[99] Y. Mo, W. Zhu, E. Kaxiras, Z. Zhang, Phys. Rev. Lett. **101**, 216101 (2008).

[100] H. Gebremariam, S.D. Cohen, H.L. Richards, T.L. Einstein, Phys. Rev. B **69**, 125404 (2004) and references therein.

[101] A. Pimpinelli, Hailu Gebremariam, T.L. Einstein, Phys. Rev. Lett. **95**, 246101 (2005).

[102] A.BH. Hamouda, A. Pimpinelli, T.L. Einstein, Surf. Sci. **602**, 3569 (2008).

[103] K. Kim, T. L. Einstein, preprint.

[104] D. B. Abraham, F. H. L. Essler, and F. T. Latrémolière, Nucl. Phys. B **556**, 411 (1999).

[105] H.L. Richards, S.D. Cohen, T.L. Einstein, and M. Giesen, Surf. Sci. **453**, 59 (2000).

[106] R. Najafabadi, D. J. Srolovitz, Surf. Sci. **317**, 221 (1994).

[107] S.-A. Cheong, C. L. Henley, arXiv:0907.4228v1.

[108] T.W. Burkhardt, P. Schlottmann, J. Phys. A **26**, L501 (1993).

[109] V.B. Shenoy, S. Zhang, W.F. Saam, Surf. Sci. **467**, 58 (2000).

[110] M. E. Fisher, J. Stat. Phys. **34**, 667 (1984).

[111] C. Jayaprakash, C. Rottman, W.F. Saam, Phys. Rev. B **30**, 6549 (1984).

[112] S. T. Chui, J. D. Weeks, Phys. Rev. B **23**, 2438 (1981).

[113] T.W. Burkhardt, P. Schlottmann, Z. Phys. B **54**, 151 (1984).

[114] T. L. Einstein, T. M. Jung, N. C. Bartelt, E. D. Williams, C. Rottman, J. Vac. Sci. Technol. A **10**, 2600 (1992).

[115] `http://www.edstephan.org/Book/contents.html`

[116] K. Rancie, S. M. Otterstrom, J. M. Sanderso, F. J. Donaldson, in: J. D. Gatrell, R. R. Jensons (Editors) Geotechnologies and the Environment, Planning and Socioeconomic Applications, Vol. 1, Springer, Netherlands, 2009, p.183 and references therein.

[117] H. A. Makse, S. Havlin, H. E. Stanley, Nature **377**, 608 (1995).

[118] `http://www.familyhistory101.com/map_county.html`

[119] `http://en.wikipedia.org/wiki/13_colonies`

[120] Frédéric Giraut, Proceedings of the French-South African meeting on territorial innovation Proceedings of the French-South African meeting on territorial innovation (2003).

[121] `http://www.statoids.com`.

[122] `http://en.wikipedia.org/wiki`.

[123] J.-S. Ferenc, Z. Néda, Physica A **385**, 518 (2007).